Quantum Interference Control (QuIC) of Currents in Semiconductors

by

Yiming Gong

A dissertation submitted in partial fulfillment
of the requirements for the degree of
Doctor of Philosophy
(Physics)
in the University of Michigan
2024

Doctoral Committee:

Professor Steven T. Cundiff, Chair
Professor Theodore B. Norris
Professor Jennifer P. Ogilvie
Professor John. E. Sipe
Professor Liuyan Zhao

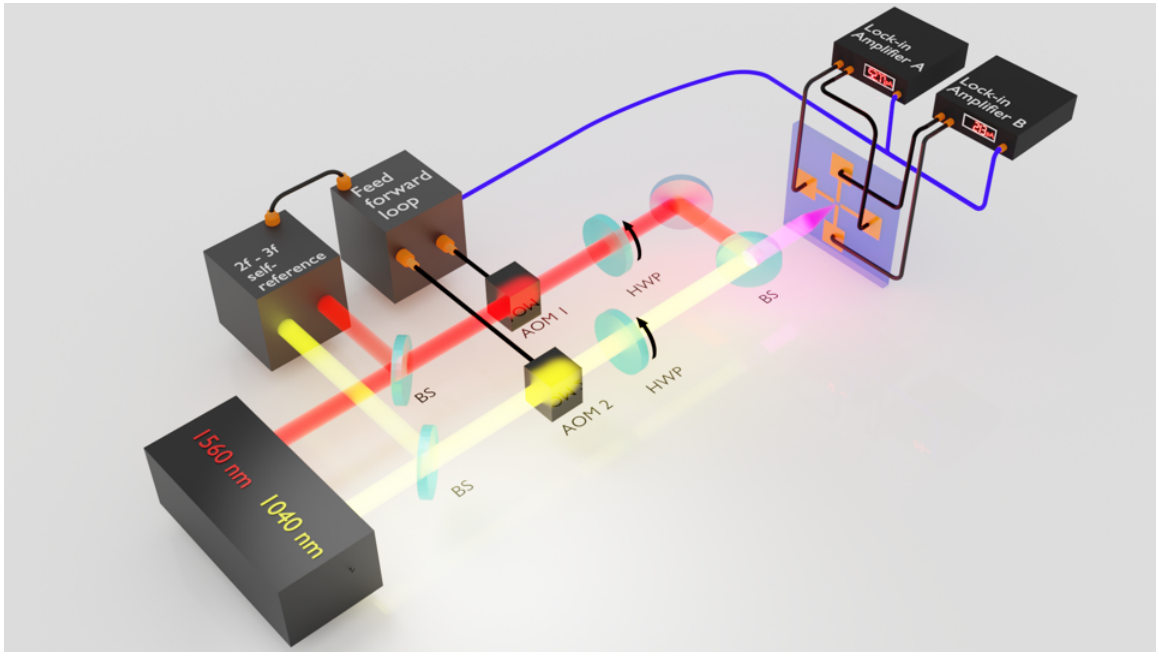
Lock-in Amplifier A
Lock-in Amplifier B
Feed forward loop
2f - 3f self-reference
AOM 1
AOM 2
HWP
HWP
BS
BS
BS
1560 nm
1040 nm

Yiming Gong

ymgong@umich.edu

ORCID iD: 0009-0005-7493-9680

ACKNOWLEDGEMENTS

The journey of a Ph.D. takes persistence, courage, and self-reflection. Over the years, I was fortunate enough to encounter many great souls who have helped me better understand science, life, and myself.

I am grateful for the series of research experiences from undergrad that led me to pursue a Ph.D. in the Cundiff group. I thank Professor Hebin Li, Xiaojun Liu, and Yuanbo Zhang for opening my eyes to the world of research in physics. I am also thankful for the enormous amount of support from members of the Cundiff group. I would like to thank Xiaoyan Ding, with whom I spent countless hours discussing experiments. I greatly benefited from her knowledge of optics and her way of approaching problems. In the second year of my Ph.D., I worked with Ruixue Zhang and Professor Dong Sun on experiments, from which I gained so much knowledge of frequency combs and spectroscopy, which laid the foundation for my Ph.D. project. I would like to thank Professor Kai Wang, without whom I would have never succeeded in my QuIC experiments. Kai has always been very helpful and patient to me despite the 12-hour time difference and the fact that we have never met each other in person. He was always there to steer me away from rabbit holes and dead ends with his previous experience in QuIC experiments. I would like to extend my gratitude to Professor Steven Cundiff, my graduate research advisor, for patiently guiding me with his knowledge and insights over the years. I gained inspiration from the research ideas of Steve every time I felt stuck on a problem. Besides the tremendous amount of academic support, Steve has also been very caring and understanding to me, which I will be forever grateful for.

Lastly, I would like to thank my family for raising and supporting me. I would never be who I am without them. My love for Mom has been and will always be my motivation to live a meaningful life in this world.

PREFACE

My PhD work mainly involves building two experimental setups, one for 1+2 QuIC and the other for 2+3 QuIC, entirely from scratch, developing a more robust detection of 2+3 QuIC, and exploring semiconductor device fabrication in the clean room. I worked independently on these two experiments throughout the time span of my project. Although a previous group member has worked on the 2+3 QuIC experiment before, I've never overlapped with him in the lab. The previous experimental setup was completely taken apart by the time I started my project. Toward the end of my project, I successfully obtained results from both the 1+2 QuIC experiment (Y. Gong, S. T. Cundiff, in preparation) and the 2+3 QuIC experiment(Y. Gong, K. Wang, S. T. Cundiff, in preparation).

TABLE OF CONTENTS

ACKNOWLEDGEMENTS ii

PREFACE iv

LIST OF FIGURES vii

LIST OF APPENDICES xiii

ABSTRACT xiv

CHAPTER

1 Introduction **1**

2 Photocurrent Generation with Quantum Interference Control (QuIC) **5**

2.1 Introduction to Photocurrent 5
2.2 Introduction to Energy Band Structure 7
2.2.1 The band structure of GaAs 9
2.3 How do the electrons and holes move inside crystals? 14
2.4 Oblique Incidence of Light in Photocurrent Injection 17
2.5 1+2 QuIC Theory 19
2.5.1 Carrier Population Control 25
2.5.2 Injection Current Control 26
2.5.3 Swarm Velocity 28
2.6 Carrier Scattering Mechanism 29
2.6.1 Hot Carrier Generation in the QuIC Process 29
2.6.2 Hot Carrier Relaxation 30
2.6.3 Phonon Scattering 32
2.6.4 Energy-momentum Conservation in Phonon Scattering 33

3 1+2 Quantum Interference Control (QuIC) in AlGaAs **35**

3.1 Metal-semiconductor Contact 35
3.2 1+2 QuIC setup 37
3.3 1+2 QuIC 41

3.3.1 Relative-phase Dependence . . . 41
3.3.2 External-resistance Dependence . . . 42

4 2+3 QuIC . . . 48

4.1 Introduction to Frequency Comb . . . 48
4.2 Laser System . . . 52
4.3 2+3 QuIC Theory . . . 55
4.3.1 Carrier Injection in 2+3 QuIC . . . 55
4.3.2 Current Injection in 2+3 QuIC . . . 56
4.3.3 The Localization of Carrier Distribution . . . 58
4.3.4 2+3 QuIC Current Generated with Frequency Combs . . . 59
4.4 Offset Frequency . . . 62
4.4.1 2f-3f Self-referencing Technique . . . 62
4.4.2 Harmonic Generation . . . 66
4.4.3 Feed-forward Loop . . . 69
4.4.4 Feedback Loop . . . 73
4.4.5 Two-Color Temporal Overlap . . . 78
4.5 Experimental Results . . . 79
4.5.1 Detection-frequency Dependence of 2+3 QuIC . . . 79
4.5.2 Relative-phase Dependence of 2+3 QuIC . . . 80
4.5.3 Polarization Dependence of 1+2 QuIC and 2+3 QuIC (dual-polarization rotation) . . . 81
4.5.4 Current Injection Model . . . 83
4.5.5 Polarization Dependence of 1+2 QuIC and 2+3 QuIC (single-polarization rotation) . . . 90
4.5.6 Discussion . . . 94
4.5.7 Summary . . . 95

5 Outlook . . . 96

APPENDICES . . . 98

BIBLIOGRAPHY . . . 102

LIST OF FIGURES

FIGURE

1.1 (A) $E(k_{||})$ 2PPE spectrum of the n = 1 image-potential state on the Cu(100) surface. Energies are referred to as the vacuum level E_{vac}. The color scale indicates the photoemission intensity. (B) Energy diagram of the corresponding excitation and photoemission scheme together with the surface-projected bulk band structure of Cu(100), where $E_{vac}-E_F = 4.64$ eV. Filled and empty projected bulk bands are marked by dark and light shades. The solid curve depicts the n = 1 image-potential band. (C) $E(k_{||})$ spectrum of the n = 1 state for excitation with two phase-locked laser pulses at frequencies ω_a and $\omega_a/2$ as depicted in (D). The 2PPE spectra in (A) and (C) have been recorded with zero time delay of the photoemission pulse ω_b. adapted from Ref. [1] 2

2.1 The lattice structure of GaAs bulk crystal[2]. 9
2.2 The band structure of GaAs[3]. 10
2.3 The carrier distributions in the $\boldsymbol{k}$-space when (a) $E^{\omega} = 0, E^{\omega} \neq 0$ (b) $E^{DC} = 0$ (c) $E^{\omega} = 0, E^{\omega} \neq 0$ (d) $E^{DC} \neq 0$. Reproduced from Ref. [4] . . . 11
2.4 The upper part of the figure is a schematic illustration of the distribution of excited carriers in optical absorption in $k_x - k_z$ plane. The lower part of the figure is a simplified sketch of the band structure of GaAs. The light is linearly polarized along $\langle 010 \rangle$ crystal axis. The photon energy is large enough to reach the three valence bands. adapted from Ref. [5] 12
2.5 The generation of an electron-hole pair in optical absorption. The velocities of the electron and hole are indicated by the blue and green arrows, respectively. 15
2.6 The carriers injected by the QuIC process on the band structure. The interference of the two pathways is constructive at $\boldsymbol{k}$ and destructive at $\boldsymbol{k}'$. The crystal is GaAs (E_g=1.43 eV). The total photon energy is 2.31 eV. The red and black arrows correspond to the optical transitions when the incidence of light is oblique and normal, respectively. The green arrow denotes the $\boldsymbol{k}$ vector of injected carriers. 18
2.7 The calculated imaginary parts of injection coefficient tensor elements as functions of fundamental photon energy for intrinsic GaAs at room temperature. adapted from Ref. [6] 27

2.8 The scattering rates of different kinds of carriers as functions of total photon energy for intrinsic GaAs at room temperature. Electrons injected from the light-hole valence band, electrons injected from the heavy-hole valence band, light-holes, and heavy-holes are denoted by e_{lh}, e_{hh}, lh, and hh, respectively. [7] 29
2.9 A schematic illustration of the scattering processes involved in the carrier relaxation. adapted from Ref. [5] 31
2.10 A sketch of the current injected by the QuIC process as a function of time. 32
2.11 The band structure of phonons in GaAs [5] 33

3.1 A picture of the Ohmic-contact electrodes on the AlGaAs wafer. The four tips are connected to 4 larger metal pads ($1\ mm \times 1\ mm$). The spacing between opposing electrode pairs is 7 μm. The width of each tip is 3 μm. 37
3.2 Left: the I-V curve of the Ohmic horizontal electrode pair. Right: is the I-V curve of the Ohmic vertical electrode pair. The range of applied voltage is from -100 mV to 100 mV. The resistances of these two pairs are fitted by the linear equations, denoted by the orange lines. 38
3.3 The I-V curve of a Schottky electrode pair on AlGaAs from $V_{bias} = -15\,V$ to $V_{bias} = 15\,V$. 38
3.4 A schematic diagram of the 1+2 QuIC setup 38
3.5 The power of the green light after the second BBO crystal is plotted as a function of time, shown as the black curve. The times when the piezo starts to move in the other direction are denoted by the red arrows. The frequency of the slow ramp is 0.5 Hz. 40
3.6 The QuIC signal from the Ohmic-contact sample detected at 2 KHz as a function of the relative time delay. 42
3.7 The X channel of the Lock-in Amplifier measured the relative-phase dependence of the 1+2 QuIC. The horizontal electrode pair of the Ohmic-contact sample was used. The lock-in amplifier was in voltage mode. 43
3.8 The X channel of the Lock-in Amplifier measured the relative-phase dependence of the 1+2 QuIC. The horizontal electrode pair of the Schottky-contact sample was used. The lock-in amplifier was in voltage mode. . . . 43
3.9 The amplitude of 1+2 QuIC from the Schottky-contact sample and Ohmic-contact sample are plotted as functions of the external resistance. 44
3.10 (a) A circuit diagram as a model of the Schottky-contact 1+2 QuIC detection. (b) A circuit diagram as a model of the Ohmic-contact 1+2 QuIC detection. 45
3.11 Left: the amplitude of the 1+2 QuIC from Schottky contact as a function of the external resistance (pink squares). Right: the amplitude of the 1+2 QuIC from Ohmic contact as a function of the external resistance (green squares). The fit curves are calculated based on the circuit models (black triangles). 47

4.1 (a) In the time domain, a frequency comb is defined by an infinitely long train of identical but arbitrarily-shaped envelopes with period $T = 1/f_{rep}$. Each successive carrier wave slips by a phase of $\phi_{off} = 2f_{off}/f_{rep}$ with respect to its envelope. (b) The Fourier transform of (a) reveals comb structure with an FSR of f_{rep} offset from the origin by frequency f_{off}. The optical frequency of each comb tooth is given by $_n = nf_{rep} + f_{off}$ where n is an integer. 51
4.2 (a) The energy diagram of Erbium. adapted from Ref. [8] (b) The absorption and emission spectra of Yb. adapted from Ref. [9] 53
4.3 (a) the spectrum of the optical frequency comb center at 1040 nm. (b) the spectrum of the optical frequency comb center at 1560 nm. 54
4.4 Left: the calculated injection rate of 1+2 QuIC carriers in the $\boldsymbol{k}$-space when the relative phase of two frequencies is $\frac{\pi}{2}$. The fields of frequency ω and 2ω are polarized along $\boldsymbol{k}_x$. Right:the calculated injection rate of 2+3 QuIC carriers in the $\boldsymbol{k}$-space when the relative phase of two frequencies is $\frac{\pi}{2}$. The fields of frequency ω and $\frac{3\omega}{2}$ are polarized along $\boldsymbol{k}_x$. adapted from Ref. [10] 59
4.5 A schematic illustration of the comb teeth of fundamental beam and second harmonic on the frequency domain. 60
4.6 A schematic illustration of the current injected by 2+3 QuIC on the time domain. The fields of photon frequency ω and $\frac{3\omega}{2}$ share the same repetition rate and offset frequency, denoted by f_{rep} and f_{off}, respectively. 62
4.7 A picture of the experimental 2f-3f setup. 64
4.8 A schematic diagram of the first 2f-3f self-referencing interferometer, where the second harmonic of 1040-nm OFC and the third harmonic of 1560-nm OFC are generated and beat against each other to create a beat note at f_{off}. 64
4.9 A schematic illustration of why the beat note of the green harmonics is the offset frequency. 66
4.10 Top: the spectra of the third harmonic of the 1560-nm frequency comb generated with different modulation periods of PPLN. Bottom: the spectrum of the second harmonic of the 1040-nm frequency comb. 67
4.11 The offset frequency of the optical oscillator measured by 2f-3f self-referencing interferometer. The bandwidth (red double arrow) of the offset frequency is $\sim 400KHz$. 68
4.12 Concept of the direct feed-forward method for stabilization of CEP. For maximum diffraction efficiency into first order (red comb modes), the Bragg condition $2\lambda_{ac}sin(\alpha) = \lambda n$ has to be fulfilled. $\alpha = \alpha_{in} = \alpha_{out}$ is the Bragg angle, λ_{ac} the acoustic wavelength, λ the optical wavelength, and n the refractive index. adapted from Ref. [11] 69
4.13 A schematic diagram of the optical part of the feed-forward loop. The post-AOM offset frequencies of the 1040-nm OFC and the 1560-nm OFC are 20 KHz and 56 KHz, respectively. 70
4.14 The RF-circuit part of the feed-forward loop. The two frequencies on the right are the driving signals of two AOMs. 71

4.15 The beat note (blue curve) with an FWHM of ∼ 1Hz from the second 2f-3f self-referencing interferometer. The frequency spectra when blocking 1560 nm light (orange curve) and 1040 nm light (grey curve). 73
4.16 5 runs of free-running oscillator offset frequency measurement. The offset frequency drifts out of ±1.5MHz (the grey region) within a few minutes. . 74
4.17 The spectrum of the bandpass filter with an FWHM of 4.2 MHz. 74
4.18 The spectrum of the oscillator offset frequency picked out by the bandpass filter. 75
4.19 A schematic illustration of the beam geometry when the driving frequency of the 1560-nm beam has a slow drift. 76
4.20 The oscillator offset frequency as a function of the backend voltage (black dots). A linear equation (red line) fits the measurement with a good number of 0.9978. 77
4.21 A schematic diagram of the feedback loop. 77
4.22 The oscillator offset frequency stabilized by the feedback loop. The red arrows denote the times when the offset frequency is manually perturbed. 78
4.23 The spectrum of the light after the temporal-overlap-checking BBO. The second harmonics of 1040-nm light and 1560-nm light, the 1040-nm peaks are labeled. The SFG of 1040 nm and 1560 nm is highlighted as it indicates the temporal overlap. 79
4.24 The 2+3 QuIC current from the horizontal electrode pair as a function of time. The four colored regions from left to right show the 2+3 QuIC current detected at 32 KHz, 32 KHz + 5 Hz, 32 KHz + 10 Hz, and 32 KHz + 20 Hz, respectively. The fields of 1040 nm and 1560 nm are co-linearly polarized across the horizontal electrode pair (⟨100⟩ crystal axis). 80
4.25 The 2+3 QuIC current (black dots) from the horizontal electrode pair as a function of time. The detection frequency is 128 KHz. A sine function (red curve) fits the 2+3 QuIC current. The fields of 1040 nm and 1560 nm are co-linearly polarized across the horizontal electrode pair (⟨100⟩ crystal axis). The piezo oscillation amplitude and frequency are ∼780 nm and 0.5 Hz, respectively. 81
4.26 (a) the 1+2 QuIC current from the horizontal electrode pair (red curve) detected at 2 KHz as a function of time. (b) the 2+3 QuIC current from the hot=rizontal electrode pair (red curve) detected at 128 KHz as a function of time. In both figures, the polarization of two-color light fields is rotated with an angular frequency of $9 \circ /s$, which results in the amplitude modulation of the relative-phase-induced oscillations. The cross marks denote the peaks of current oscillations. The piezo oscillation and polarization rotation manipulate the current simultaneously. 84

4.27 A schematic diagram of the 1+2 QuIC polarization dependence setup. A prism pair separates (denoted by a BS for simplicity) the 1040 nm light and its second harmonic. The two half-wave plates on the two arms of the two-color interferometer rotate at the same angular rate simultaneously. A PZT dithers the 1040-nm arm at 2 KHz. Two Lock-in Amplifiers measure 2+3 QuIC currents from the horizontal and vertical electrode pairs. . . . 84
4.28 A schematic diagram of the 2+3 QuIC polarization dependence setup. The feed-forward and feedback loops stabilize and control the offset frequencies of 1040-nm OFC and 1560-nm oFC. The two half-wave plates on the two arms of the two-color interferometer rotate at the same angular rate simultaneously. Two Lock-in Amplifiers measure 2+3 QuIC currents from the horizontal and vertical electrode pairs. 85
4.29 An example of the injection rate of carriers on the "ring" in the $\boldsymbol{k}$-space. The darkness of the color denotes the injection rate. The red double arrow denotes the polarization of the two-color light field $\boldsymbol{k}_p$ 86
4.30 (a) A schematic illustration of 1+2 QuIC on the semiconductor band structure. (b) A schematic illustration of 2+3 QuIC on semiconductor band structure. In both graphs, the polarization of the two-color field is denoted by the red arrow. 86
4.31 (a) The polar plots of 1+2 QuIC currents from the vertical electrode pair and horizontal electrode pair. (b) The polar plots of 2+3 QuIC currents from the vertical electrode pair and horizontal electrode pair. In both graphs, the vertical QuIC currents are fitted by the theory (solid curves). The + (red) and − (purple) signs indicate the sign of QuIC current. . . . 88
4.32 (a) polar plot of the fitted injection rate of carriers in the $\boldsymbol{k}$-space. (b) polar plot of the fitted injection rate of carriers in the $\boldsymbol{k}$-space. In both graphs, the two-color light field (red double arrow) is linearly polarized across the horizontal electrode pair. 89
4.33 Polar plots of the fitted injection rate of carriers in the $\boldsymbol{k}$-space when the relative phase of the fields of 1040 nm and 1560 nm is: (a) $\frac{3\pi}{2}$, (b) π, (c) $\frac{\pi}{2}$. The two-color light field (red double arrow) is linearly polarized across the horizontal electrode pair. 90
4.34 (a) 1+2 QuIC currents from the horizontal electrode pair (red dotted line) and vertical electrode pair (black dashed line) are plotted as functions of the polarization of 520-nm light field. The 1040-nm light field is linearly polarized across the horizontal electrode pair. (b) 1+2 QuIC currents from the horizontal electrode pair (red dotted line) and vertical electrode pair (black dashed line) are plotted as functions of the polarization of 1040-nm light field. The 520-nm light field is linearly polarized across the horizontal electrode pair. In both graphs, the colored regions denote the variances. . 91

4.35 (a) 2+3 QuIC currents from the horizontal electrode pair (red dotted line) and vertical electrode pair (black dashed line) are plotted as functions of the polarization of 1040-nm light field. The 1560-nm light field is linearly polarized across the horizontal electrode pair. (b) 2+3 QuIC currents from the horizontal electrode pair (red dotted line) and vertical electrode pair (black dashed line) are plotted as functions of the polarization of 1560-nm light field. The 1040-nm light field is linearly polarized across the horizontal electrode pair. In both graphs, the colored regions denote the variances. . 91

B.1 A schematic illustration of QuIC current inside beam focal spots when the wavefronts are mismatched. The relative phases at different locations are labeled. The black arrows denote the direction of QuIC currents. 101

B.2 (a) The 2+3 QuIC current from the horizontal electrode pair when the sample is 20 μm inside (optimal - 20 μm). (b) The 2+3 QuIC current from the horizontal electrode pair when the sample is 20 μm outside (optimal + 20 μm). 101

LIST OF APPENDICES

A Ohmic Contact Fabrication **98**

B Wavefront Mismatch **100**

ABSTRACT

This dissertation presents the first comparison of the polarization dependence of the photocurrents generated in 1+2 QuIC and 2+3 QuIC. We also show the first observation of 1+2 QuIC current from Ohmic-contact AlGaAs devices. We demonstrate that the optical frequency combs (OFC) are capable of providing a two-color light field with a controllable relative phase, which is vital to 2+3 QuIC generation. The feed-forward technique is effective in reducing the bandwidth of the offset frequency and offers tunability to the detection frequency of 2+3 QuIC.

We first discuss our results from the 1+2 QuIC setup. We generate 1+2 QuIC photocurrent from AlGaAs devices, which have two types of metal-semiconductor contact - Schottky contact and Ohmic contact. We detect the QuIC currents at the dither frequency of one of the arms of the two-color interferometer. We show that the oscillation of the relative phase results in the oscillation of QuIC current. The amplitude of the QuIC current responds to the oscillations of both optical arms. The QuIC current from the Ohmic-contact AlGaAs device has a more linear external-resistance dependence than that from the Schottky-contact AlGaAs device, which indicates a current source nature of the Ohmic-contact QuIC device.

We then discuss our results on the 2+3 QuIC current, which is detected at a phase ramp directly related to the offset frequencies of two OFCs. We present the detection-frequency dependence of 2+3 QuIC current, which validates the bandwidth reduction of the offset frequencies. The sinusoidal dependence of 2+3 QuIC current on the optical

path delay is consistent with the optical injection theory.

We finally show the QuIC currents measured from two perpendicular Ohmic-contact electrode pairs in 1+2 QuIC and 2+3 QuIC. We observe the change of QuIC currents when two co-linearly polarized light fields rotate together. The fitting of experimental data with an angular current density model shows evidence for the $\boldsymbol{k}$-space localization of 2+3 QuIC. We also extract the injection rate tensor elements from one-color polarization dependencies of 1+2 QuIC and 2+3 QuIC. Our study shows the potential of 2+3 QuIC as a tool for high $\boldsymbol{k}$-space-resolution band anisotropy studies.

CHAPTER 1

Introduction

Quantum Interference Control (QuIC) is the manipulation of a system due to the interference of two independent pathways, A and B, coupling the same initial and final states. The interference, contributing constructively or destructively to the transition amplitude [6], is effectively a "matter interferometer," where the laser phase is a key control parameter. For example, as shown in Fig. 1.1 c [1], the contributions of mode-locked laser pulses at frequencies ω_a and $\omega_a/2$ to the n = 1 image-potential state interfere constructively on the right side (green box) and destructively on the left side (red box) in reciprocal space.

QuIC was first theoretically explored by Manykin and Afanas'ev [12] back in 1967 when they proposed the suppression of transition rates by quantum interference of multiple-photon transitions. The early progress on QuIC was from the studies on molecular processes [13]. In 1986, Brumer and Shapiro [12] proposed a scheme where weak phase-coherent optical fields excite an initial superposition state to alter product ratios in unimolecular decay and photodissociation. In 1989, Kurizki et al. [14] applied the same idea to semiconductors for photocurrent generation without a bias voltage. The interference of one- and three-photon processes was proposed by Shapiro et al. [15] in 1988 and demonstrated by Chen et al. [16] in 1990. The QuIC of one- and two-photon processes in the photoionization of continuum states in a photomultiplier

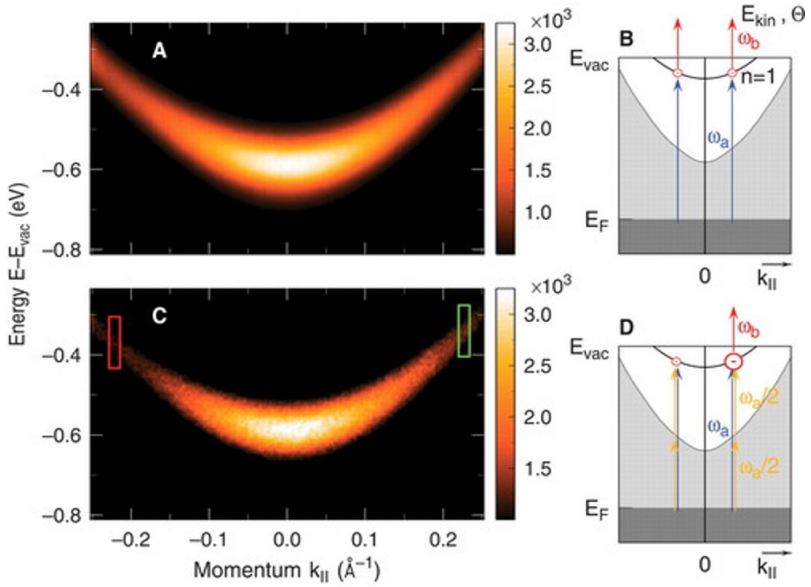

Figure 1.1: (A) $E(k_{||})$ 2PPE spectrum of the n = 1 image-potential state on the Cu(100) surface. Energies are referred to as the vacuum level E_{vac}. The color scale indicates the photoemission intensity. (B) Energy diagram of the corresponding excitation and photoemission scheme together with the surface-projected bulk band structure of Cu(100), where $E_{vac} - E_F = 4.64$ eV. Filled and empty projected bulk bands are marked by dark and light shades. The solid curve depicts the n = 1 image-potential band. (C) $E(k_{||})$ spectrum of the n = 1 state for excitation with two phase-locked laser pulses at frequencies ω_a and $\omega_a/2$ as depicted in (D). The 2PPE spectra in (A) and (C) have been recorded with zero time delay of the photoemission pulse ω_b. adapted from Ref. [1]

was observed by Baranova et al. [17, 18, 19] in 1990.

Over the last few decades, QuIC has been extensively studied both for fundamental research and applications. It has been explored in a wide variety of systems, which include atomic gases [16, 20, 21, 22], semiconductors [23, 24, 25, 26]. Sun et al. [27] have shown that QuIC is suitable for injecting and detecting ballistic currents unbiased epitaxial graphene at 300 K. QuIC has been applied to the study of waveform and vectorial arrangement of optical fields by Shawn et al. [28]. QuIC has also been proven to be powerful in detecting and controlling the carrier-envelope comb offset frequency of a mode-locked laser [29, 30].

Although the conventional wisdom is that the ultrafast decoherence processes would make QuIC processes challenging to observe in solids, Atanasov et al. [31] predicted the current injected by the two-color coherent field to be sufficiently large to be measurable. The fundamentals of photocurrent in semiconductors will be further discussed in Chapter 2. Current flow induced by QuIC in semiconductors has been theoretically predicted in multiple-beam free-carrier absorption [32], photoionization of doublet donor states [14], or band-band transition in bulk semiconductors. GaAs is often considered the hydrogen atom of semiconductor physics and is the benchmark for many experiments. In 1997, Hache' et al. experimentally observed the first QuIC of current in GaAs using electrodes to collect the accumulated charge displacement [23, 33]. In semiconductors with spin-orbit coupling, the angular momentum of light can be transferred to the injected carrier in a QuIC experiment, yielding spin-polarized carriers [34]. These carriers were predicted to form pure spin currents without accompanying electrical currents. Pure spin currents were experimentally observed in GaAs by Stevens et al., and in ZnSe by Huebner et al. [35, 36]. in 2003. In noncentrosymmetric semiconductors, QuIC has been shown by Fraser et al. to be capable of manipulating the carrier population [37] in 1999. However, in all the previous experiments where the QuIC currents of one-

and two-photon absorptions were directly detected, the metal-semiconductor contacts have Schottky barriers, which give non-ideal current transmission. We will discuss our results on 1+2 QuIC current with Ohmic contacts in Chapter 3.

Compared to the early studies of QuIC, which is mainly related to the phase-coherent ω and 2ω field, there have only been a few studies on higher-order QuIC processes [20, 38]. The non-integer QuIC is desirable because it doesn't require octave-spanning spectra to detect the offset frequency of mode-locked lasers. QuIC of two- and three-photon optical absorptions (2+3 QuIC) in AlGaAs has been studied both for fundamental research [39, 40, 41] and applications [42]. More importantly, recent theoretical studies predicted 2+3 QuIC to be desirable for studying band anisotropy [10, 41]. However, our understanding of the carrier distribution in QuIC is still limited, especially for higher-order QuIC processes. There have been a few experimental studies related to carrier distribution in QuIC. Yin et al. [22] measured the relative phase dependence of one- and two-photon photoionization processes at four different angles, which showed the k-space distribution of photoelectrons to a limited extent. The $\boldsymbol{k}$-space carrier distribution was also explored by Guedde et al. [1] with the time- and angle-resolved photoelectron spectroscopy at five different angles. However, a better-resolved carrier distribution is needed to study carrier localization in higher-order QuIC processes.

Two main ways of detecting QuIC in semiconductors are THz emission detection and direct photocurrent detection. With the 2+3 QuIC process, we aim to develop optical phase-sensitive photodetectors. The THz emission cannot deliver the information of the k-space carrier distribution. Therefore, we directly measure the photocurrents extracted by electrodes in 1+2 QuIC and 2+3 QuIC as a tool to study the k-space carrier distribution, which we will discuss in Chapter 4.

CHAPTER 2

Photocurrent Generation with Quantum Interference Control (QuIC)

2.1 Introduction to Photocurrent

The photocurrent is the current induced by illumination in photosensitive devices. To form a photocurrent, the key is to achieve the movement of charges in space with the energy from illumination. The charges deviate from their original state and move towards a direction macroscopically. Early studies on photocurrent have revealed that many effects can move charges in this manner, such as the photoconductive effect, the photovoltaic effect, and the photoelectric effect. The photoconductive effect is an extrinsic effect in which a material absorbs photons to generate electrons and holes that move in opposite directions under a bias electric field. The photoelectric effect is an intrinsic effect where the electrons are emitted into space when the material is under electromagnetic radiation. The photovoltaic effect is an extrinsic effect where the illumination of crystals can induce absorption and generate photocurrents or photovoltages. The formations of photocurrent in the effects mentioned above are different from each other. For example, both the photoconductive effect and photovoltaic effects push electrons outside their orbits. However, the electrons in the photoconductive

effect stay within the material, whereas electrons are emitted from the material to outside in the photoelectric effect. In addition, the photovoltaic effect excites electrons from a low-energy state in the conduction band to a higher-energy state in the valence band. Those excited electrons are called hot carriers, moving freely inside the material. The vacancies the electrons leave behind are referred to as holes. The movement of the electrons in the photovoltaic effect doesn't rely on a bias field. A straightforward example is the working mode of a photo-detector. The photo-diode signals generated from zero-bias and biased modes are due to the photovoltaic effect and photoconductive effect, respectively.

The photovoltaic effect (PVE) has the most extended history among these light-matter interactional effects. The early studies primarily focused on the PVEs resulting from inhomogeneity in crystals or nonuniform illumination. For example, the Dember effect is caused by a nonuniform illumination of the crystal. Also, in P-N junctions, the separation of nonequilibrium carriers due to crystal inhomogeneity gives rise to a current flowing from the N region to the P region under illumination. In the 1960s, the bulk photovoltaic effect was observed in uniform noncentrosymmetric crystals under homogeneous illumination. The bulk photovoltaic can generate photovoltage of tens of thousands of volts, which is several orders of magnitude higher than the band gap. The fact that the generation of photocurrents is related to the second-order nonlinear susceptibility opens opportunities to study the optical-electro properties of various materials. It also allows people to study the carrier generation and recombination processes from the dynamics of electrons and holes within the medium.

More importantly, the idea that the broken inversion symmetry in the $\boldsymbol{k}$-space results in a nonzero photocurrent was introduced by bulk photovoltaic effects. The "principle of detailed balancing" is invalid in bulk noncentrosymmetric crystals. In other words, the probability of excited carriers transferring from momentum $\boldsymbol{k}$ to momentum $-\boldsymbol{k}$ does

not equal the probability of excited carriers moving from momentum $-\boldsymbol{k}$ to momentum $\boldsymbol{k}$. The imbalanced carrier distribution in the $\boldsymbol{k}$ space results in a ballistic photovoltaic current. Both ballistic and shift photovoltaic currents can be affected by the crystal structure and polarization of light. This generation mechanism of photovoltaic currents is similar to the origin of quantum interference control of carriers. That being said, the generation of bulk photovoltaic currents relies on the noncentrosymmetry of the crystal, while QuIC can arise from centrosymmetric materials. In addition, QuIC is also different from the photoelectric effect because it does not rely on a bias electric field for the electron-hole separation.

Why are semiconductors suitable medium for QuIC? Firstly, the translational symmetry of bulk crystalline media permits continuum states. All the conduction and valence band states, coupled with the excitation pulses, can contribute to the injected current. In molecular systems, QuIC usually only targets a particular quantum state and/or breaks a particular bond in the presence of rapid decoherence phenomena. Secondly, the electron-hole and electron-electron scattering processes require conservation of momentum under restrictive selection rules. Thus, the scattering time of injected carriers in semiconductors is much longer than in amorphous media or even large molecules. These two reasons make QUIC current generation in solids more amenable than other forms of QUIC phenomena.

2.2 Introduction to Energy Band Structure

We denote the wave function of an electron with $\psi(z)$. Assume we have an independent electron under a periodic potential:

$$U(\boldsymbol{r}) = U(\boldsymbol{r} + \boldsymbol{R}) \tag{2.1}$$

The wave function of a Bloch electron is an energy eigenstate and a Bloch state, which can be written as:

$$\psi(r) = e^{i\boldsymbol{k}\cdot\boldsymbol{r}} u(\boldsymbol{r}) \tag{2.2}$$

where $u_k(x)$ has a boundary condition: $u_{\boldsymbol{k}}(\boldsymbol{r}) = u_{\boldsymbol{k}}(\boldsymbol{r} + \boldsymbol{R})$ According to Bloch's theorem, the wave function of electrons in the crystal reflects the periodicity of the lattice potential. So we have:

$$\psi(\boldsymbol{r} + \boldsymbol{R}) = e^{i\boldsymbol{k}\cdot R}\psi(\boldsymbol{r}) \tag{2.3}$$

The eigenfunction u_k and its energy E_k can be obtain by solving the following equation:

$$[-\frac{\hbar^2}{2m_0}\frac{\partial^2}{\partial \boldsymbol{r}^2} + U(\boldsymbol{r})]\psi(\boldsymbol{k}) = E_k\psi(\boldsymbol{k}) \tag{2.4}$$

The solutions form the band structure of electrons in crystals. For each $\boldsymbol{k}$, there is an infinite number of eigenfunctions and energy states. E_k has a periodicity due to the periodic crystal potential. The band structure of semiconductors such as GaAs can be simplified into a 4-band model with an electron band (conduction band), a heavy hole band, a light hole band, and a split-off band.

$Al_xGa_{1-x}As$ alloy is the material we used to generate QuIC in the two experiments discussed later in the thesis. It has the same crystal structure as GaAs. A layer of $Al_xGa_{1-x}As$ (x=0.28) oriented along $\langle 001 \rangle$ crystal axis is epitaxially grown on GaAs substrate. The band gap of AlGaAs can be engineered by changing the Al fraction. The band gap of the AlGaAs we used is 1.77 eV, based on the practical relation between

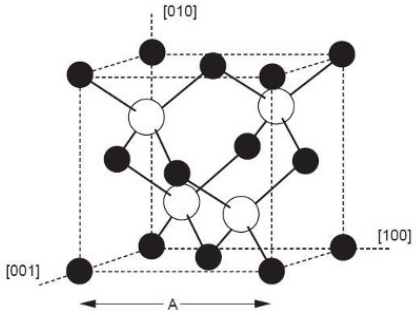

Figure 2.1: The lattice structure of GaAs bulk crystal[2].

the energy band gap of AlGaAs and Al concentration (for $x < 0.45$)[ref]:

$$E_{g,dir}(x) = 1.422eV + x1.2475eV \tag{2.5}$$

The GaAs lattice has inversion symmetry with respect to the center of the unit cell shown in Fig. 2.1. The interference of the two carrier injection pathways breaks the inversion symmetry in the $\boldsymbol{k}$-space, creating relative-phase-dependent injected currents. There are different types of QuICs, such as QuIC of carrier injection, QuIC of carrier population, and QuIC of spin current. QuIC usually means the quantum interference control of carrier injection in this thesis if not further specified. The inversion symmetry is broken along other crystal axes such as $\langle 111 \rangle$. The QuIC of carrier population, where the density of carriers is dependent on the relative phase of the two colors, arises from the broken inversion symmetry of the crystal. [ref]

2.2.1 The band structure of GaAs

In the band structure of GaAs, the conduction band has three minima: one at k = 0 (called the Γ point), another along $\langle 111 \rangle$ directions at the boundary of the first Brillouin zone (called L). As shown in Fig. 2.2, this minimum is 0.29 eV lower than the Γ

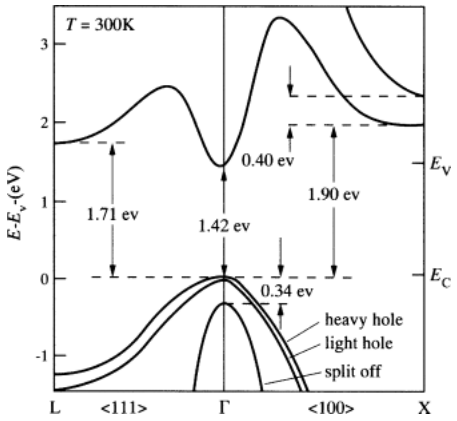

Figure 2.2: The band structure of GaAs[3].

minimum. The third minimum is near the zone boundary along (100) directions (the Δ line) and is 0.48 eV higher than the Γ minimum. There are three valence bands, which all have a maximum at $\boldsymbol{k} = 0$. The heavy hole and light hole bands are degenerate at $\boldsymbol{k} = 0$. In crystals with strong spin-orbital coupling, such as GaAs, the split-off band is separated from the other two valence bands and more parabolic. For most semiconductors, the spin-orbit coupling is much larger, and the split-off band is not typically populated by holes (e.g., in GaAs, $\Delta so = 0.35\text{eV}$). When the conduction band minimum doesn't occur at the same point as the valence band maximum, the semiconductor is referred to as an $indirect - gap$ semiconductor. It is not impossible to generate electron-hole pairs in an indirect band gap material. Due to the momentum preservation law, the electrons injected from the top of the valence band need to emit a phonon to reach the bottom of the conduction band, which makes indirect-gap absorption strength susceptible to temperature. As shown in Fig. 2.2, GaAs is a $direct - gap$ semiconductor. The direct band gap is desirable for optical injections. The electrons can be injected from the valence band to the conduction band by photons without phonon assistance. The momentum of electrons is not affected by the injection process. The electrons in the semiconductor crystal without illumination or bias field are

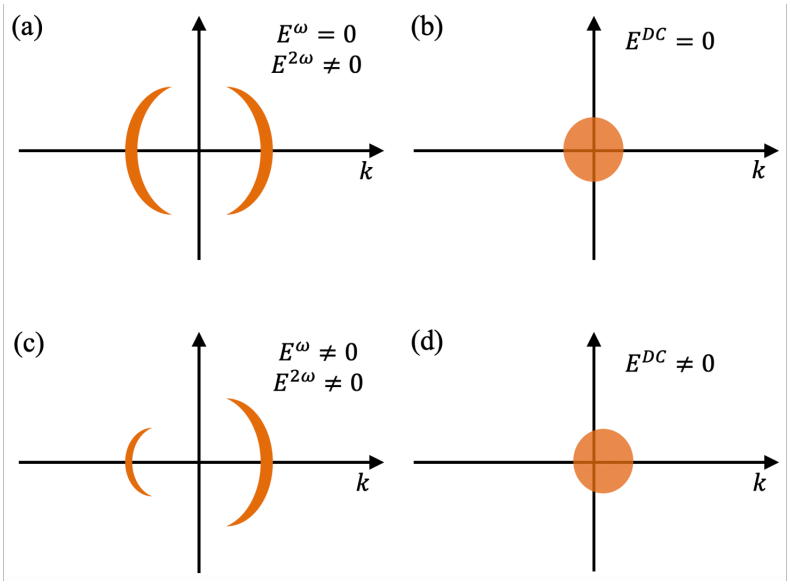

Figure 2.3: The carrier distributions in the $\boldsymbol{k}$-space when (a) $E^{\omega} = 0, E^{\omega} \neq 0$ (b) $E^{DC} = 0$ (c) $E^{\omega} = 0, E^{\omega} \neq 0$ (d) $E^{DC} \neq 0$. Reproduced from Ref. [4]

sketched in Fig. 2.3 (b), where $\boldsymbol{k}$ states are filled up to the Fermi surface. Compared to Fig. 2.3 (b), the optically injected carriers in one-color absorption, as shown in Fig. 2.3 (a), are further away from $\boldsymbol{k} = 0$. In addition, the injected carrier distribution is more anisotropic. The velocity of carriers in Fig. 2.3 (d) needs to go through an acceleration process. In contrast, the velocity of carriers in Fig. 2.3 (c) is directly given by the instantaneous photon absorption process on the fs time scale. Also, the DC bias method needs a large electric field to achieve the "herding" of statistically distributed electrons. Therefore, the QuIC process is a more efficient way of current production compared to the conventional DC field method.

At $\boldsymbol{k} = 0$, the conduction and split-off valence bands are approximately parabolic. The energy dispersion of GaAs band structure $E(\boldsymbol{k})$ can be approximately expressed by[43]:

$$E(\boldsymbol{k}) = \frac{\hbar^2 k^2}{2m_e} \tag{2.6}$$

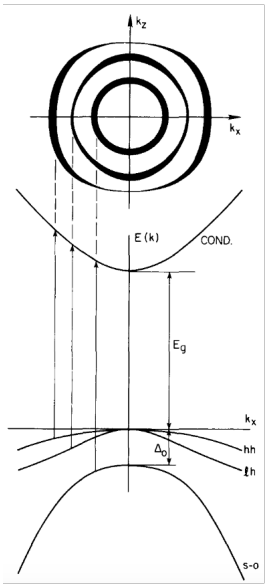

Figure 2.4: The upper part of the figure is a schematic illustration of the distribution of excited carriers in optical absorption in $k_x - k_z$ plane. The lower part of the figure is a simplified sketch of the band structure of GaAs. The light is linearly polarized along $\langle 010 \rangle$ crystal axis. The photon energy is large enough to reach the three valence bands. adapted from Ref. [5]

The sign of effective mass m_e is positive for the conduction band and minus for the valence band. When electrons are excited by photons with larger photon energy to the conduction band, they are far away from $\boldsymbol{k} = 0$ in the $\boldsymbol{k}$-space. When $\boldsymbol{k}$ is large, the energy dispersion has a nonparabolicity[43], which is described by:

$$E(1 + \alpha E) = \frac{\hbar^2 k^2}{2m_e} \tag{2.7}$$

The $k \cdot p$ perturbation theory has been widely used for calculating the band structure of crystals. The periodic Bloch state function u_{nk} can be obtained by solving a

Schrödinger equation that contains the $k \cdot p$ Hamiltonian H_k:

$$H_k u_{nk}(r) = E_k u_{nk} \tag{2.8}$$

$$H_k = H_0 + \frac{\hbar}{m} k \cdot p + \frac{\hbar^2 k^2}{2m} \tag{2.9}$$

$$v(k) = \frac{1}{\hbar} \frac{\partial}{\partial k} H_k \tag{2.10}$$

For zinc-blende crystals, the 14 band $k \cdot p$ model cannot fully capture the band structure features outside 0.5 eV above and below the semiconducting band gap. 30 band $k \cdot p$ model can predict the optical response above 0.5 eV. It has also been applied to calculations of optical injection in GaAs and Ge and coherent control in Ge.

In light absorption processes of GaAs, the distribution of excited electrons in the conduction band has inversion symmetry around $\boldsymbol{k} = 0$. More importantly, the distribution is anisotropic due to the dipole matrix elements between the conduction and valence bands. When light is incident on the GaAs crystal, if the photon energy is larger than the bandgap at Γ point (1.424 eV), the electrons from the three valence bands are excited to three corresponding "rings" in the conduction band, as shown in Fig. 2.4. Each "ring" represents the strength of optical transition with its width and the momentum of excited electrons with its diameter.

The optical absorption strength depends on the number of states available for electrons and the matrix elements. The heavy-hole-related electrons are distributed more along k_x, and the "ring" is not perfectly circular. The light-hole-related electron distribution maximizes along the direction of light polarization. As mentioned earlier, the conduction band is isotropic near $\boldsymbol{k} = 0$. Therefore, the anisotropy is mainly due to

the warping of valence bands. This also shows the heavy hole and light hole bands have opposite warpings.

The density of states (DOS) quantitatively defines the number of states available for occupation in a small range in the momentum space and energy space. The DOS in $\boldsymbol{k}$-space can be written as:

$$\frac{Number\ of\ electron\ states}{Volume\ of\ k-space} = N_k = 2 \times \frac{L^d}{(2\pi)^d} \tag{2.11}$$

where d is the dimensionality, L is the sample size, and the factor of 2 is due to spin degeneracy.

The nonparabolicity flattens out the energy band and increases the DOS. It is easier to calculate the density of state for semiconductors with higher symmetry. And it is often more useful to express DOS in energy space rather than in momentum space. DOS in the energy space is related to the dispersion relations of the crystal. For parabolic energy bands, the density of the state of 3D carriers can be expressed by:

$$g_c(E) = \frac{m_e}{\pi^2\hbar^2}k = \frac{m_e\sqrt{2m_eE}}{\pi^2\hbar^3} \tag{2.12}$$

2.3 How do the electrons and holes move inside crystals?

We simplify optical carrier injection by only considering the conduction band and light hole valence band. The excitation light is normally incident on the crystal. As shown in Fig. 2.5, the transitions are vertical in the energy band diagram because the momenta of electrons and holes are preserved. That is to say, the electrons before and after light injection have the same k vector. If we only consider the right side of the bands in Fig.

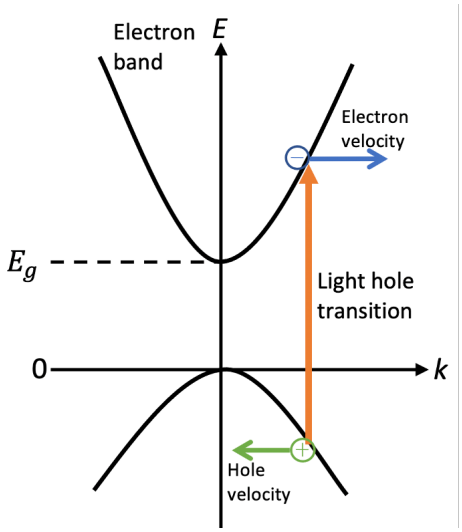

Figure 2.5: The generation of an electron-hole pair in optical absorption. The velocities of the electron and hole are indicated by the blue and green arrows, respectively.

2.5, the electron velocity in the conduction band can be expressed as:

$$v_e = [2\frac{2\hbar\omega - E_g}{m_e(1 + m_e/m_\hbar)}]^{1/2} \tag{2.13}$$

where E_g is the energy gap of GaAs. When an electron-hole pair is generated, the electron and hole carry the same momentum in opposite directions. The speed of holes can be obtained from $v_h m_h = v_e m_e$ if the energy bands are parabolic. Based on Eq. 1.6, the effective mass of an electron is defined as:

$$(m_e)^{-1} = \frac{1}{\hbar^2}\frac{\partial^2 E}{\partial k^2} \tag{2.14}$$

The effective mass of electrons is related to the curvature of energy bands. Thus, electrons have negative mass on the top of the valence band and positive mass on the conduction band. Since the holes carry positive charges, the sign of their effective mass is opposite to the electrons' effective mass. So, the velocity of holes on the light hole band is in the opposite direction to that of electrons, which is indicated by the arrows

in Fig. 2.5. Although electrons and holes are moving in opposite directions on one side of the bands, overall, one color excitation cannot induce a net current from an unbiased bulk AlGaAs crystal. This is because the carriers injected at $\boldsymbol{k}$ and $-\boldsymbol{k}$ cancel out. This is also how QuIC generates injected currents. Namely, the imbalance of the injected currents at $\boldsymbol{k}$ and $-\boldsymbol{k}$ results in a net current sensitive to the relative phase of the two involved excitation frequencies. Moreover, if we only consider electrons and view holes as vacancies of electrons, we can see that the electron's velocity changes direction as it goes from the valence band to the conduction band. This change of momentum comes from the lattice. In coherent control, there is initially no net current in the crystal, and then after excitation, there is a net current moving in a certain direction. The momentum of that current came from the lattice recoil.

The electron-hole pairs generated from above-gap excitations are fundamentally different from excitons. Excitons are hydrogen-like quasi-particles where electrons and holes are bound through the Coulomb force. Similar to the energy structure of hydrogen atoms, excitons have discrete energy levels based on the number of electrons in a quasi-particle. The type of exciton is related to how strongly bonded the electrons and holes are. The excitons redshift the electron conduction band by the Coloumb potential. The excitation photon energy is above the band gap in the current injection process. The electrons and holes have opposite momenta, which makes the center of mass momentum zero. On the contrary, the exciton states are usually below the conduction band. Excitons carry a crystal pseudomomentum equivalent to the vector sum of the individual momenta of the electron and the hole and their relative momentum. In other words, for excitons, electrons and holes move in the same direction, and the momentum of the center of mass is nonzero.

2.4 Oblique Incidence of Light in Photocurrent Injection

Light at normal incidence cannot induce a current in unbiased ⟨001⟩ oriented bulk GaAs. Would an oblique incidence result in a current comparable to the QuIC current? Now we consider an excitation light incident on a ⟨001⟩ oriented GaAs crystal at an oblique angle of 70°. We assume the wavelength of excitation is centered at 520 nm with a bandwidth of 20 nm. In direct optical transitions, the crystal will absorb most of the photons. The refraction index of GaAs n_1 is ∼3.8. Therefore, inside the crystal, the angle between the direction of propagation and the normal direction from the surface will be $arcsin(sin(70°)/n1) \sim 14°$. As shown in Fig. 2.6, each photon injects one electron from the valence band to the conduction band. The total photon energy corresponds to the red arrow. It is tilted because the photon momentum component parallel to the sample surface is transferred to the injected electrons. The tilting is towards the same direction on both sides of the bands, which, in principle, will result in a net current. However, the current is fairly insignificant compared to the QuIC current. We assume that the two optical pathways interfere perfectly constructively on the right side and perfectly destructively on the left side. Then, the strength of the QuIC current is related to the momentum of carriers injected to the right side of the conduction band, indicated by the green arrow in Fig. 6. The photon energy contributing to the vertical transition is 2.31 eV, indicated by the black arrow. Note that the lattice parameter of GaAs is 5.65 angstroms. According to the electron conduction band of GaAs, the injected electrons are centered around $k_1 = 1.4 \times e^9\ m^{-1}$. The average momentum of the electrons is $\hbar k_1 = 1.477 \times e^{-25} kg \cdot m/s$. The electrons do not all have the same exact momentum. The broadening of carriers on the conduction band is mainly related to the energy span of excitation, the band curvature, and the density of states. We simplify the

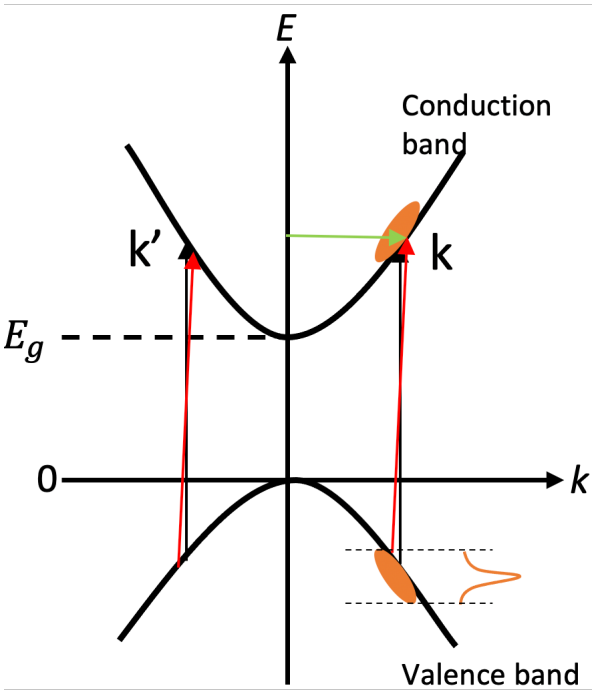

Figure 2.6: The carriers injected by the QuIC process on the band structure. The interference of the two pathways is constructive at $\boldsymbol{k}$ and destructive at $\boldsymbol{k}'$. The crystal is GaAs (E_g=1.43 eV). The total photon energy is 2.31 eV. The red and black arrows correspond to the optical transitions when the incidence of light is oblique and normal, respectively. The green arrow denotes the $\boldsymbol{k}$ vector of injected carriers.

energy span of carriers on the conduction band to the span of excitation photon energy from 2.27eV to 2.36eV. The variation of electron momentum is $\sim 6 \times e^{-26} kg \cdot m/s$ The momentum of photon can be expressed as: $k_{photon} = frac\hbar\lambda = 2.03 \times e^{-28} kg \cdot m/s$. The component of the photon momentum that is parallel to the surface can be expressed as $k_{photon} sin(14°) = 4.9 \times e^{-29} kg \cdot m/s$. From the calculation above, we get that the momentum of electron given by the parallel component of photon momentum is $\sim 3 \times e^4$ times smaller than that given by the optical injection. Moreover, the momentum of electrons given by the parallel component of photon momentum is even much smaller than the variation of electron momentum due to excitation bandwidth. Therefore, the net current caused by the oblique incidence alone is negligible.

2.5 1+2 QuIC Theory

The content in this section referenced the work done by Professor John. Sipe's group [6]. For one electron in the crystal, the Hamiltonian H_0 can be written as:

$$\frac{p^2}{2m} + V(r) + H_{s-o} \tag{2.15}$$

where p is the momentum operator, $V(r)$ is the periodic crystal lattice potential. m is the bare mass of the electron. The spin-orbit coupling Hamiltonian can be written as:

$$H_{s-o} = \frac{\hbar}{4m^2c^2}\sigma \cdot (\boldsymbol{\nabla} \times p) \tag{2.16}$$

$\sigma = 2S/\hbar$ is the dimensionless spin operator. The momentum operator can be rewritten in the presence of a spatially uniform EM field.

$$p \to p - \frac{e}{c}A(t) \tag{2.17}$$

where $A(t)$ is the vector potential of the field and $e = -\|e\|$ is the charge of the electron. The overall Hamiltonian of electrons consists of the single-electron Hamiltonian H_0, the electron-photon interaction Hamiltonian $H_1(t)$, and Hamiltonian $H_2(t)$ that only affects the overall phase of $|\psi(t)\rangle$

$$H_1(t) = -\frac{e}{mc}A(t) \cdot P \tag{2.18}$$

$$H_2(t) = \frac{e^2}{2mc^2}|A(t)|^2 \tag{2.19}$$

The expectation of single-particle operator θ should satisfy the following conditions: (a) the expectation in the ground state is 0. (b) the operator can't excite the ground state: $\langle cvk|\,\theta\,|0\rangle = 0$. (c) only the electron states or hole states with the same crystal momentum can be involved in the operation: $\left\langle c^{'}v^{'}k^{'}\right|\theta\left|cvk\right\rangle = \left\langle c^{'}v^{'}k\right|\theta\left|cvk\right\rangle \delta_{kk'}$. where $|cvk\rangle$ is the state representing the perturbative term in the electron-hole pair wave function.

We use $\langle\theta\rangle$ to stand for the expectation $\langle\psi(t)|\theta|\psi(t)\rangle$. Then the (m,n)-order of the time derivative of $\langle\theta\rangle$ can be written as:

$$\frac{\partial\left\langle\theta\right\rangle^{(m,n))}}{\partial t} = 2\pi\sum_{cc'vv'k}\left(\langle c'k|\theta|ck\rangle\,\delta_{vv'} - \langle v'k|\theta|vk\rangle\,\delta_{cc'}\right)\times\Omega_{cv}^{(n)}\left(w,k\right)\delta[\lambda_{cv}^{(n)}(w,k)] \tag{2.20}$$

The m and n can be interpreted as m- and n-photon absorption in the optical absorption process. When one-photon and two-photon absorption are present, the $\Omega_{cv}(k)$ in equation can be written as:

$$\Omega_{cv}(k) = \Omega_{cv}^{(1)}(2\omega,k) + \Omega_{cv}^{(2)}(\omega,k) \tag{2.21}$$

We first consider that there is a monochronic field with a frequency 2ω incident on the sample. The field can be expressed as:

$$E(t) = E(2\omega)e^{-i2\omega t} + c.c. \tag{2.22}$$

In Eq. 24, the observable $\langle\theta\rangle$ can be carrier density or spin density. Therefore, the rate of injection of carriers excited by one-photon absorption is given by:

$$\dot{n} = \xi_1^{ab}(2\omega)E^{a*}(2\omega)E^{b}(2\omega) \tag{2.23}$$

where the carrier injection tensor is:

$$\xi_1^{ab}(2\omega) = \frac{2\pi e^2}{\hbar^2\omega^2}\sum_{c,v}\int \frac{d^3k}{8\pi^3} v_{cv}^{a*}(\boldsymbol{k}) v_{cv}^{b}(\boldsymbol{k})\delta[\omega_{cv}(\boldsymbol{k}) - 2\omega] \tag{2.24}$$

The matrix elements of the velocity tensor $\boldsymbol{v}_{mn}(k)$ can be derived with the Bloch states of bands m and n at wavevector $\boldsymbol{k}$:

$$\left\langle m\boldsymbol{k} \left| \boldsymbol{v} \right| n\boldsymbol{k}^{'} \right\rangle = v_{mn}(\boldsymbol{k})\delta(\boldsymbol{k} - \boldsymbol{k}^{'}) \tag{2.25}$$

Some of the elements in $\xi_1^{ab}(2\omega)$ are identical under crystal symmetry. The zinc-blende lattice for GaAs results in only one independent nonzero component:

$$\xi_1^{xx} = \xi_1^{yy} = \xi_1^{zz} \tag{2.26}$$

Also, ξ_1 can be expressed as a function of the imaginary part of the susceptibility $\chi(2\omega)$:

$$\xi_1(2\omega) = \frac{2Im[\chi(2\omega)]}{\hbar} \tag{2.27}$$

Now, we consider a light with a frequency of ω triggering two-photon absorption. The rate of injection of carriers can be written as:

$$\dot{n}_2(\omega) = \xi_2^{abcd}(\omega)E^{a*}(\omega)E^{b*}(\omega)E^{c}(\omega)E^{d}(\omega) \tag{2.28}$$

$$\xi_2^{abcd}(\omega) = \frac{2\pi e^4}{\hbar^4\omega^4}\sum_{c,v}\int \frac{d^3k}{8\pi^3} w_{cv}^{ab*}(\boldsymbol{k}) w_{cv}^{cd}(\boldsymbol{k})\delta[\omega_{cv}(\boldsymbol{k}) - 2\omega] \tag{2.29}$$

where $\omega_{cv}^{ab}(\boldsymbol{k})$ is the symmetrized two-photon amplitude:

$$w_{cv}^{ab}(\boldsymbol{k}) \equiv \frac{1}{2}\sum_{m}\frac{v_{cm}^{a}(\boldsymbol{k})v_{mv}^{b}(\boldsymbol{k})+v_{cm}^{b}(\boldsymbol{k})v_{mv}^{a}(\boldsymbol{k})}{\omega_{m}(\boldsymbol{k})-\overline{\omega}_{cv}(\boldsymbol{k})} \tag{2.30}$$

$\xi_2^{abcd}(\omega)$ has 21 nonzeros and three independent components under zic-blende lattice symmetry.

$$\xi_2^{xxxx} = \xi_2^{yyyy} = \xi_2^{zzzz} \tag{2.31}$$

$$\xi_2^{xxyy} = \xi_2^{yyzz} = \xi_2^{zzxx} = \xi_2^{xxzz} = \xi_2^{yyxx} = \xi_2^{zzyy} \tag{2.32}$$

$$\xi_2^{xyxy} = \xi_2^{yzyz} = \xi_2^{zxzx} = \xi_2^{xzxz} = \xi_2^{yxyx} = \xi_2^{zyzy} = \xi_2^{xyxy} = \xi_2^{yzzy} = \xi_2^{zxxz} = \xi_2^{xzzx} = \xi_2^{yxxy} = \xi_2^{zyyz} \tag{2.33}$$

Similar to one-photon absorption, the two-photon absorption amplitude can be expressed as a function of χ^3:

$$\xi_2(\omega) = \frac{3Im[\chi^3(\omega;-\omega,\omega,\omega)]}{\hbar} \tag{2.34}$$

In the case of 1+2 quantum interference, the incident optical field consists of two frequencies ω and 2ω. Assuming that ω is smaller than the band gap, the two-photon absorption of $\hbar\omega$ and one-photon absorption of $2\hbar\omega$ will happen simultaneously. The two-color light field can be expressed as:

$$E(t) = E(\omega)e^{-i\omega t} + E(2\omega)e^{-2iwt} + c.c. \tag{2.35}$$

where

$$E(\omega) = E_\omega e^{i\varphi_\omega}\hat{e}_\omega, \quad E(2\omega) = E_{2\omega}e^{i\varphi_{2\omega}}\hat{e}_{2\omega} \tag{2.36}$$

The injection rate of $\langle\theta\rangle$ has two terms caused solely by the two absorption processes and another term representing the interference.

$$\frac{\partial \langle\theta\rangle}{\partial t} = \frac{\partial \langle\theta\rangle_1}{\partial t} + \frac{\partial \langle\theta\rangle_2}{\partial t} + \frac{\partial \langle\theta\rangle_I}{\partial t} \tag{2.37}$$

$$\frac{\partial}{\partial t}\langle\theta\rangle_1 = \Theta_1 : E^*(2\omega)E(2\omega) \tag{2.38}$$

$$\frac{\partial}{\partial t}\langle\theta\rangle_2 = \Theta_2 : E^*(\omega)E^*(\omega)E(\omega)E(\omega) \tag{2.39}$$

$$\frac{\partial}{\partial t}\langle\theta\rangle_I = \Theta_I : E^*(\omega)E^*(\omega)E(2\omega) \tag{2.40}$$

Eq. 1.24 can be rewritten as:

$$\frac{\partial}{\partial t}\langle\theta\rangle_{I;e} = 2\pi\sum_{cvk}(\langle ck|\theta|ck\rangle - \langle vk|\theta|vk\rangle) \times \Omega_{cv}^{(2)*}(\omega,k)\Omega_{cv}^{(1)}(2\omega,k)\delta[\omega_{cv}(k) - 2\omega] + c.c. \tag{2.41}$$

where

$$\Omega_{cv}^{(1)}(\omega,k) = \Upsilon_{cv}^{(1)}(\omega,\boldsymbol{k}) \cdot E(\omega) \tag{2.42}$$

$$\Omega_{cv}^{(2)}(\omega,k) = \Upsilon_{cv}^{(2)}(\omega,\boldsymbol{k}) : E(\omega)E(\omega) \tag{2.43}$$

Therefore, we have the coefficient in the interference term as:

$$\Theta_I = 2\pi \sum_{cvk} (\langle ck|\theta|ck\rangle - \langle vk|\theta|vk\rangle) \times \Upsilon^{(2)*}_{cv}(\omega, k)\Upsilon^{(1)}_{cv}(2\omega, k)\delta[\omega_{cv}(k) - 2\omega] \tag{2.44}$$

Note that

$$\Upsilon^{(1)}_{cv}(\omega, \boldsymbol{k}) = \frac{ie}{\hbar\omega} v_{cv}(\boldsymbol{k}) \tag{2.45}$$

$$\Upsilon^{(2)}_{cv}(\omega, \boldsymbol{k}) = \frac{e^2}{\hbar^2\omega^2} \sum_n \frac{v_{cn}(\boldsymbol{k})v_{nv}(\boldsymbol{k})}{\omega_n(\boldsymbol{k}) - \overline{\omega}_{cv}(\boldsymbol{k})} \tag{2.46}$$

$$\overline{\omega}_{mn}(k) \equiv (\omega_m(\boldsymbol{k}) + \omega_n(\boldsymbol{k}))/2 \tag{2.47}$$

$$\tag{2.48}$$

The rate of the observable $\langle\theta\rangle$ can be rewritten as:

$$\left\langle \dot{\theta} \right\rangle_I = |E_\omega|^2 |E_{2\omega}| \left(Re[\Theta_I : \hat{e}^*_\omega \hat{e}^*_\omega \hat{e}_{2\omega}] cos(\Delta\varphi^{realtive}_{1+2}) + Im[\Theta_I : \hat{e}^*_\omega \hat{e}^*_\omega \hat{e}_{2\omega}] sin(\Delta\varphi^{realtive}_{1+2})\right) \tag{2.49}$$

where the relative phase parameter is defined as below:

$$\Delta\varphi^{realtive}_{1+2} \equiv 2\varphi_\omega - \varphi_{2\omega} \tag{2.50}$$

The rate of the interference term of observable $\left\langle \dot{\theta} \right\rangle_I$ can be the rate of the density of injected carriers, the rate of injected current, or the rate of injected spin current. The magnitude and sign of the observable can be controlled by the relative phase of the light fields of two optical frequencies. Experimentally, it has been shown that QuIC can lead to the injection of ballistic charge current[24, 23**?**] or pure spin current[35].

2.5.1 Carrier Population Control

In noncentrosymmetric materials, the crystal can absorb the incident light in two-photon absorption if the imaginary part of χ_2 is nonzero. More importantly, when coherent fundamental and sum-frequency beams are simultaneously present in a crystal, $Im[\chi_2]$ results in the energy transferring from the two frequencies to carrier injection.

The rate of total injection of carriers is:

$$\dot{n} = \dot{n_1}(2\omega) + \dot{n_2}(\omega) + \dot{n_I}(\omega) \tag{2.51}$$

The one- and two-photon terms are related to the imaginary parts of the even rank tensors $\chi_1(-2\omega; 2\omega)$ and $\chi_3(-\omega; -\omega, \omega, \omega)$ respectively. These two terms exist for any material. The interference term of the density of injected carriers $\dot{n}_I$ is only present in the materials lacking enter of inversion symmetry. It can be expressed as:

$$\dot{n}_I(\omega) = -\xi_I^{abc} E^{a*}(\omega) E^{b*}(\omega) E^c(2\omega) + cc. \tag{2.52}$$

$\xi_I^{abc}(\omega)$ is defined by Fraser et al.:

$$\xi_I^{abc}(\omega) = -\frac{i\pi e^3}{\hbar^3 \omega^3} \sum_{cv} \int \frac{d^3k}{8\pi^3} w_{cv}^{ab*}(\boldsymbol{k}) v_{cv}^c(\boldsymbol{k}) \delta[\omega_{cv}(\boldsymbol{k}) - 2\omega] \tag{2.53}$$

$\xi_I^{abc}(\omega)$ only has one independent nonzero component in zinc-blende crystals:

$$\xi_I^{xyz} = \xi_I^{xzy} = \xi_I^{yzx} = \xi_I^{yxz} = \xi_I^{zxy} = \xi_I^{zyx} \tag{2.54}$$

This component is purely real in the independent-particle approximation. It can be

expressed as a function of the second-order susceptibility:

$$\xi_I(\omega) = \frac{2Im[\chi^{(2)}(-2\omega, \omega, \omega)]}{\hbar} \tag{2.55}$$

The dependence of the density of injected carriers on the relative phase of a 1550 nm beam and its second harmonic is shown as the change in the differential transmission. The two beams are orthogonally polarized with the 1550 nm beam's polarization aligned parallel to crystal $\cdot \langle 011 \rangle$ axis to maximize the χ_2 contributions.

2.5.2 Injection Current Control

The interference term can generate a current that can be controlled by the relative phase parameter $\Delta\varphi_{1+2}^{relative}$:

$$\frac{d}{dt} \langle J^a \rangle_{1+2} = \eta_{1+2}^{abcd}(3\omega) E_{3\omega/2}^{b*} E_{3\omega/2}^{c*} E_{3\omega}^{d} + c.c. \tag{2.56}$$

$$j_I^a = \eta_I^{abcd}(\omega) E^{b*}(\omega) E^{c*}(\omega) E^d(2\omega) + c.c. \tag{2.57}$$

$$j_I^a = \eta_I^{abcd}(\omega) E^{b*}(\omega) E^{c*}(\omega) E^d(2\omega) + c.c. \tag{2.58}$$

$$\eta_{\substack{l:e \\ (h)}}^{abcd}(\omega) = (-)\frac{i\pi e^4}{\hbar^3\omega^3} \sum_{cv} \int \frac{d^3k}{8\pi^3} v^a_{\substack{cc \\ (vv)}}(\boldsymbol{k}) w_{cv}^{bc*}(\boldsymbol{k}) v_{cv}^d(\boldsymbol{k}) \delta[\omega_{cv}(\boldsymbol{k}) - 2\omega] \tag{2.59}$$

$$\eta_e^{abcd}(\omega) = \frac{i\pi e^3}{\hbar^3\omega^3} \sum_{cv} \int \frac{d^3k}{8\pi^3} w_{cv}^{bc*}(\boldsymbol{k}) v_{cv}^d(\boldsymbol{k}) \delta[\omega_{cv}(\boldsymbol{k}) - 2\omega] \tag{2.60}$$

$$\eta_{1+2}^{abcd}(\omega) = \frac{i4\pi e^3}{27\hbar^3\omega^3}\sum_{cv}\int\frac{d^3k}{16\pi^3}[\sum_{m}\frac{v_{cm}^{b}(\boldsymbol{k})v_{mv}^{c}(\boldsymbol{k})+v_{cm}^{c}(\boldsymbol{k})v_{mv}^{b}(\boldsymbol{k})}{\omega_m(\boldsymbol{k})-\overline{\omega}_{cv}(\boldsymbol{k})}]^{*}v_{cv}^{d}(\boldsymbol{k})\delta[\omega_{cv}(\boldsymbol{k})-3\omega] \tag{2.61}$$

The imaginary part of $\eta_{\substack{l:e\\(h)}}^{abcd}(\omega)$ has been calculated in a span of photon energy for GaAs. As shown in Fig. 2.7, there is a threshold around the band gap of GaAs, which indicates that the above-gap excitations contribute to the QuIC injection current. Since $\eta_{\substack{l:e\\(h)}}^{abcd}(\omega)$ is purely imaginary, the injection rate can be written as:

$$\dot{J}_I^a = Im[\eta_I^{abcd}(\omega)]sin(\Delta\varphi_{1+2}^{relative})\left|E^b(\omega)\right|\left|E^c(\omega)\right|\left|E^d(2\omega)\right| + c.c. \tag{2.62}$$

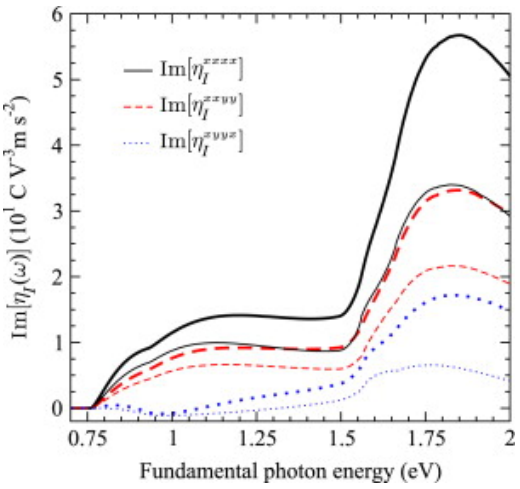

Figure 2.7: The calculated imaginary parts of injection coefficient tensor elements as functions of fundamental photon energy for intrinsic GaAs at room temperature. adapted from Ref. [6]

The control of carrier population and the control of injected current are different in many aspects. Firstly, the carrier population has a scalar dependence on the relative phase parameter, whereas the control of the injected current's direction depends on the relative phase. Secondly, from a macroscopic point of view, the control of carrier popu-

lation is caused by the sum of the interfering amplitudes at $\boldsymbol{k}$ and $-\boldsymbol{k}$. But the injected current originates from the difference of the injection rates at $\boldsymbol{k}$ and $-\boldsymbol{k}$. Thirdly, the control population is related to $\chi_2(-2\omega;\omega,\omega)$ whereas the control of injected current originates from the most divergent part of $\chi_3(0;-2\omega,\omega,\omega)$. Lastly, in semiconductors such as GaAs, the two phenomena arise from different polarization schemes and crystal cuts. For example, the control of carrier population can arise in $\langle 111\rangle$ oriented GaAs with orthogonally polarized lights. In contrast, the control of injected current appears in $\langle 001\rangle$ oriented GaAs with co-linearly polarized lights.

2.5.3 Swarm Velocity

Swarm velocity is defined as the average velocity of the injected carriers. Swarm velocity represents the efficiency of the carrier injection. It can be written as:

$$\boldsymbol{v}_s = \frac{\dot{\boldsymbol{J}}}{e\dot{n}} \tag{2.63}$$

where $\dot{J}$ is given by Eq. 1.62. and $\dot{n}$ is given by Eq. 1.56. The swarm velocity maximizes when the following conditions are satisfied: a) $sin(2\varphi_\omega - \varphi_{2\omega}) = 1$. b) the one- and two-photon absorption are balanced: $\dot{n}_1(2\omega) = \dot{n}_2(\omega)$. The interference term $\dot{n}_I$ is zero for linearly polarized beams. Assuming the polarizations of two beams are co-linearly align to $\langle 100\rangle$, the maximum of swarm velocity is:

$$v_{s,max}^{\langle 100\rangle} = \frac{Im[\eta_I^{xxxx}(\omega)]}{e\sqrt{\xi_1^{xx}(2\omega)\xi_2^{xxxx}(\omega)}} \tag{2.64}$$

2.6 Carrier Scattering Mechanism

2.6.1 Hot Carrier Generation in the QuIC Process

In the light absorption process, there are different kinds of charged carriers moving inside the crystal, such as heavy holes, light holes (hh and lh), and electrons (e). The speed of different kinds of carriers in GaAs at the Γ-point as a function of photon energy is shown in Fig. 2.8. The electrons generated with heavy holes have the largest speed. The electrons (lh) and light holes have more similar velocities since their effective masses are more similar. The number of the e-hh pairs near the band edge is about three times larger than e-hh pairs. Assuming the excitation energy is 1.6 eV, 80% of the injected photocurrent is carried by the electrons. Therefore, we only consider electrons' contribution to QuIC current.

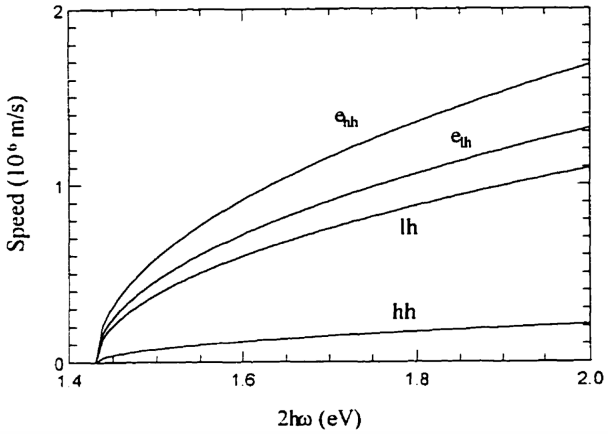

Figure 2.8: The scattering rates of different kinds of carriers as functions of total photon energy for intrinsic GaAs at room temperature. Electrons injected from the light-hole valence band, electrons injected from the heavy-hole valence band, light-holes, and heavy-holes are denoted by e_{lh}, e_{hh}, lh, and hh, respectively. [7]

2.6.2 Hot Carrier Relaxation

In this subsection, we discuss the general hot carrier relaxation processes. As discussed earlier, a population of hot carriers is injected into the conduction band from the valence band in optical absorption processes. In our case, the total photon energy (2.38 eV) is much higher than the band gap (1.77 eV). The injected carriers will distribute far away from the bottom of the conduction band. In Fig. 2.9, different carrier relaxation pathways are sketched on the band structure. $\hbar\omega_{LO}$ denotes the energy of longitudinal phonons. $\hbar\omega_p$ denotes the energy of plasmon energy. The electron-electron scattering becomes more significant when the carriers are more spread out towards the bottom of the conduction band because the scattering has to satisfy the momentum and energy conservation laws. In the quantum control of carriers process, the carriers are initially highly localized in the conduction band. Therefore, electron-electron scattering is less impactful than electron-phonon scattering in the initial stage. The injected carriers are usually called "hot carriers" because they have significant excess energy, so they can travel in crystals with large momentum. These carriers will slow down through three thermalization stages. In the first stage, the carriers go through a rapid initial relaxation where the carrier energy is reduced in units of plasmons and LO phonons. In the second stage, the carriers cool down towards lattice temperature through optical phonon scattering. However, the cooling will not be complete because optical phonons carry more energy than acoustic phonons, and they are less efficient in energy relaxation when the excess energy of carriers is reduced to a certain degree. The first two stages of thermalization usually happen within 100 ps. In the third stage, the distribution of carriers is further cooled down to lattice temperature through acoustic phonon scattering. This process is usually on the nanosecond time scale. [5]

The QuIC current is sketched as a function of time in Fig. 2.10, where the current bursts appear at the repetition rate of the laser. The rise slope of each current burst

Figure 2.9: A schematic illustration of the scattering processes involved in the carrier relaxation. adapted from Ref. [5]

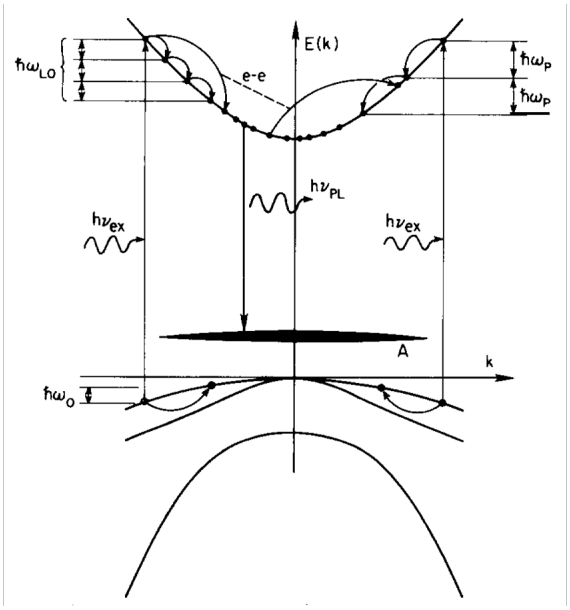

is limited by the optical pulses, and the fall slope is related to the current relaxation time. The current relaxation time is determined by the rate of all the scattering mechanisms. In general, a variety of scattering mechanisms can happen in a crystal. Inside the crystal, carriers can be scattered by defects, other carriers, and phonons. As pointed out by Auston [44], the photocurrent lifetime may be much longer than the carrier scattering time because only certain collision events will cause the current to decay. In semiconductor materials such as GaAs, the current injected by QuIC is not affected significantly by e-e, hh-hh, or lh-lh scattering. This is because the carrier-carrier scattering follows the momentum preservation rule, which is hard to achieve on a parabolic band surface. In principle, the carriers at $\boldsymbol{k}$ and $-\boldsymbol{k}$ on the same energy level can still interact with each other. However, this kind of carrier-carrier interaction is neglectable since the distribution of carriers in QuIC is highly anisotropic and non-inversion symmetric. This kind of scattering can be prominent in the QuIC of spin current because the carriers are injected more isotropically to the conduction band. It

can potentially explain the short mean free path of carriers in QuIC of spin current. In the low carrier density regime ($\rho < 10^{18} cm^{-3}$), the current relaxation is dominated by LO-phonon scattering, of which cross-section is much smaller than e-e and e-lh interactions. The current relaxation time τ_e is the sum effect of the phonon, impurity, and carrier-carrier scattering times.

$$\frac{1}{\tau_e} = \sum_i \frac{1}{\tau_i} \tag{2.65}$$

Figure 2.10: A sketch of the current injected by the QuIC process as a function of time.

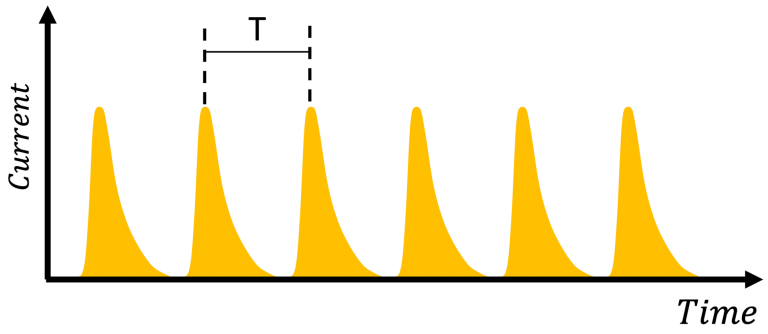

2.6.3 Phonon Scattering

Phonons are essentially the vibration of a lattice where atoms oscillate about their equilibrium sites. These vibrational lattice waves have periodicity, just like Bloch waves. For crystals with more than one different atom in the primitive cell, there are six modes of phonon waves - three acoustic modes and three optical modes. There is one longitudinal acoustic mode and two transverse acoustic modes. The adjacent atoms of acoustic modes are displaced in the same direction, whereas those of optical modes are displaced out of phase. Fig. 2.11 is the phonon energy band structure of GaAs. Optical phonons in GaAs have higher oscillation frequency around Γ point of

GaAs. And it has little dispersion near the long wavelength limit. The dispersion relation of acoustic phonons can be written as:

$$\omega(\beta) = v_s \beta \tag{2.66}$$

where v_s is the sound velocity in crystal. The distribution of thermal phonons follows the Bose-Einstein distribution, where the probability of finding phonons in a given state with a given angular frequency is:

$$n(\omega) = \frac{1}{exp(\frac{\hbar\omega}{k_B T} - 1)}, \tag{2.67}$$

k_B is the Boltzmann constant.

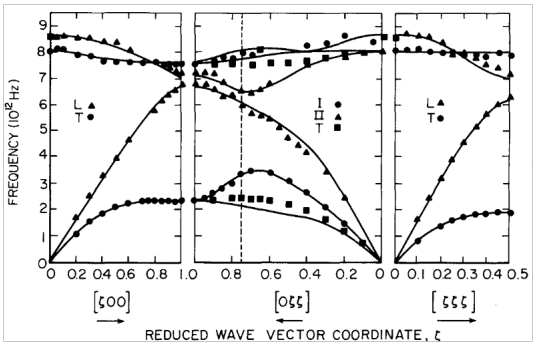

Figure 2.11: The band structure of phonons in GaAs [5]

2.6.4 Energy-momentum Conservation in Phonon Scattering

When a carrier is scattered by a phonon, both energy and momentum should be conserved. Assume $\hbar\omega(\beta)$ is the energy of the phonon. The conservation of energy can be expressed as:

$$E(\boldsymbol{p}') = E(\boldsymbol{p}) \pm \hbar\omega(\boldsymbol{\beta}) \tag{2.68}$$

If the band is parabolic, the equation can be written as:

$$\frac{p'^2}{2m^*} = \frac{p^2}{2m^*} \pm \hbar\omega(\beta) \tag{2.69}$$

In the carrier relaxation process, multiple phonon scattering events will alter the magnitude of $\boldsymbol{k}$ while preserving its directionality. For $\rho \sim 10^{15} cm^{-3}$, the scattering rate and the electron momentum relaxation time in LT-GaAs were measured to be 5.5 ps^{-1} and 185±50 fs, respectively [45]. LO-phonon emission and absorption rates in GaAs by electrons excited above the band gap have been calculated and measured by a number of groups.[46][47] At room temperature, the combined emission/absorption rate in GaAs is 8 ps^{-1} for electrons with 150 meV excess energy (this corresponds to a two-photon transition at 1.55 nm)[48]. The effective phonon scattering time τ_{LO} for an electron with excess energies $\Delta E >> E_{LO}$ can be expressed as:

$$\tau_{LO} \sim \frac{\Delta E}{R_{LO} E_{LO}} \tag{2.70}$$

where R_{LO} is the LO-phonon scattering rate. Based on the band structure of AlGaAs and the total excitation energy (2.8 eV), we know that the excess energy $\Delta E \sim 120$ eV. We use 8 ps^{-1} to estimate the scattering rate for undoped AlGaAs. The LO-phonon energy E_{LO} is $\sim$ 35eV in GaAs. For one injected electron to relax to the bottom of the conduction band, the LO-phonon scattering time is roughly 430 fs.

CHAPTER 3

1+2 Quantum Interference Control (QuIC) in AlGaAs

To our knowledge, all the previous studies on the 1+2 QuIC currents directly extracted from metal contacts were conducted with Schottky contacts. The 1+2 QuIC signals were all observed as photo-voltage signals, while the intrinsic product of the QuIC process is supposed to be current. There has been a debate on the type of electrical source the QuIC process offers. In this chapter, we show that the Schottky contact is more related to the "voltage source," and Ohmic contact is more related to the "current source."

3.1 Metal-semiconductor Contact

There are two kinds of metal-semiconductor junction-rectifying contact (Schottky barrier) and non-rectifying contact (ohmic contact). The ohmic contact between semiconductor and metal is desirable in semiconductor devices because of its low resistance. In the case of carrier injection, the carriers can tunnel through the depletion layer of ohmic contact, resulting in a better current collection than Schottky contact. One of the features of ohmic contact is that its potential barrier is very thin compared to the

Schottky barrier. The tunneling probability is a function of barrier thickness:

$$P \approx exp[-2T\sqrt{\frac{8\pi^2 m}{h^2}(V_H - E)}] \tag{3.1}$$

where $V_H - E$ is the height of the energy barrier, and m is the effective mass. The barrier thickness T can be expressed by:

$$T \approx W_{dep}/2 = \sqrt{\varepsilon_s \phi_{Bn}/(2qN_d)} \tag{3.2}$$

Therefore, the tunneling probability can be written as:

$$P \approx exp(-\frac{4\pi}{h}(\phi_{Bn} - V)\frac{1}{\sqrt{N_d}}\sqrt{\varepsilon_s m^*}) \tag{3.3}$$

and the current of tunneling electrons is:

$$J = nqv \cdot P = N_d qvexp(-\frac{4\pi}{h}(\phi_{Bn} - V)\frac{1}{\sqrt{N_d}}\sqrt{\varepsilon_s m^*}) \tag{3.4}$$

We can tell from the equation above that when $V \ll \phi_{Bn}$, J is linear in the applied voltage, which is a main characteristic of ohmic contact. The concept of specific contact resistance ($\Omega/\ cm^2$), the resistance of a 1 cm^2 contact, is introduced by the expression of current:

$$R_c \equiv \frac{V}{J} = \frac{2 \cdot e^{H\phi_{Bn}/\sqrt{N_d}}}{qvH\sqrt{N_d}} \propto e^{H\phi_{Bn}/\sqrt{N_d}} \tag{3.5}$$

where $H \equiv \frac{4\pi}{h}\sqrt{(\varepsilon_s m_n)/q}$

Five layers of Au, Ge, and Ni were deposited on the AlGaAs bulk crystal and annealed at 450 ∘C for 5 mins to create ohmic contact. The order of the five layers is Au Ni Ge Au Ni (110nm, 30nm, 20nm, 10nm, 5nm) from top to bottom. The electrode

pattern was applied to a layer of photoresist (5 μm) using photo-lithography. Before the metal deposition, the wafer with photoresist was plasma etched for 1 minute with LAM 9400. As shown in Fig. 3.2, the I-V curves of ohmic contact are linear in a wide range of voltage. The goodness number of the fitting with the linear equation is ~ 0.999, which is consistent with Eq. 2.4. The resistance of Ohmic contact ($\sim 8K\Omega$) is way smaller than that of Schottky contact ($\sim 80M\Omega$) without illumination. Based on the I-V curves in Fig. 3.3, the Schottky barriers have a much larger effective resistance than ohmic contact. The I-V curve is diode-like on the $V > 0$ side and $V < 0$ side. It can be considered as a much larger resistor when the bias voltage is small (from -100 mV to 100 mV).

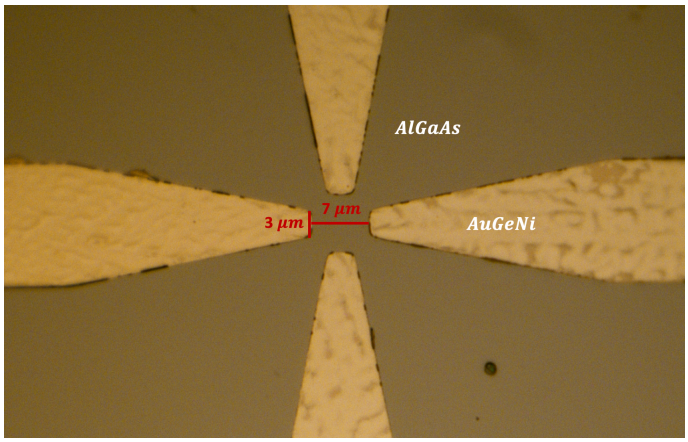

Figure 3.1: A picture of the Ohmic-contact electrodes on the AlGaAs wafer. The four tips are connected to 4 larger metal pads ($1\,mm \times 1\,mm$). The spacing between opposing electrode pairs is 7 μm. The width of each tip is 3 μm.

3.2 1+2 QuIC setup

Fig. 3.4 is a sketch of the 1+2 QuIC setup. The Second Harmonic Generation in a 100 μm BBO crystal doubles the frequency of the frequency comb, whose spectrum is centered at 1040 nm. The repetition rate of the frequency comb is 250.583 MHz.

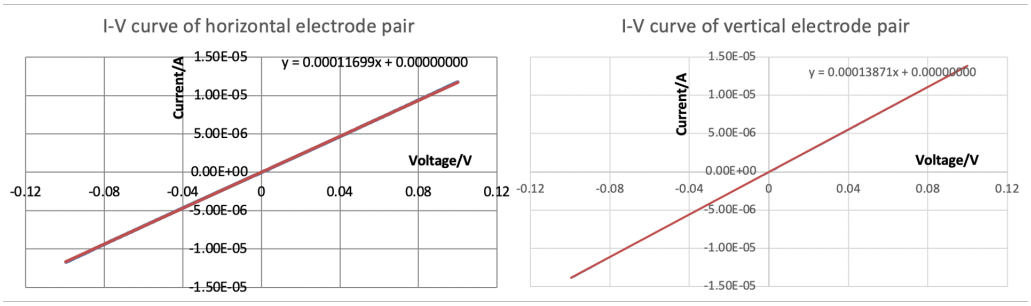

Figure 3.2: Left: the I-V curve of the Ohmic horizontal electrode pair. Right: is the I-V curve of the Ohmic vertical electrode pair. The range of applied voltage is from -100 mV to 100 mV. The resistances of these two pairs are fitted by the linear equations, denoted by the orange lines.

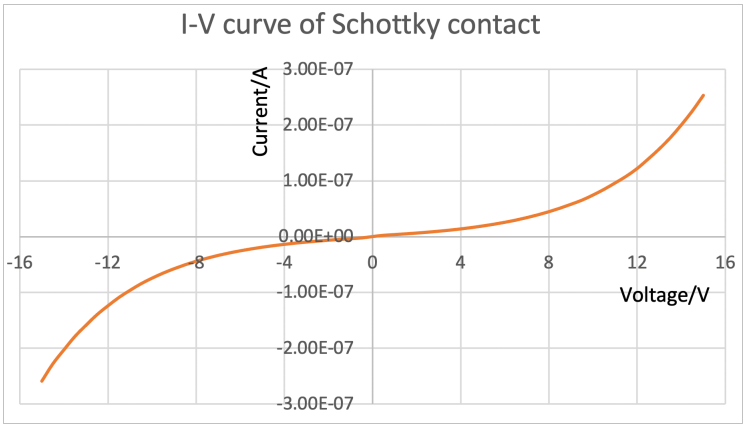

Figure 3.3: The I-V curve of a Schottky electrode pair on AlGaAs from $V_{bias} = -15\,V$ to $V_{bias} = 15\,V$.

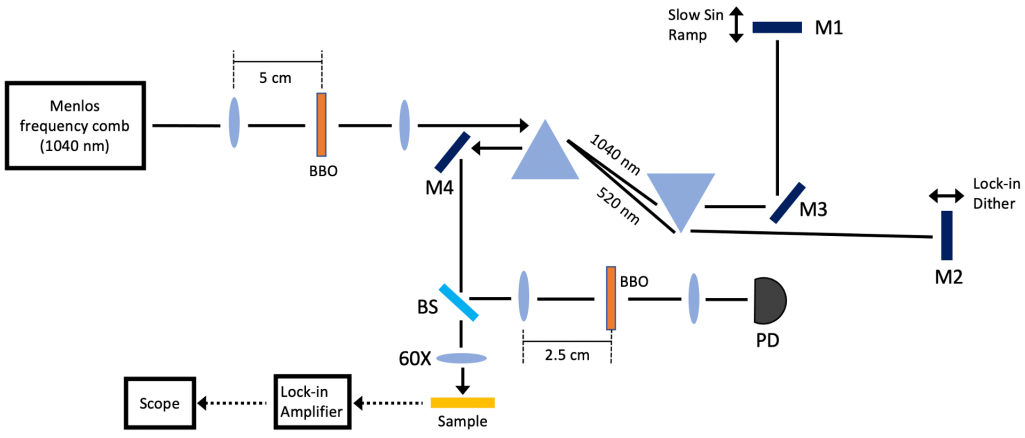

Figure 3.4: A schematic diagram of the 1+2 QuIC setup

A prism pair separates the 1040 nm light from its second harmonic spatially. The spacing between the two prisms is about 40 cm. There are pros and cons to using a prism pair to separate the two colors. On the one hand, the prism pair has more degrees of freedom regarding beam alignment optimization. In the previous method, the two colors are separated by a bandpass spectral filter. The problem with this method is that it cannot completely filter out one color from the other. The residue of 1040 nm (520 nm) light in the 520 nm (1040 nm) arm will interfere with its replica at the sample and create spatial fringes. As the delay between two arms varies, the fringes will move back and forth, generating a signal at the proposed QuIC frequency. Therefore, it will be very hard to differentiate the QuIC signal from the interference signal. Contrary to the previous method, the prism pair can perfectly separate two colors both spectrally and spatially, which inherently guarantees that the signal at slow ramp frequency is caused by quantum interference. On the other hand, the prism pair can introduce different anomalous group delay dispersions to the two colors. Therefore, the two beams need to be kept close to each other inside the prism pair. The 520-nm arm of the interferometer was dithered sinusoidally over about $\lambda/4$ at 2 KHz for lock-in detection. The 1040-nm arm was ramped sinusoidally over several wavelengths at 0.5 Hz. In the previous QuIC measurements where the Lock-in Amplifier detects at the chopper frequency, phase-insensitive single- or two-photon absorption can easily overwhelm the QIC signal. Applying oscillation to both arms eliminates irrelevant signals at the Lock-in reference frequency. The two driving voltages of Piezos are phase-stable relative to the same DDS clock. After the two arms are recombined, a fraction of the light is sent through another BBO crystal, where the second harmonic of the 1040 nm arm interferes with the 520 nm arm when they temporally overlap.

The power of the 520 nm light after BBO can be written as:

$$I = cos(\phi_{relative}) + c.c. = cos((2\omega_{520nm\ dither} + \omega_{1040nm\ slow\ ramp})t) + c.c. \tag{3.6}$$

Thus, the signal power should have the same relative-phase dependence as the QuIC signal. The oscillation of the 520-nm power should be twice the frequency of the slow ramp. Fig. 3.5 is the amplitude of the photo-detector signal detected at the dither frequency (2KHz) by the Lock-in Amplifier. The turn-around points indicate the duration of the oscillation cycle, which, in this case, is 1 second.

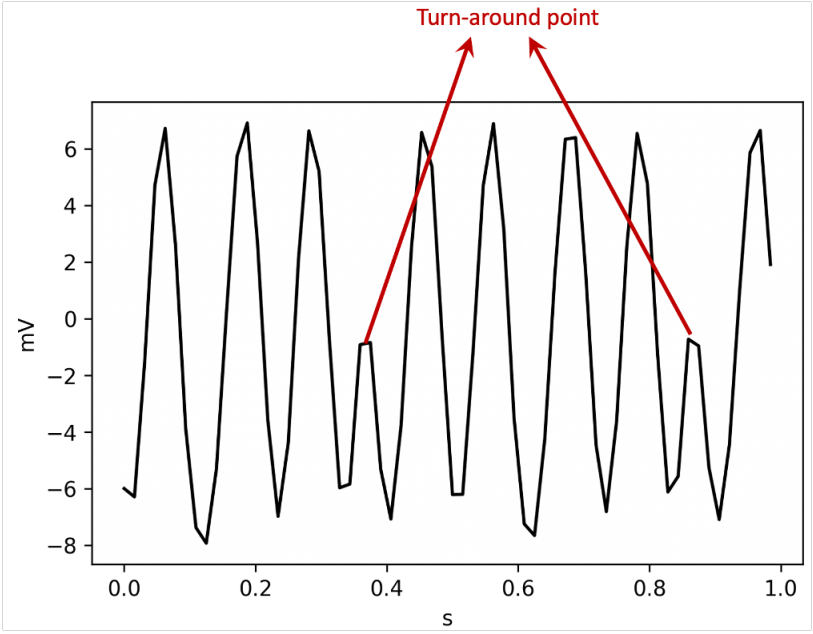

Figure 3.5: The power of the green light after the second BBO crystal is plotted as a function of time, shown as the black curve. The times when the piezo starts to move in the other direction are denoted by the red arrows. The frequency of the slow ramp is 0.5 Hz.

3.3 1+2 QuIC

3.3.1 Relative-phase Dependence

The two beams are focused at the center of the horizontal electrode pair. The two beams are co-linearly polarized. The direction of their polarization is across the electrode pair. The diameter of the focal spot of the 1040-nm beam is $\sim 2\mu m$, and the diameter of the focal spot of the 520-nm beam is $\sim 3\mu m$. The power of 1040-nm illumination is $\sim 42mW$, and the power of 520-nm illumination is $\sim 8mW$. The 1+2 QuIC current is converted to a voltage signal by external resistance, which is the load resistor of the voltage channel of the Lock-in Amplifier ($10M\Omega$) and EXTECH Resistance Decade Box ($10M\Omega$) in parallel. Fig. 3.6 is the 1+2 QuIC signal as a function of the relative temporal delay between the two pulse trains. The FWHM of the overlap envelope (∼280 fs) is consistent with the duration of the 1040-nm pulse (∼90 fs) and 520-nm pulse (∼120 fs) measured from auto-correlation. The oscillation inside the envelope indicates the phase dependence of the QuIC current. The fact that the voltage signal oscillates around 0 means that the QuIC current changes direction as the relative phase between the two quantum pathways changes. To gain resolution of each oscillation, we set the travel range of the slow sinusoidal ramp of the 1040-nm arm to be a little over one wavelength and keep the waveform as what is shown in Fig. 3.7. Now, with the same ramping frequency and sampling rate of Lock-in Amplifier, the number of data points in each oscillation is maximized. Another reason for capturing turn-around points is to get the amplitude of the QuIC signal. The reference signal of the Lock-in Amplifier is at the dither frequency of the 520-nm arm. Note that not only the oscillation depth but also the resting position of M2 needs to be adjusted. The optimal resting position is when the relative phase between two pathways is 90°. However, if the resting position is when the relative phase between two pathways is 0° or 180°, the

detection frequency of QuIC signal should be twice the dithering frequency. The same measurement was also done with a Schottky-contact sample (resistance:$100K\Omega$ under illumination) with the same contact pattern. As shown in Fig. 3.8, with the same excitation energies, the QuIC signal from the Schottky-contact sample has a smaller amplitude than the QuIC signal measured from the Ohmic-contact sample.

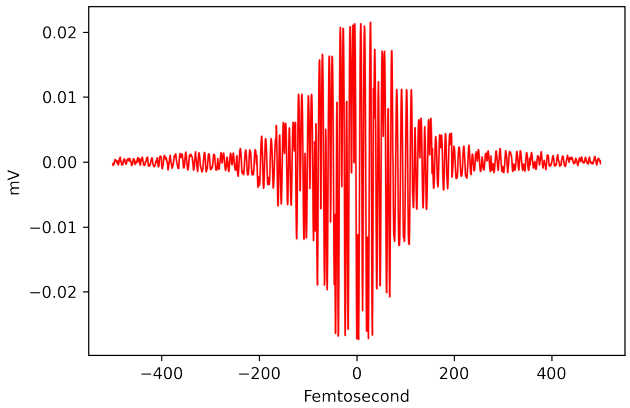

Figure 3.6: The QuIC signal from the Ohmic-contact sample detected at 2 KHz as a function of the relative time delay.

3.3.2 External-resistance Dependence

To study the type of electrical source the Schottky barrier and Ohmic contact offer, we conducted measurements on the amplitude of QuIC voltage oscillation as a function of the external resistance both on Ohmic-contact and Schottky-contact AlGaAs samples. In the experiment, the load resistance converts the current $I_{External}(t)$ to a voltage, whose average over time is read by the Lock-in Amplifier. The external resistance was varied from 0.01 $M\Omega$ to 5 $M\Omega$ by adjusting the EXTECH Resistance Decade Box. 30 cycles of phase-induce oscillation were taken at each external resistance. The amplitude of phase-induce oscillation was analyzed by averaging the peak values for different external resistances. The dependence of QuIC-induced voltage from Schottky

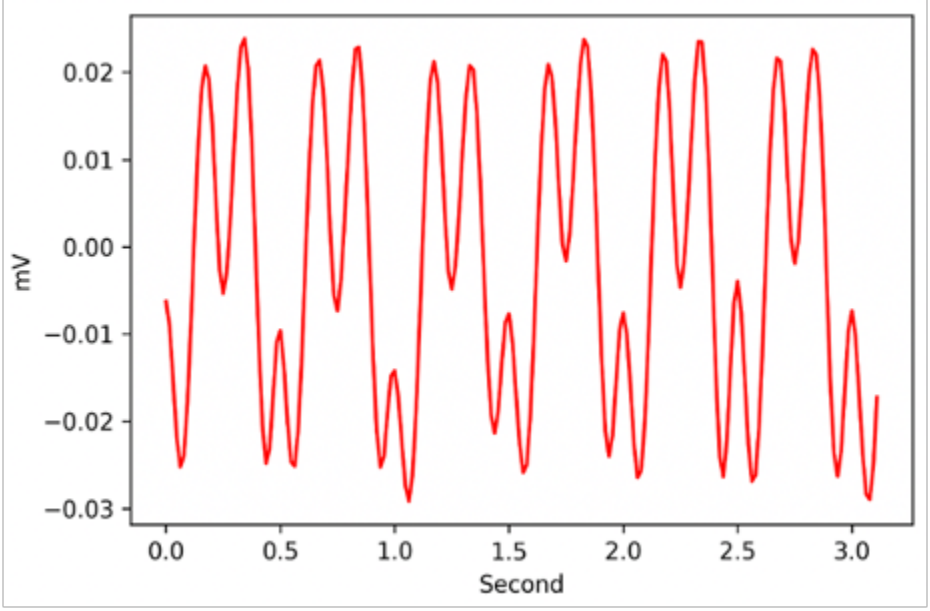

Figure 3.7: The X channel of the Lock-in Amplifier measured the relative-phase dependence of the 1+2 QuIC. The horizontal electrode pair of the Ohmic-contact sample was used. The lock-in amplifier was in voltage mode.

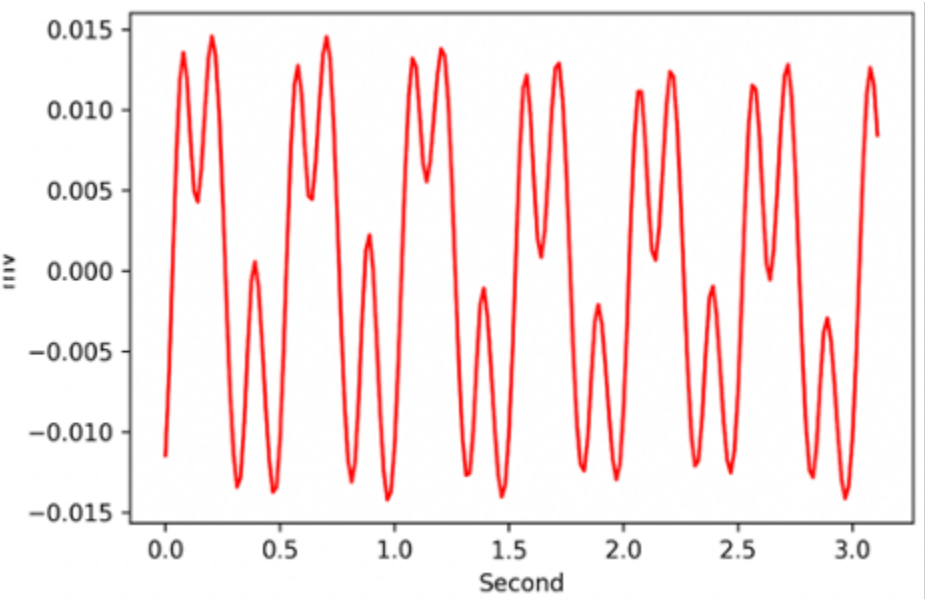

Figure 3.8: The X channel of the Lock-in Amplifier measured the relative-phase dependence of the 1+2 QuIC. The horizontal electrode pair of the Schottky-contact sample was used. The lock-in amplifier was in voltage mode.

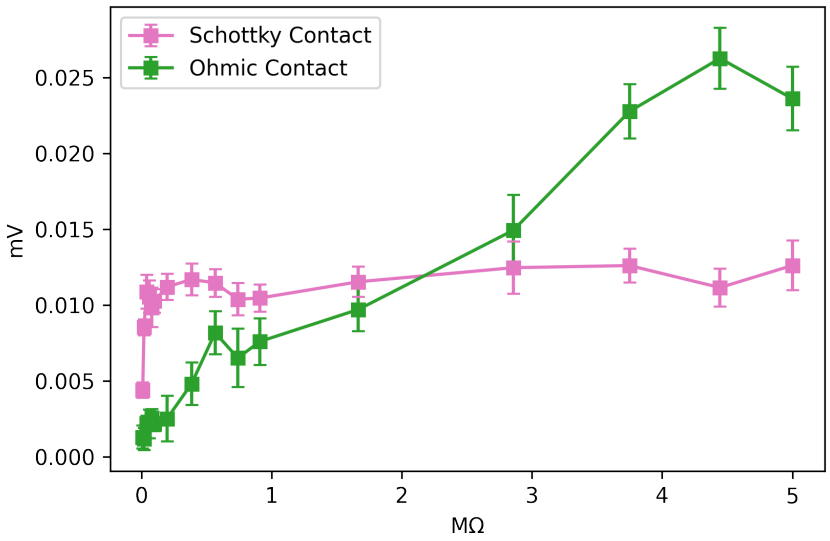

Figure 3.9: The amplitude of 1+2 QuIC from the Schottky-contact sample and Ohmic-contact sample are plotted as functions of the external resistance.

contact differs from that from Ohmic contact. As shown in Fig. 3.9, the voltage from Schottky contact rises fast in the low external resistance regime and plateaus in the high external resistance regime. In contrast, the voltage from ohmic contact has a more linear relation with external resistance in the measurement range.

We model the 1+2 QuIC measurements with electrical circuits. Fig. 3.10 (a) is the circuit with Schottky barriers, and Fig. 3.10 (b) is the circuit with ohmic contact. For Schottky contact, the metal-semiconductor-metal structure is modeled by a capacitor and a resistor in parallel. Due to the Schottky barriers, the injected carriers will accumulate around the metal-semiconductor interface, which makes the metal electrode pair effectively a capacitor. The capacitor is discharged periodically in time, which creates the current flow in the external circuit. The capacitance is denoted by $C^{MSM}_{Schottcky}$. The resistances of the two kinds of contacts are denoted by $R^{MSM}_{Ohmic}(t)$ and $R^{MSM}_{Schottcky}(t)$, respectively. The resistors R^{MSM} and R_{load} in parallel provide two discharge channels. The total current I_{Total}, resistance of device R^{MSM}, and external current $I_{External}$ vary

with time. Their periodicity is related to the repetition rate of the pulse train. For instance, we have $I_{Total}(t) = I_{Total}(t+T)$, where T is the time interval between adjacent pulses.

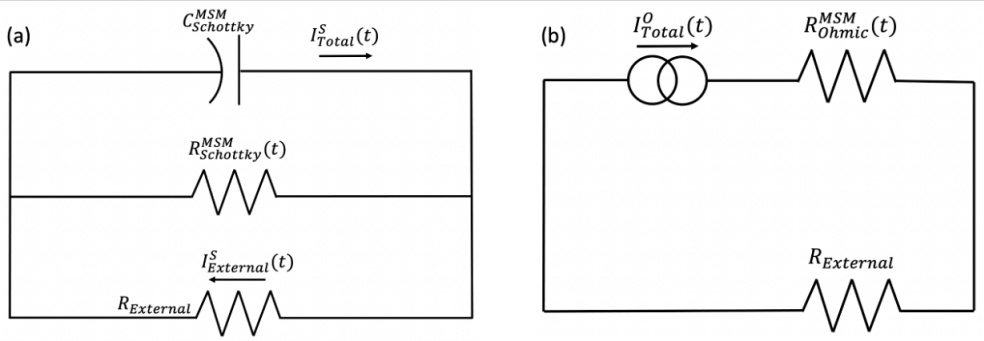

Figure 3.10: (a) A circuit diagram as a model of the Schottky-contact 1+2 QuIC detection. (b) A circuit diagram as a model of the Ohmic-contact 1+2 QuIC detection.

When the circuit is in the low external resistance regime, the total resistance of the Schottky-contact circuit can be written as: $\frac{R_{External}\, R^{MSM}_{Schottky}(t)}{R_{External}+R^{MSM}_{Schottky}(t)}$. It is larger than the total resistance of the Ohmic contact circuit since $R^{MSM}_{Schottky}(t) > R^{MSM}_{Ohmic}(t)$. We assume that $\left\langle I^{S}_{total}(t)\right\rangle$ roughly remain constants under the change of $R_{External}$ in the low external resistance regime. In this regime, $I_{Total}(t)$ is split into $R^{MSM}_{Schottky}(t)$ and $R^{MSM}_{Ohmic}(t)$. The voltage measured by Lock-in Amplifier from the Schottky-contact sample can be written as a function of external resistance: $V_{Schottky} = \frac{\langle I_{Total}(t)\rangle\, R_{External}\, \left\langle R^{MSM}_{Schottky}(t)\right\rangle}{R_{External}+\left\langle R^{MSM}_{Schottky}(t)\right\rangle}$. The experimental data from 0.01 $M\Omega$ was fitted by this function, as shown in Fig. 3.11. The fitted $\left\langle R^{MSM}_{Schottky}(t)\right\rangle$ and $\langle I_{Total}(t)\rangle$ are 23.5 $K\Omega$ and $5.4e^{-7}$ A, respectively. The $\left\langle R^{MSM}_{Schottky}(t)\right\rangle$ is close to the resistance measured with a multi-meter under the same illumination ($\sim$37 $K\Omega$). The voltage across the external resistance can also be expressed by: $\langle Q(t)\rangle / C^{MSM}_{Schottky}$. As external resistance increases, the charges transfer across the depletion layer to the metal-semiconductor interface become more saturated. Therefore, the voltage plateaus in the high external resistance regime, possibly because there are not enough charges yielding an increasing voltage.

In addition, for Schottky contact, it is harder for carriers to get through the depletion layer to the electrode pads, whereas the carriers can tunnel through the thin depletion layer easily for ohmic contact. Therefore, Schottky contact's capacitance is way larger than Ohmic contact's capacitance, which also makes the Schottky voltage plateau at a lower external resistance than Ohmic voltage. These features of the Schottky MSM device make it act like a "voltage source" that provides roughly constant voltage for a wide range of external resistance.

Different from Schottky contact, the capacitance of Ohmic contact is mostly parasitic and much lower. The charges transfer across the depletion layer through the tunneling process instead of thermionic emission. Therefore, we use the circuit in Fig. 3.10 (b) as our model, where the device provides the injected carriers as a current source. In the high external resistance regime, the voltage across the external resistor can be fitted by a linear function: $V_{Ohmic} = \langle I^o_{Total}(t) \rangle \, R_{External} + V_0$, assuming the MSM device (capacitor and internal resistance in parallel) acts like a "current source". The fitted parameters $\langle I^o_{Total}(t) \rangle$ and V_0 are $5e^{-9}$ A and 0.0018 mV respectively. As shown in Fig. 3.11, the linear trendline and the resistance dependence show a fairly good agreement. $\langle I^o_{Total}(t) \rangle$ is much smaller than $\left\langle I^S_{Total}(t) \right\rangle$, possibly because the voltage also plateaus to some degree due to the charge transfer saturation.

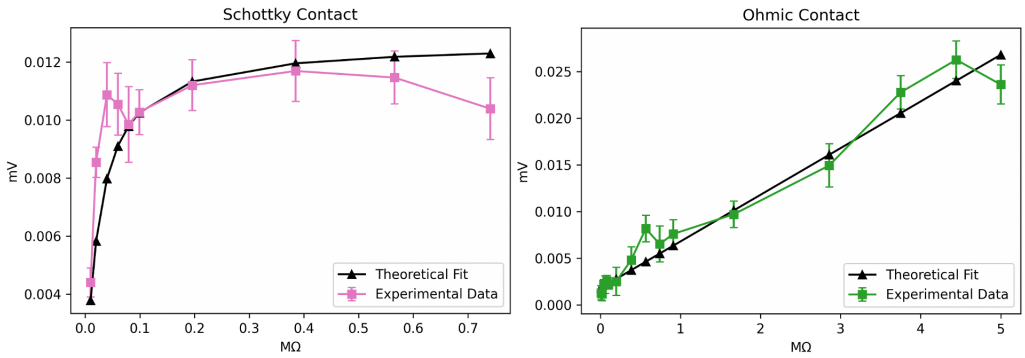

Figure 3.11: Left: the amplitude of the 1+2 QuIC from Schottky contact as a function of the external resistance (pink squares). Right: the amplitude of the 1+2 QuIC from Ohmic contact as a function of the external resistance (green squares). The fit curves are calculated based on the circuit models (black triangles).

CHAPTER 4

2+3 QuIC

Due to the higher order of optical transitions, the injected carriers in the QuIC of two- and three-photon absorptions (2+3 QuIC) have been predicted to be more localized in the $\boldsymbol{k}$-space than those in the QuIC of one- and two-photon absorptions (1+2 QuIC)[2]. This localization is desirable because it offers access to k-space microscopy with optical transitions. In this chapter, we will first demonstrate why frequency combs are suitable tools for generating 2+3 QuIC current. We will then discuss the origin of the localization of carrier distribution in the $\boldsymbol{k}$-space. The control and stabilization of the offset frequency will be discussed in detail. In the end, we will show the measurements of the detection frequency dependence, relative-phase dependence, and polarization dependence of the 2+3 QuIC current. Our analysis of the polarization dependence reveals the localization of carrier distribution in 2+3 QuIC.

4.1 Introduction to Frequency Comb

In the time domain, the frequency comb can be considered as a train of pulses with coherent phases. As shown in Fig. 4.1, the carrier-envelope phase (CEP) shift between adjacent pulses is denoted by $\omega_c T$, where ω_c is the carrier angular frequency. The time interval between adjacent pulses is denoted by T. The electric field of an optical

frequency comb can be written as a function of time:

$$\boldsymbol{E}(t) = \sum_{m=-\infty}^{\infty} \boldsymbol{\varepsilon}(t - mT)e^{i[w_c(t-mT)+m\phi_{off}]} \tag{4.1}$$

where the sum runs to infinity, $\boldsymbol{\varepsilon}$ is the envolope. To get the comb structure in the frequency domain, we apply Fourier transform to $\boldsymbol{E}(t)$:

$$\tilde{\boldsymbol{g}}(\omega) = \int_{-\infty}^{\infty} \boldsymbol{g}(t)e^{-i\omega t}dt \tag{4.2}$$

According to convolution theorem: $\mathcal{F}[f \cdot g] = \mathcal{F}[f] * \mathcal{F}[g]$, where $\mathcal{F}$ represents Fourier transform and $*$ indicates convolution. Thus, the frequency domain is:

$$\tilde{\boldsymbol{E}} = \sum_{m} \mathcal{F}[\boldsymbol{\varepsilon}(t - mT)] * \mathcal{F}[e^{i[w_c(t-mT)+m\phi_{off}]}] \tag{4.3}$$

We then apply the Fourier shift theorem: $\mathcal{F}[g(t - \tau)] = exp(-i\omega\tau)\mathcal{F}[g(t)]$, we have:

$$\tilde{\boldsymbol{E}} = \sum_{m}[e^{-im\omega T}\tilde{\varepsilon}(\omega)] * [e^{-im(w_cT-\phi_{off})}\delta(\omega - \omega_c)] = \tilde{\varepsilon}(\omega - \omega_c)\sum_{m} e^{im(\omega T-\phi_{off})} \tag{4.4}$$

A Dirac comb can be expressed as:

$$\text{Ш}_{\omega_{rep}}(\omega) \equiv \sum_{k=-\infty}^{\infty} \delta(\omega - k\omega_{rep}) = \frac{1}{\omega_{rep}} \sum_{m=-\infty}^{\infty} e^{im\omega T} \tag{4.5}$$

$$\omega_{rep}\text{Ш}_{\omega_{rep}}(\omega - \omega_{off}) = \sum_{m=-\infty}^{\infty} e^{im(\omega-\omega_{off})T)} \tag{4.6}$$

where $\omega_{off} \equiv \phi_{off}/T$. Thus, the Fourier transform of the electric field can be written as

$$\tilde{\boldsymbol{E}}(\omega) \equiv \omega_{rep}\tilde{\boldsymbol{\varepsilon}}(\omega - \omega_c)\text{Ш}_{\omega_{rep}}(\omega - \omega_{off}) \tag{4.7}$$

Alternatively this may be expressed with non-angular frequencies (refer to the appropriate Fourier Transform) as

$$\tilde{\boldsymbol{E}}(f) = f_{rep}\tilde{\boldsymbol{\varepsilon}}(f - f_c)\text{Ш}_{f_{rep}}(f - f_{off}) \tag{4.8}$$

In the time domain, the electric field now can be written as:

$$\boldsymbol{E}(t) = f_{rep}\sum_{k=0}^{\infty}\tilde{\varepsilon}(kf_{rep} + f_{off} - fc)e^{2\pi i(kf_{rep}+f_{off})t} \tag{4.9}$$

The per-roundtrip CEP difference can now be written as:

$$\phi_{off} = 2\pi f_{off}/f_{rep} \tag{4.10}$$

Eq. 3.9 indicates that a frequency comb is composed of numerous different CW frequency lines. It is automatically guaranteed that these CW frequency components are *phase coherent*, since they are only determined by two parameters-f_{rep} and f_{off}. This feature makes frequency combs fundamentally different from filtered thermal light from Fabry-Perot cavities. Because thermal light has a random temporal envelope and carrier phase in each repetition period, there is no phase coherence between its frequency components or temporal periodicity.

There are a few methods for optical frequency comb generation. An easy approach to the formation of an optical frequency comb employs a few cascaded electro-optical

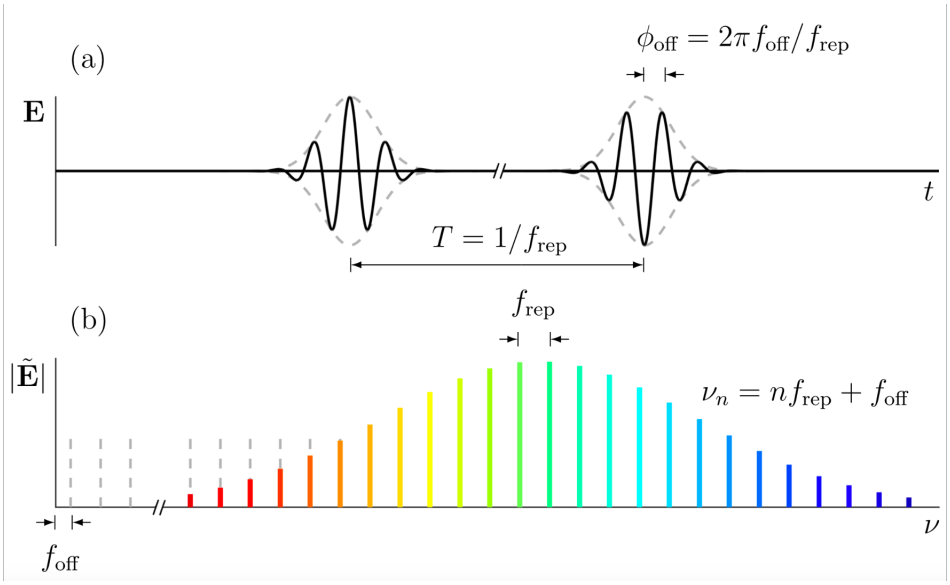

Figure 4.1: (a) In the time domain, a frequency comb is defined by an infinitely long train of identical but arbitrarily-shaped envelopes with period $T = 1/f_{rep}$. Each successive carrier wave slips by a phase of $\phi_{off} = 2f_{off}/f_{rep}$ with respect to its envelope. (b) The Fourier transform of (a) reveals comb structure with an FSR of f_{rep} offset from the origin by frequency f_{off}. The optical frequency of each comb tooth is given by $_n = nf_{rep} + f_{off}$ where n is an integer.

(EO) modulators driven by a microwave signal to impose a series of sidebands on a continuous-wave laser. Due to the recent advances in integrated lithium niobate waveguides, the EO comb uses off-the-shelf components from the telecommunication industry and has great reliability.

Another approach to optical frequency combs generation has attracted great interest due to its advantages of a small footprint, low power consumption, and integration capability. It offers the possibility of miniature comb systems integrated on a semiconductor chip. They are often called microcombs which rely on the Kerr nonlinearity that is enhanced by the optical power build-up in high-Q microresonators or ring-like resonators. Benefiting from modern fabrication techniques, the ultra-low propagation loss inside the microresonators results in the quality (Q) factors ranging from 10^6 up to nearly 10^{11}.

4.2 Laser System

A custom laser system (MenloSystems) outputs two femtosecond pulse trains at different wavelengths: one is centered at 1560 nm (400 mW) and the other is centered at 1040 nm (740 mW). The two pulse trains are pumped by the same oscillator, which is generated from an Er-doped fiber ring. The fiber system is stabilized such that the optical pulses are *phase coherent*. The output of oscillator splits into two doped fibers, where lights go through different optical power amplification processes. The 1040-nm and 1560-nm frequency combs share the same repetition rate of 250.583 MHz.

To get the 1560 nm frequency comb, one of the fibers goes through an Er-doped fiber amplifier (EDFA). After EDFA, a dispersion compensation module eliminates the dispersion introduced by the Er-doped fiber. In general, the gain is available only at a wavelength longer than the pump wavelength. There are two excited states (Excited

state 1 at 1480 nm absorption and Excited state 2 at 980 nm absorption) and one ground state involved in the optical amplification process. The stimulated emission from 1530-1560 nm happens with the population inversion between the ground state and Excited state The population inversion can be achieved by pumping at 980 nm or at 1480 nm. The Er ions pumped by 1480 nm light can directly participate in the emission process. The Er ions at Excited state 2 pumped by 980 nm relax to Excited state 1 through heat radiation, which has a short lifetime. Typically, 980 nm pumping is more desirable because: 1. The separation between output wavelength and pumping wavelength is larger. 2. The absorption linewidth is narrower than the absorption linewidth at 1480 nm. 3. It cannot stimulate back transition to the ground state. To

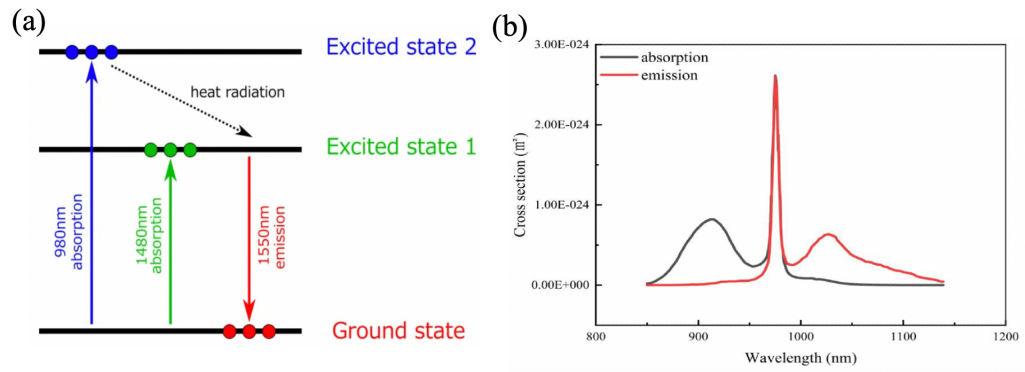

Figure 4.2: (a) The energy diagram of Erbium. adapted from Ref. [8] (b) The absorption and emission spectra of Yb. adapted from Ref. [9]

get the 1040 nm frequency comb, the other part of the oscillator beam goes into a fiber stretcher, where the temporal profile of femtosecond pulses is stretched. It then goes into a Yb-doped fiber amplifier (YDFA). After that a TOD compresser is used to compress the time duration of femtosecond pulses. The gain recovery time (10 us to 1 ms) of doped fibers is long enough for the fiber to "see" the femtosecond pulse trains as a continuous light power. This means its threshold is directly related to the peak pulse energy. Even though the average power is low, ultrashort optical pulses

have high peak intensity, which can damage the doped fiber easily. Therefore, the stretching-compressing technique is widely used in optical power amplification to avoid damaging the doped fibers and also get a larger power amplification.

As shown in the absorption and emission spectra in Fig. 4.2 (b), Yb ions have a strong absorption peak at 980 nm. Optical gain can achieved with the emission peak at 1040 nm. In the Menlos laser system, the YDFA and EDFA are pumped by the replica of the same oscillator. The optical amplification module benefits from the fact that Er and Yb have overlapping absorption wavelength regions, which are roughly from 900 nm – 980 nm. The outputs of two amplifications both have a pulse duration of $\sim$ 70 fs.

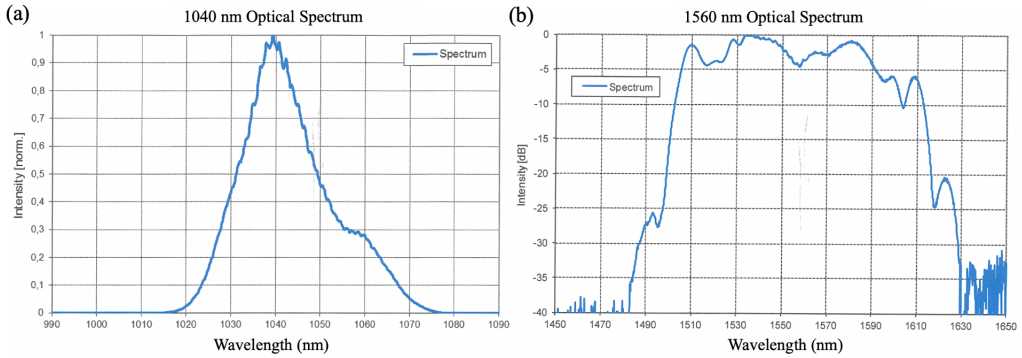

Figure 4.3: (a) the spectrum of the optical frequency comb center at 1040 nm. (b) the spectrum of the optical frequency comb center at 1560 nm.

The spectra of the two output frequency combs are shown in Fig. 4.3 (a) and Fig. 4.3 (b). The 1040 nm frequency comb has an FWHM of $\sim$18 nm, and the 1560 nm frequency comb has an FWHM of $\sim$80 nm. The two pulse trains are 1.7 ns apart in time out of laser heads. The two frequency combs share the same repetition rate and offset frequency. The offset frequency is one of the determining factors of the SNR of 2+3 QuIC current. It needs to be precisely measured, stabilized, and controlled. The importance of measuring the absolute offset frequency will be further discussed later

in the thesis.

4.3 2+3 QuIC Theory

To show why it is necessary to use OFCs for the 2+3 QuIC current generation, we need to start with an introduction to 2+3 QuIC.

4.3.1 Carrier Injection in 2+3 QuIC

The optical injection of carriers in 2PA, 3PA, and 2+3 QuIC can be expressed by the electric fields and the tensor ξ. The number of carriers injected by the two-photon absorption is:

$$\frac{d}{dt}\langle n\rangle_2 = \xi_2^{abcd}(3\omega)E^a_{-3\omega/2}E^b_{-3\omega/2}E^c_{-3\omega/2}E^d_{-3\omega/2} \tag{4.11}$$

The number of carriers injected by the three-photon absorption is:

$$\frac{d}{dt}\langle n\rangle_3 = \xi_3^{abcdef}(3\omega)E^a_{-\omega}E^b_{-\omega}E^c_{-\omega}E^d_{\omega}E^e_{\omega}E^f_{\omega} \tag{4.12}$$

The number of carriers injected by 2+3 QuIC is:

$$\frac{d}{dt}\langle n\rangle_{2+3} = \xi_{2+3}^{abcde}(3\omega)E^a_{-\omega}E^b_{-\omega}E^c_{-\omega}E^d_{3\omega/2}E^e_{3\omega/2} + c.c. \tag{4.13}$$

where,

$$\xi_2^{abde}(3\omega) = 2\pi\int\frac{d\boldsymbol{k}}{(2\pi)^D}\sum_{cv}R^{ab*}_{cv\boldsymbol{k}}R^{de}_{cv\boldsymbol{k}}\delta(3\omega-\omega_{cv}) \tag{4.14}$$

$$\xi_3^{abdefg}(3\omega) = 2\pi \int \frac{d\boldsymbol{k}}{(2\pi)^D} \sum_{cv} R_{cv\boldsymbol{k}}^{abd*} R_{cv\boldsymbol{k}}^{efg} \delta(3\omega - \omega_{cv}) \tag{4.15}$$

$$\xi_{2+3}^{abdef} = 2\pi \int \frac{d\boldsymbol{k}}{(2\pi)^D} \sum_{cv} R_{cv\boldsymbol{k}}^{abd*} R_{cv\boldsymbol{k}}^{ef} \delta(3\omega - \omega_{cv}) \tag{4.16}$$

4.3.2 Current Injection in 2+3 QuIC

The injection rate coefficients of the interference of two- and three-photon processes can be written as:

$$\mu_{2+3}^{abd,fg}(\Omega) = 2\pi \int \frac{d\boldsymbol{k}}{(2\pi)^D} \sum_{cvc'v'} (M_{cc'\boldsymbol{k}} \delta_{v'v} - M_{vv'\boldsymbol{k}} \delta_{c'c}) \times \delta_{w_{cv\boldsymbol{k}} = w_{c'v'\boldsymbol{k}}} R_{c'v'\boldsymbol{k}}^{(3)abd*} R_{cv\boldsymbol{k}}^{(2)fg} \delta(\Omega - \omega_{cv\boldsymbol{k}}) \tag{4.17}$$

where the second-order coefficient $R_{cv\boldsymbol{k}}^{(2)ab}(\frac{3\omega}{2}, \frac{3\omega}{2})$ is:

$$R_{cv}^{(2)ab}(\boldsymbol{k}; \frac{3\omega}{2}, \frac{3\omega}{2}) = \frac{-4e^2}{9\hbar^2\omega^2} \sum_m \frac{v_{cm\boldsymbol{k}}^a v_{cm\boldsymbol{k}}^b}{(\frac{3\omega}{2} - \omega_{mv\boldsymbol{k}})} \tag{4.18}$$

and the third-order coefficient $R_{cv\boldsymbol{k}}^{(3)abd}(\omega, \omega, \omega)$ is:

$$R_{cv}^{(3)abd}(\boldsymbol{k}; \omega, \omega, \omega) = \frac{ie^3}{\hbar^3\omega^3} \sum_{mn} \frac{v_{cm\boldsymbol{k}}^a v_{mn\boldsymbol{k}}^b v_{n\nu\boldsymbol{k}}^d}{(\omega - \omega_{cmk})(\omega - \omega_{nv\boldsymbol{k}})} \tag{4.19}$$

The intraband transitions are the dominant contributions to $R_{cv\boldsymbol{k}}^{(2)ab}$, while $R_{cv\boldsymbol{k}}^{(3)abd}$ also has contributions from interband velocity matrix elements. Note that the intraband velocity matrix elements are associated with the corresponding band dispersion: $v_{nn\boldsymbol{k}}^a = \partial_{\boldsymbol{k}}^a \omega_{n\boldsymbol{k}}$ The broken inversion symmetry of carrier distribution in the k-space is caused by the change of sign of the factor $R_{c'v'\boldsymbol{k}}^{(3)abd*} R_{cv\boldsymbol{k}}^{(2)fg}$ under transformation $\boldsymbol{k} \to -\boldsymbol{k}$.

The current injection rate of 2+3 QuIC can be rewritten as:

$$\frac{d}{dt}\left\langle J^a\right\rangle_{2+3} = \eta_{2+3}^{abdefg}(3\omega)E_\omega^{b*}E_\omega^{d*}E_\omega^{e*}E_{3\omega/2}^{f}E_{3\omega/2}^{g} + c.c. \tag{4.20}$$

where $\hbar\Omega = 3\hbar\omega$ is the total photon energy. The current injection coefficient η_{2+3}^{abdefg} is defined as:

$$\eta_{2+3}^{abdefg}(3\omega,\boldsymbol{k}) = 2\pi e[v_{cc}^a(\boldsymbol{k}) - v_{vv}^a(\boldsymbol{k})]R_{cv\boldsymbol{k}}^{(3)bde}(\boldsymbol{k};\omega,\omega,\omega)^* \times R_{cv}^{(2)fg}(\boldsymbol{k};\frac{3\omega}{2},\frac{3\omega}{2})\delta[3\omega - \omega_{cv}(\boldsymbol{k})] \tag{4.21}$$

where $\omega_{cv}^{ab}(\boldsymbol{k})$ is the symmetrized two-photon amplitude

$$w_{cv}^{ab}(\boldsymbol{k}) \equiv \frac{1}{2}\sum_m \frac{v_{cm}^a(\boldsymbol{k})v_{mv}^b(\boldsymbol{k}) + v_{cm}^b(\boldsymbol{k})v_{mv}^a(\boldsymbol{k})}{\omega_m(\boldsymbol{k}) - \overline{\omega}_{cv}(\boldsymbol{k})} \tag{4.22}$$

The 2+3 QuIC current is generated from $< 001 >$ oriented AlGaAs and behaves like a planar current. Since the electric fields only have x and y components, there are six independent nonzero η_{2+3}^{abcdef} elements:

$$\eta_{2+3}^{xxxxxx} = P(x,y,z) \tag{4.23}$$

$$\eta_{2+3}^{xxxyy} = P(x,y,z) \tag{4.24}$$

$$\eta_{2+3}^{xxyyxx} = \eta_{2+3}^{xyxyxx} = \eta_{2+3}^{xyyxxx} = P(x,y,z) \tag{4.25}$$

$$\eta_{2+3}^{xxxyxy} = \eta_{2+3}^{xxxyyx} = \eta_{2+3}^{xxyxxy} = \eta_{2+3}^{xxyxyx} = \eta_{2+3}^{xyxxxy} = \eta_{2+3}^{xyxxyx} = P(x,y,z) \tag{4.26}$$

$$\eta_{2+3}^{yxxxxy} = \eta_{2+3}^{yxxxyx} = P(x,y,z) \tag{4.27}$$

$$\eta_{2+3}^{yxxyxx} = \eta_{2+3}^{yxyxxx} = \eta_{2+3}^{yyxxxx} = P(x,y,z) \tag{4.28}$$

4.3.3 The Localization of Carrier Distribution

We compare the injection rates of 1+2 QuIC and 2+3 QuIC. They are both functions of $\boldsymbol{k}$, representing distributions of carrier injection in the $\boldsymbol{k}$-space. $\eta_{2+3}^{abdefg}(3\omega,\boldsymbol{k})$ has higher orders of $v(\boldsymbol{k})$, which is related to the energy band dispersion. We assume all the upscripts of $\eta_{2+3}^{abdefg}(3\omega,\boldsymbol{k})$ and $\eta_{1+2}^{abcd}(\omega,\boldsymbol{k})$ are x, which corresponds to the case where the electric fields are polarized along $\langle 100\rangle$ crystal axis. We denote the angle between $\boldsymbol{k}$ and $\langle 100\rangle$ by θ. $\eta_{1+2}^{abcd}(\omega,\boldsymbol{k})$ is a function of $cos^4(\theta)$, whereas $\eta_{2+3}^{abdefg}(3\omega,\boldsymbol{k})$ is a function of $cos^6(\theta)$. This is the origin of the localization of 2+3 carrier injection rate in the $\boldsymbol{k}$-space. It has been theoretically studied by Mahon, Perry T. et al. [10]. Fig. 4.4 shows the calculation of carrier injection rate distribution for 1+2 QuIC and 2+3 QuIC in the $\boldsymbol{k}$-space.

$$\eta_{1+2}^{abcd}(\omega,\boldsymbol{k}) = \frac{i\pi e^4}{2\hbar^3\omega^3}\sum_{cv} v_{cc}^a(\boldsymbol{k})[\sum_m \frac{v_{cm}^b(\boldsymbol{k})v_{mv}^c(\boldsymbol{k}) + v_{cm}^c(\boldsymbol{k})v_{mv}^b(\boldsymbol{k})}{\omega_m(\boldsymbol{k}) - \overline{\omega}_{cv}(\boldsymbol{k})}]^* v_{cv}^d(\boldsymbol{k})\delta[\omega_{cv}(\boldsymbol{k}) - 2\omega] \tag{4.29}$$

$$\begin{aligned}\eta_{2+3}^{abdefg}(3\omega,\boldsymbol{k}) = 2\pi e[v_{cc}^a(\boldsymbol{k}) - v_{vv}^a(\boldsymbol{k})][\frac{ie^3}{\hbar^3\omega^3}\sum_{mn}\frac{v_{cm}^b(\boldsymbol{k})v_{mn}^d(\boldsymbol{k})v_{n\nu}^e(\boldsymbol{k})}{(\omega-\omega_{cmk})(\omega-\omega_{nv\boldsymbol{k}})}]^* \times \\ [\frac{-4e^2}{9\hbar^2\omega^2}\sum_m \frac{v_{cm}^f(\boldsymbol{k})v_{cm}^g(\boldsymbol{k})}{(\frac{3\omega}{2}-\omega_{mv\boldsymbol{k}})}]\delta[3\omega - \omega_{cv}(\boldsymbol{k})]\end{aligned} \tag{4.30}$$

$$\eta_{2+3}^{abdefg}(3\omega,\boldsymbol{k}) = 2\pi\int\frac{d\boldsymbol{k}}{(2\pi)^3}\sum_{cv}\frac{i4e^5}{9\hbar^5\omega^5}[\sum_{mn}\frac{\boldsymbol{v}_{cm\boldsymbol{k}}^b\boldsymbol{v}_{mn\boldsymbol{k}}^d\boldsymbol{v}_{nv\boldsymbol{k}}^e}{(\omega-\omega_{cm\boldsymbol{k}})(\omega-\omega_{nv\boldsymbol{k}})}]^* \times [\sum_m\frac{\boldsymbol{v}_{cm\boldsymbol{k}}^f\boldsymbol{v}_{mv\boldsymbol{k}}^g}{(\frac{3\omega}{2}-\omega_{mv\boldsymbol{k}})}] \delta[\omega_{cv}(\boldsymbol{k}) - 3\omega] \tag{4.31}$$

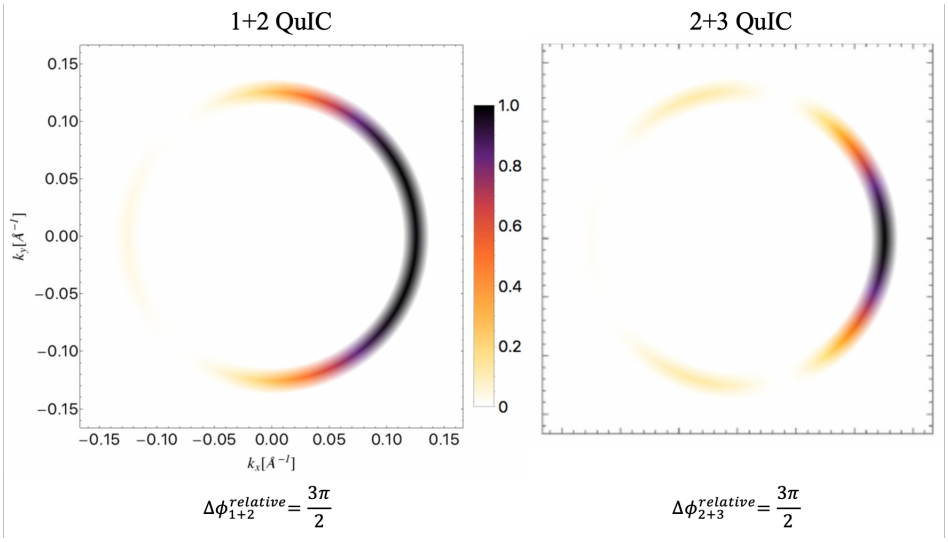

Figure 4.4: Left: the calculated injection rate of 1+2 QuIC carriers in the $\boldsymbol{k}$-space when the relative phase of two frequencies is $\frac{\pi}{2}$. The fields of frequency ω and 2ω are polarized along $\boldsymbol{k}_x$. Right:the calculated injection rate of 2+3 QuIC carriers in the $\boldsymbol{k}$-space when the relative phase of two frequencies is $\frac{\pi}{2}$. The fields of frequency ω and $\frac{3\omega}{2}$ are polarized along $\boldsymbol{k}_x$. adapted from Ref. [10]

4.3.4 2+3 QuIC Current Generated with Frequency Combs

In order to describe the 2+3 QuIC signal, we need to first understand the spectrum of the second harmonic generation of a frequency comb. It can be considered as the sum frequency process of each frequency comb tooth and all the other comb teeth, as shown in Fig. 4.5. We denote the lower and upper bounds of the spectrum in units of repetition rate by N_a and N_b, respectively. The square of the electric field spans from $2N_a$ to $2N_b$. The offset frequency is doubled while the repetition rate is the same.

$$\sum_{m=N_a}^{N_b} e^{2\pi i(mf_{rep}+f_{off})t} \sum_{m=N_a}^{N_b} e^{2\pi i(mf_{rep}+f_{off})t} = \sum_{m=2N_a}^{2N_b} e^{2\pi i(mf_{rep}+2f_{off})t} \tag{4.32}$$

According to the spectra of 1040 nm OFC and 1560 nm OFC, there are 39448 comb

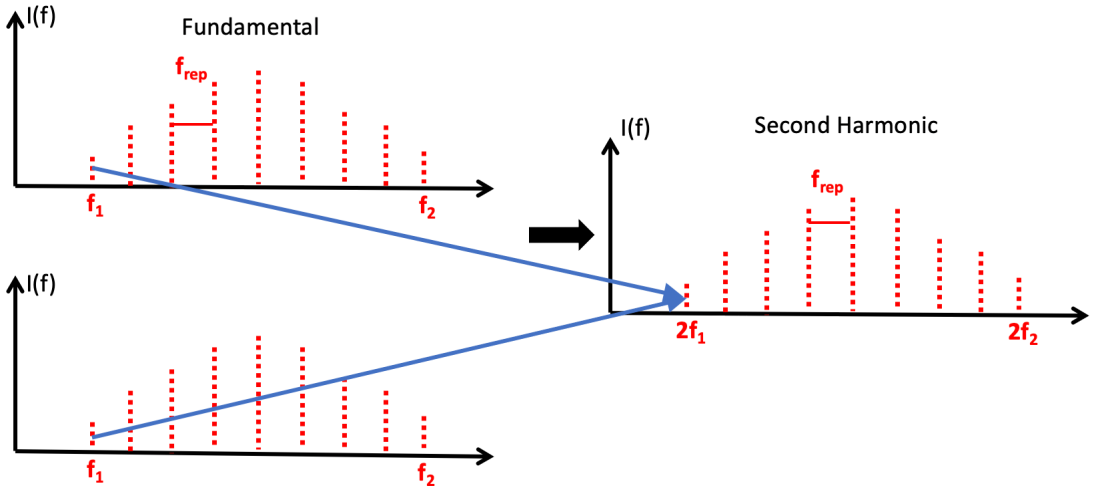

Figure 4.5: A schematic illustration of the comb teeth of fundamental beam and second harmonic on the frequency domain.

teeth in the 1560-nm spectrum and 28556 comb teeth in the 1040-nm spectrum. The square of the 1040-nm electric field and the cube of the 1560-nm electric field have the same central frequency: $2N_{1040nm} = 3N_{1560nm}$, where N_{1040nm} and N_{1560nm} are the central frequency of 1040 nm OFC and 1560 nm OFC in units of repetition rate, respectively. We assume the two OFCs are linearly polarized along the same axis. N_1 and N_2 denote the number of frequency combs teeth in the two OFCs. We assume the two OFCs have the same spectral bandwidth: $N_1 = 3N_2/2$. The electric field part of QuIC expression can be written as:

$$E^{2*}_{1040nm}E^{3}_{1560nm} = \sum_{m=2N_{1040nm}-N_1}^{2N_{1040nm}+N_1} e^{-2\pi i(mf_{rep}+2f^{1040}_{off})t} \sum_{n=3N_{1560nm}-3N_2/2}^{3N_{1560nm}+3N_2/2} e^{2\pi i(nf_{rep}+3f^{1560}_{off})t}$$
$$|E_{1560nm}|^3 \left|E^f_{1040nm}\right|^2 = e^{2\pi i\Delta\phi^{relative}_{2+3}} |E_{1560nm}|^3 \left|E^f_{1040nm}\right|^2 \quad (4.33)$$

Therefore, the injection rate of QuIC current can be written as:

$$\frac{d}{dt}\langle J^a\rangle_{2+3} = \sum_{bdefg} \eta_{2+3}^{abcdef} e^{2\pi i \Delta\phi_{2+3}^{relative}} \left|E_{1560nm}^{b}\right| \left|E_{1560nm}^{d}\right| \left|E_{1560nm}^{e}\right| \left|E_{1040nm}^{f}\right| \left|E_{1040nm}^{g}\right| + c.c. \tag{4.34}$$

where $b, c, d, e, f = (x, y, z)$. The relative phase parameter $\Delta\phi_{2+3}^{relative}$ is $(3f_{off}^{1560} - 2f_{off}^{1040})t$, which is a phase ramp with a slope of $3f_{off}^{1560} - 2f_{off}^{1040}$. This means that the QuIC current is oscillating at the offset frequency of the oscillator.

Fig. 4.6 is a sketch of the 2+3 QuIC current induced by a ω OFC and a $3\omega/2$ OFC with the same offset frequency and repetition rate. The two pulse trains are temporally overlapped, and $\chi^{(3)}$ comes into play. QuIC currents appear as "bursts" at the cooccurrences of 1040 nm pulses and 1560 nm pulses. The rise of bursts is limited by the temporal profile of the pulses, which is on the femtosecond time scale. The long "tail" is related to the current relaxation process, which is a few hundred ps for GaAs. Between adjacent pulses, there is a phase shift of $2\pi f_{off}/f_{rep}$ on the relative phase parameter $\Delta\phi$, which results in the amplitude modulation of QuIC current. A Lock-in amplifier is a tool capable of picking up signals at a specific frequency. In this case, the Lock-in detector detects at the amplitude modulation frequency. The signal is the integral of the current bursts, which is proportional to the injection rate of the QuIC current.

The two determining factors of OFCs - f_{rep} and f_{off} - are both useful to the measurement of 2+3 QuIC. The offset frequency serves as the detection frequency of 2+3 QuIC. It has been mentioned that the 1040-nm OFC and 1560-nm OFC of the Menlo Systems laser share the same repetition rate and offset frequency. Here, we show that having the same repetition rate is beneficial to reducing the noise of 2+3 QuIC. Firstly, the same repetition rate indicates the same pulse interval for the two OFCs,

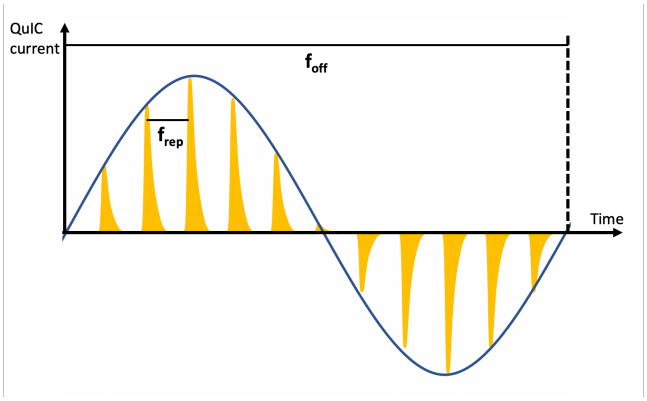

Figure 4.6: A schematic illustration of the current injected by 2+3 QuIC on the time domain. The fields of photon frequency ω and $\frac{3\omega}{2}$ share the same repetition rate and offset frequency, denoted by f_{rep} and f_{off}, respectively.

which guarantees a good temporal overlap over the whole pulse train. Secondly, the relative phase parameter can be expressed as:

$$\Delta\phi = [-m(2f_{rep}^{1040} + 2\delta f_{rep}^{1040}) + m(3f_{rep}^{1560} + 3\delta f_{rep}^{1560}) - 2(f_{off}^{1040} + \delta f_{off}^{1040}) \\ +3(f_{off}^{1560} + \delta f_{off}^{1560})]t \tag{4.35}$$

If the two OFCs share the same repetition rate, we will have $3\delta f_{rep}^{1560} - 2\delta f_{rep}^{1040} = 0$. However, if the two repetition rates are locked separately, $3\delta f_{rep}^{1560} - 2\delta f_{rep}^{1040}$ will be nonzero and magnified by the number of comb teeth m, which is on the order of 10^6.

4.4 Offset Frequency

4.4.1 2f-3f Self-referencing Technique

The conventional way of measuring the offset frequency of an OFC is to optically beat it against itself. However, this method is only effective when the spectrum of the OFC is octave-spanning, which is not the case for our lasers. Although the spectrum of laser can be expanded by creating supercontinuum, we used a 2f-3f self-reference setup to

measure the offset frequency for the following reasons: 1. The supercontinuum method is not efficient in terms of optical power. Most of the power on the spectrum is "dead" power since it does not contribute to the beat note. The 2f-3f self-reference technique doesn't require an octave-spanning spectrum. All of the power of the harmonics contributes to the beat note signal. 2. More importantly, the 2f-3f self-reference process is very similar to 2+3 QuIC in terms of the relative-phase dependence. Later we will show that for some technical reasons, it is actually better to set different offset frequencies for the two OFCs, where the beat note of 2f-3f self-reference is even more informational.

In this experiment, we have two 2f-3f self-referencing setups. The first setup is to measure the offset frequency of the optical oscillator. The offset frequency is detected as the beat note of the frequency comb teeth of the third harmonic of 1550 nm light and the second harmonic of 1040 nm light. The electrical signal from the Si-based photodetector is sent to two modules to produce signals for offset frequency control and stabilization: One is a feedback loop, and the other is a feed-forward loop designed to compensate for the low-frequency noise and high-frequency noise, respectively. The feedback loop loosely locks the offset frequency within a narrow frequency range. It is composed of a frequency counter that reads out the offset frequency and a LabVIEW program that calculates the voltage needed to compensate for the slow drift. In the fast feed-forward loop, AOMs are used to provide a real-time compensation for noise at fast frequencies ($\sim 80MHz$). The second 2f-3f self-referencing setup is to measure the AOM-stabilized beat note, at which QuIC current should appear.

The two 520 nm beams need to have similar beam diameters and wavefronts to achieve a better quality of the 2f-3f beat note signal. Fig. 4.7 is a picture of the 2f-3f experimental setup. The 1040-nm beam and 1560-nm beam are at different heights outside the laser heads. A periscope is used to adjust the height of the 520 nm beam

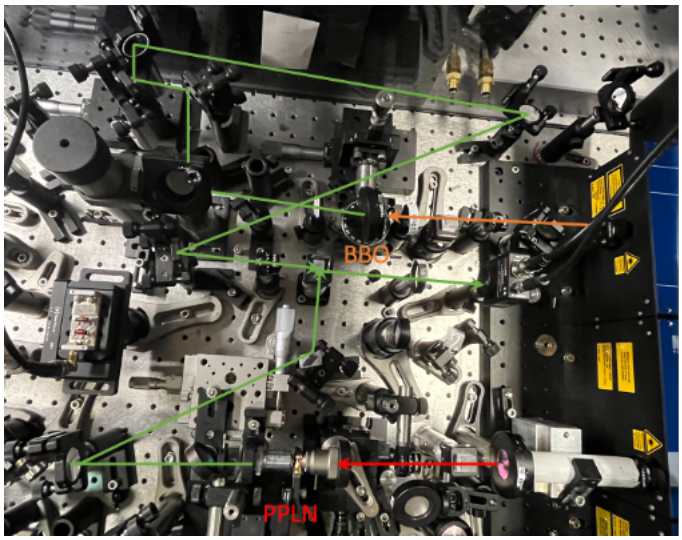

Figure 4.7: A picture of the experimental 2f-3f setup.

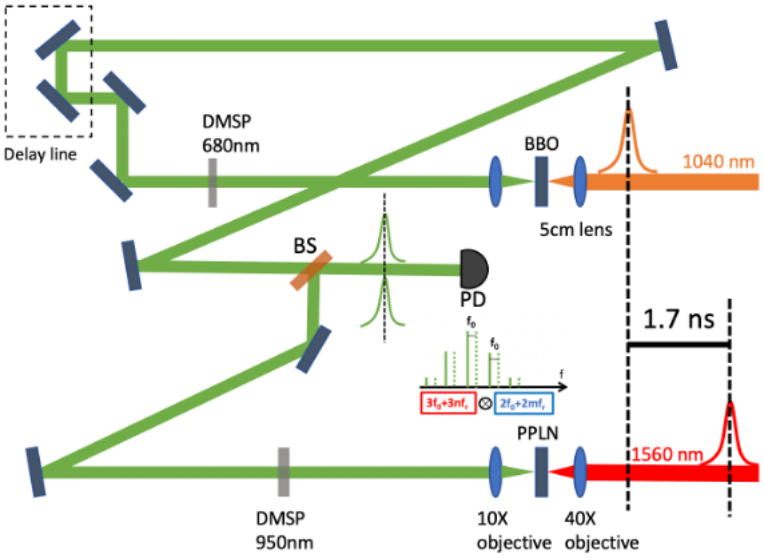

Figure 4.8: A schematic diagram of the first 2f-3f self-referencing interferometer, where the second harmonic of 1040-nm OFC and the third harmonic of 1560-nm OFC are generated and beat against each other to create a beat note at f_{off}.

after the BBO crystal. As mentioned earlier in this thesis, the 1040-nm and 1560-nm lights are 1.7 ns apart in time right out of laser heads. A delay line is used to achieve temporal overlap of the second harmonic of 1040 nm and the third harmonic of 1560 nm. The 1560 nm light is focused by a 40X objective lens (focal length: 6 mm) to a periodically poled lithium niobate (PPLN) crystal. The 1040 nm light is focused by a lens (focal length: 2.5 cm) to a BBO crystal. The second harmonic generation and third harmonic generation coincide inside the PPLN crystal. We use a dichroic short pass filter at 950 nm on the 1560 nm arm and a dichroic short pass filter at 680 nm on the 1040 nm arm to filter out the irrelevant light. A 10X objective lens collimates the fundamental beam and harmonics. The longitudinal and transverse positions of PPLN crystal can affect the efficiency and spectrum of the third harmonic generation. Therefore, the PPLN is mounted to a 3D translational stage. The longitudinal position of the second lens in each telescope system was varied to collimate the 520 nm beam after the nonlinear crystal. Fig. 4.9 depicts the optical spectra of green OFCs on the frequency domain. In each adjacent comb teeth pair, one is generated from the 1040-nm OFC, and the other is generated from the 1560-nm OFC. Thus, the beat note of two green OFCs can be written as:

$$E_{green}^{1040*} E_{green}^{1560} = \sum_{m} e^{2\pi i(3f_o+3mf_r)t} \sum_{n} e^{-2\pi i(2f_o+2nf_r)t} \tag{4.36}$$

where f_r is the repetition rate and f_o is the offset frequency. This expression is identical to the expression of the injection rate of 2+3 QuIC in Eq. 31. If the 1040-nm OFC and 1560-nm OFC have different offset frequencies, then it can be written as:

$$E_{green}^{1040*} E_{green}^{1560} = \sum_{m} e^{2\pi i(3f_{off}^{1560}+3mf_r)t} \sum_{n} e^{-2\pi i(2f_{off}^{1040}+2nf_r)t} \tag{4.37}$$

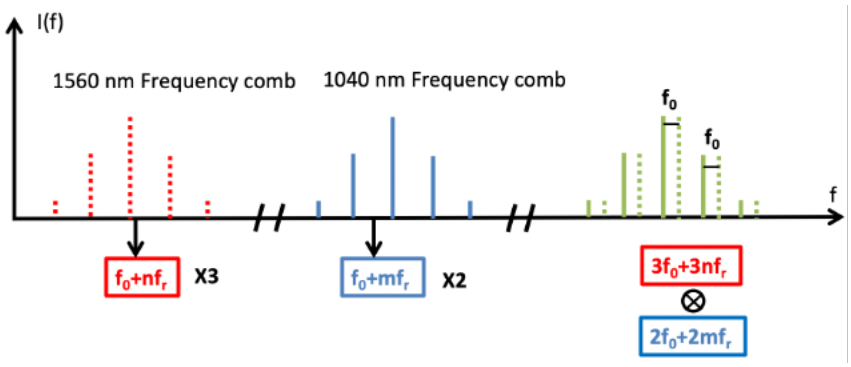

Figure 4.9: A schematic illustration of why the beat note of the green harmonics is the offset frequency.

4.4.2 Harmonic Generation

Quasi-phase matching is a type of phase matching achieved in a nonlinear crystal where the crystal orientation is periodically modulated. It is especially useful for nonlinear processes where multiple beams are involved, such as second harmonic generation and sum frequency generation. In these processes, the efficiency is dependent on how well the product waves are in phase with the fundamental beam along the direction of propagation. The efficiency is determined by the energy transferred from fundamental waves to product waves. In this chapter, we only discuss collinear phase matching. As shown below, the direction of energy transfer changes when there is a large phase mismatch between product waves and fundamental waves. Taking second harmonic generation as an example, we denote E_1 as the electric field of the second harmonic and E_2 as the electric field of the fundamental. E_1 and E_2 can be expressed as plane waves: $\boldsymbol{E}_1 = |E_1| e^{-ik_1 z}$, $\boldsymbol{E}_2 = |E_2| e^{-ik_2 z}$. The relative phase is from: $\boldsymbol{E}_1^* \boldsymbol{E}_1^* \boldsymbol{E}_2 = |E_1|^2 |E_2| e^{i(-k_2+2k_1)z}$. In a homogeneous medium, due to chromatic dispersion, we have $2k_1 \neq k_2$. Therefore, a phase mismatch larger than 180° between the second harmonic and fundamental makes the energy transfer flip direction, which compromises the overall efficiency.

The crystal orientation of Lithium Niobate is flipped by strong electric fields periodically. The period is a multiple of the desired wavelength of operation. The number of generated photons is proportional to the distance waves travel with PPLN. To obtain quasi-phase matching, the crystal orientation flips in areas where the relative phase is more than 180 degrees. The direction of dipoles in the crystal is kept the same throughout propagation, resulting in a consistent energy transfer from pumping light to product lights. Although PPLN we used (MSHG1550-0.5-0.5) is typically used to generate the second harmonic of 1550 nm, the third harmonic generation can also take place given a high spatial intensity. In the spectrum of outcoming light from PPLN, the intensity of 780 nm (SHG) is much stronger than that of 520 nm (THG).

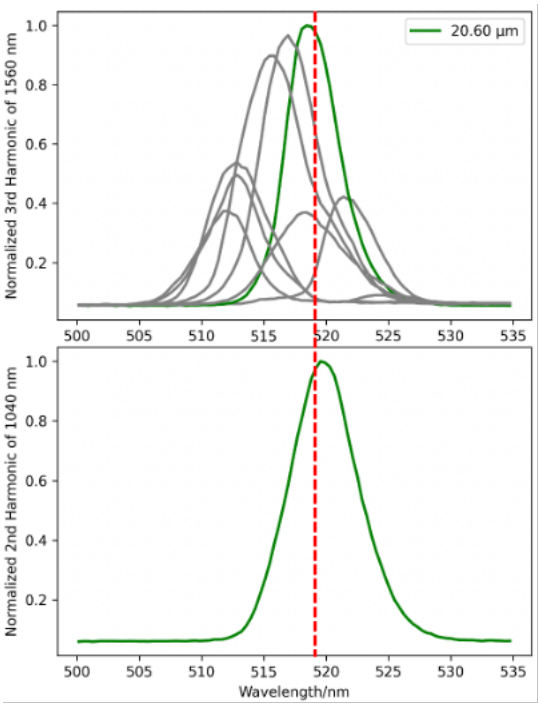

Figure 4.10: Top: the spectra of the third harmonic of the 1560-nm frequency comb generated with different modulation periods of PPLN. Bottom: the spectrum of the second harmonic of the 1040-nm frequency comb.

The power of beat note is highly dependent on the overlap of spectra of the green light from the 1040-nm OFC and the green light from the 1560-nm OFC. The quasi-

phase matching condition can be adjusted by changing the modulation period inside the crystal. There are nine modulation periods ranging from 18.50 - 20.90 um in one PPLN crystal. As shown in Fig. 4.10, the spectrum of the second-harmonic is centered at $\sim$ 519 nm. The center of the third-harmonic spectrum shifts from 512 nm to 521 nm while the modulation period gets larger. The modulation period of 20.60 μm offers the best overlap of the two green-light spectra. In general, the spectra of harmonics will be narrowed if the wavefronts of harmonic and fundamental mismatch inside the crystal. Therefore, we generally need the Rayleigh length to be longer than the thickness of crystals. The Rayleigh length of the focused beam should be comparable to the thickness of nonlinear crystals. The beam diameter of 1040-nm light before the objective lens is $\sim$ 1.62 mm. The Raylength is $\sim$ 530 μm, which is longer than the thickness of BBO (100 μm). From the spectrum at the bottom of Fig. 4.10, we can tell that the second-harmonic spectrum is not limited much. On the other hand, the beam diameter of the 1560-nm light before the 40X objective is $\sim 2.17mm$. The Raylength of 1560-nm light around the focal spot is $\sim 30.4\mu m$, much shorter than the thickness of PPLN (0.5 mm). This explains the narrowing of the third-harmonic spectrum.

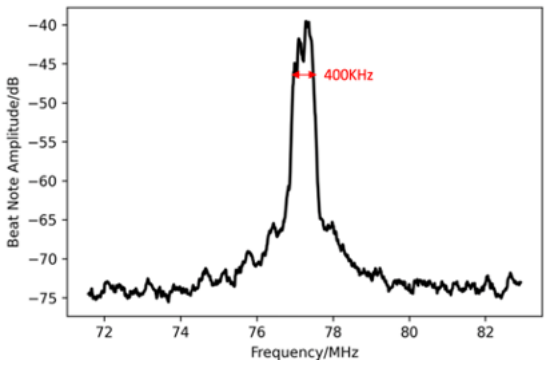

Figure 4.11: The offset frequency of the optical oscillator measured by 2f-3f self-referencing interferometer. The bandwidth (red double arrow) of the offset frequency is $\sim 400KHz$.

The power of the green light from THG is $\sim 5\,mW$, and the power of the green light from SHG is $\sim 10\,mW$. Since the detection area of our photodetector is fairly small compared to the 520 nm beam diameters, we focused both green lights with a lens in front of the photodetector to improve the absolute electrical power of the beat note. A beat-note signal-to-noise ratio of $\sim 25\,dB$ was achieved, as shown in Fig. 4.11.

4.4.3 Feed-forward Loop

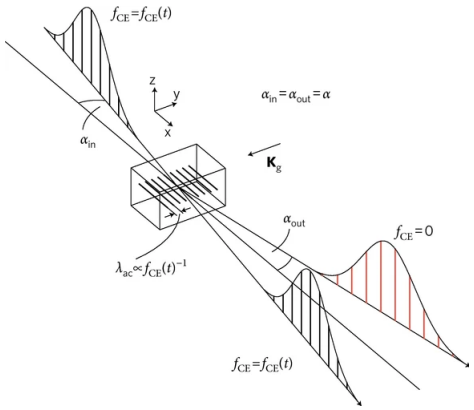

Figure 4.12: Concept of the direct feed-forward method for stabilization of CEP. For maximum diffraction efficiency into first order (red comb modes), the Bragg condition $2\lambda_{ac}sin(\alpha) = \lambda n$ has to be fulfilled. $\alpha = \alpha_{in} = \alpha_{out}$ is the Bragg angle, λ_{ac} the acoustic wavelength, λ the optical wavelength, and n the refractive index. adapted from Ref. [11]

We adapted the concept of feed-forward carrier-envelope phase (CEO) stabilization from Ref. [11]. CEP stabilization can be enabled by establishing a phase-locked loop between f_{CE} and a reference oscillator. The conventional servo control of the CEP has some drawbacks: 1. It can affect other laser parameters such as output power, pulse duration, or round-trip time. 2. It requires a careful balance between short-term phase jitter and stability against drop-outs. A feed-forward loop can avoid these drawbacks by feeding the independently measured and amplified carrier-envelope frequency into the AOM. As shown in Fig. 4.12, the jitter of the CEP of the incoming beam is

compensated in the first-order diffraction. Zero-offset frequency combs that have the same electric field structure in all the temporal pulse envelopes have been achieved in a feed-forward fashion.

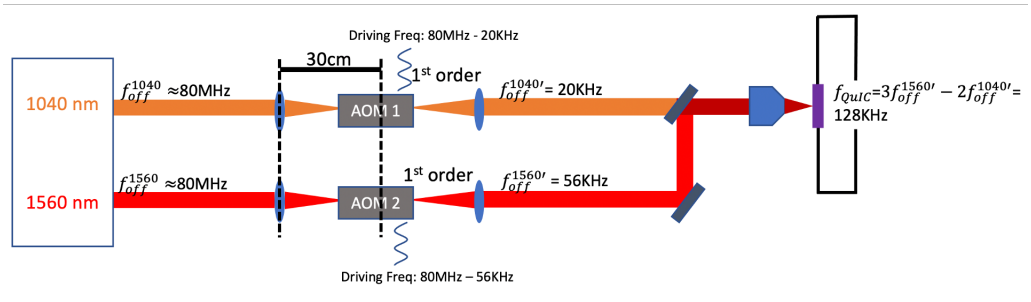

Figure 4.13: A schematic diagram of the optical part of the feed-forward loop. The post-AOM offset frequencies of the 1040-nm OFC and the 1560-nm OFC are 20 KHz and 56 KHz, respectively.

In our case, the carrier-envelope frequency needs to be at specific nonzero frequencies such that the QuIC injected current can be detected on the KHz frequency level. The driving frequency of AOM is then $f_{drive} = f_{oscillator} - f_{1st}$ where $f_{oscillator}$ is the offset frequency of the oscillator and f_{1st} is the offset frequency of 1st-order diffraction. As mentioned before, the optimal operation frequency of ISOMET 1205C-1 AOM is 80 MHz. Thus, the offset frequency of the oscillator needs to be at around 80 MHz. Note that the offset frequency of the 1st-order diffraction of AOMs is referred to as the post-AOM offset frequencies in this thesis. $f_{oscillator}$ and f_{1st} need to be mixed by an electrical frequency mixer to yield f_{drive}. However, from the RF-signal-processing point of view, it is not trivial to get a single sideband when $f_{oscillator}$ and f_{1st} are orders of magnitude apart. The frequency interval between the stop band and the pass band of RF electrical low-pass filters is usually a few MHz. However, the sidebands are only a few hundred KHz apart if we directly mix the post-AOM offset frequency and the operation frequency of AOM. Therefore, we added intermediate frequencies to mix the offset frequency up and then mix it down.

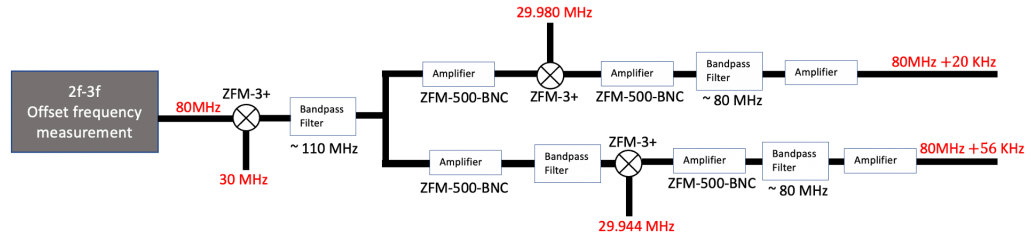

Figure 4.14: The RF-circuit part of the feed-forward loop. The two frequencies on the right are the driving signals of two AOMs.

As shown in Fig. 4.14, the sum of the offset frequency of the oscillator and intermediate frequency (30 MHZ) is picked out at around 110 MHZ with a bandpass filter. The signal is equally split into two channels. In each channel, the signal is amplified and then mixed with another slightly different intermediate frequency. The lower sideband is at ∼80 MHz. As discussed before, if the two OFCs illuminating the crystal have the same offset frequency, the QuIC injected current will oscillate at that offset frequency as well. However, practically, the frequency mixers cannot perfectly isolate their two inputs from the output. Hence, at the first frequency mixer, there is a leakage of the 30 MHz into the output. The 30 MHz will mix with the other intermediate frequency ($30\,MHz - f_{off}$), creating an extremely weak beat note at the post-AOM offset frequency. It can still be captured by our AlGaAs device because it is much more sensitive to the change of amplitude than the change of optical relative phase. Acting as amplitude modulation, this beat note will give rise to the readings on the Lock-in Amplifier at the QuIC detection frequency. But this is a fake QuIC current signal since the readings will not change with the relative phase of two OFCs. This kind of signal has been observed in [42], which later turned out to be an irrelevant amplitude modulation artifact. The approach to avoid it is to pick a pair of different offset frequencies so that $3f_{off}^{1560} - 2f_{off}^{1040}$ does not overlap with any harmonics of f_{off}^{1560} or f_{off}^{1040}, as shown in Fig. 4.13. The driving signal applied to the AOM for 1040-nm

light is at 80MHz+20KHz, and the driving signal applied to the AOM for 1560-nm light is at 80MHz+56KHz. After the feed-forward loop, the offset frequency of 1040-nm OFC is at 20KHz, and the offset frequency of 1560-nm OFC is at 56KHz, which results in a QuIC current oscillation at 128 KHz. All the intermediate frequencies are generated from the same Direct Digital Synthesizer (DDS) so that the relative phase among them is locked. The reference frequency of the Lock-in Amplifier also needs to be generated from the same DDS because the relative phase of the internal clock of the Lock-in Amplifier and the clock of DDS slowly drifts.

We optimized the diffraction efficiency of the two AOMs by changing their positions in the telescope and adjusting their orientations. The post-AOM optical power of 1040 nm is $\sim$ 90 mW, and the post-AOM optical power of 1560 nm is $\sim$ 80 mW. The driving powers of the AOM on 1040-nm arm and the AOM 1560-nm arm are both $\sim$33 dbm. The electrical signals were checked on an oscilloscope after being applied to the AOMs. On the oscilloscope, the signals are supposed to look like sine waves without too much jittering of the amplitude. The jittering is mainly caused by non-optimal frequency filtering, which can be eliminated by fine-tuning the backend voltage and band-pass filters. Also, the input power of each amplifier must not exceed the maximum input power. Otherwise, there will be significant harmonics of the signal, which can cause artifacts on the Lock-in Amplifier as well. The signals were checked carefully on a Keysight MXA Signal Analyzer to make sure that there was no beat note of harmonics at $3f_{off}^{1560} - 2f_{off}^{1040}$.

The second 2f-3f self-reference setup was placed after where the two post-AOM beams were combined. It was used to measure the new beat note at $3f_{off}^{1560} - 2f_{off}^{1040}$. The two beams passed through a PPLN crystal together, generating green lights at $\sim$520 nm. The green lights were picked out and sent to a photodetector. Fig. 4.15 shows the beat note measured by a spectrum analyzer at $\sim$128 KHz. The feed-forward

technique greatly reduced the bandwidth of the offset frequency of the oscillator from 400 KHz to 1 Hz, which is much more suitable to the Lock-in detection. It also offered tunability to the post-AOM offset frequencies, which is beneficial to separating the QuIC detection frequency from other frequencies. Each beam was blocked to ensure that the interference of two green lights caused the peak.

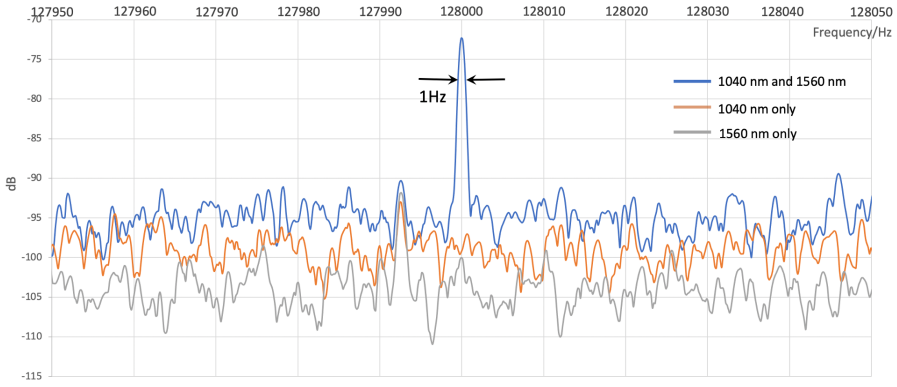

Figure 4.15: The beat note (blue curve) with an FWHM of $\sim$ 1Hz from the second 2f-3f self-referencing interferometer. The frequency spectra when blocking 1560 nm light (orange curve) and 1040 nm light (grey curve).

4.4.4 Feedback Loop

The beat note from the 2f-3f self-referencing setup powers both the slow feedback loop and the fast feed-forward loop. We introduce the mechanism of the feedback loop here. As discussed earlier, the offset frequency of the two OFCs determines the SNR of the QuIC current measurement. The free-running offset frequency of the oscillator usually drifts outside the window after only a few minutes, as shown in Fig. 4.16. The signal from the 2f-3f photodetector has the beat note at not only offset frequency but also the repetition rate of frequency combs and their electrical harmonics. Therefore, the signal needs to pass through a bandpass filter first. As shown in Fig. 4.17, the bandpass window of our bandpass filter is $\sim 4.2\,MHz$. The QUIC signal is due to the change

of optical phase, which is a much weaker effect than the change of optical power. The fluctuation in optical power can easily overwhelm the actual QUIC signal. If the beat note drifts out of the bandpass window, the electrical power of the driving signal of AOMs will significantly decrease. The change in AOM diffraction efficiency will then create a huge noise on the QuIC current. Therefore, a feedback loop is necessary for keeping the beat note inside the pass band.

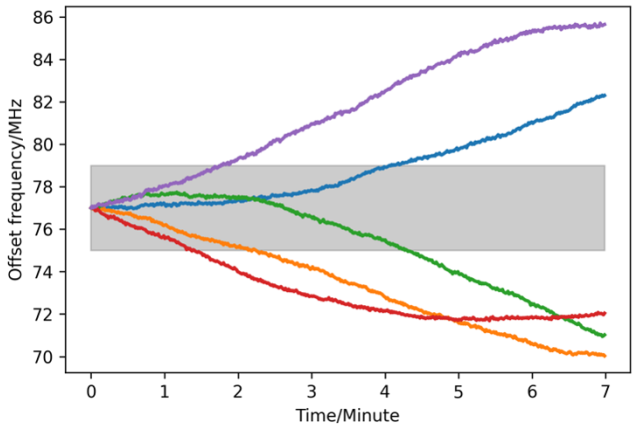

Figure 4.16: 5 runs of free-running oscillator offset frequency measurement. The offset frequency drifts out of ±1.5MHz (the grey region) within a few minutes.

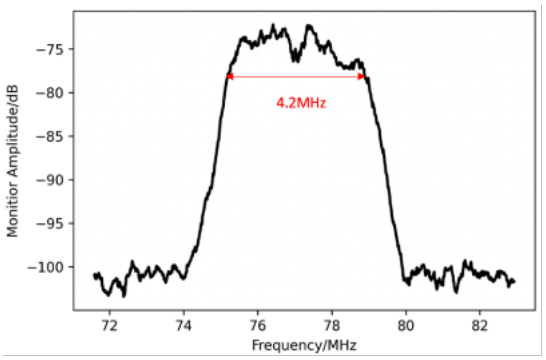

Figure 4.17: The spectrum of the bandpass filter with an FWHM of 4.2 MHz.

Before turning the loop on, we adjusted the pump current and backend voltage to place the offset frequency beat note at the center of the bandpass window ($\sim 77 MHz$),

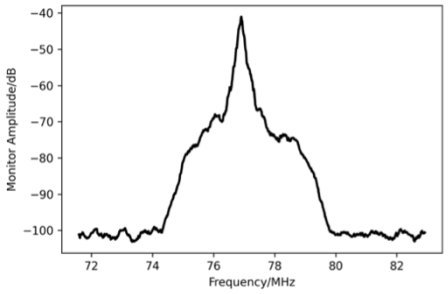

Figure 4.18: The spectrum of the oscillator offset frequency picked out by the bandpass filter.

as shown in Fig. 4.18. The smallest increment of pump current is 0.01 mA, corresponding to a frequency shift of 1.5MHz. So, the pump current adjustment acts as the "coarse control," and the backend voltage offers finer control. The backend voltage not only offers tunability for placing the offset frequency at a flat region of the filter window but also controls the alignment of the beams through the objective before the sample. In the fast-feed forward loop, two AOMs are compensating for the noise of the offset frequency of the oscillator. The first-order diffractions of the two AOMs are sent to the 60× objective lens before the sample. Due to chromatic aberration, the two colors are focused by the objective lens at different locations longitudinally. The focal length is given by:

$$\frac{1}{f(\lambda)} = (n(\lambda) - 1)(\frac{1}{R_1} - \frac{1}{R_2}) \tag{4.38}$$

where R_1 and R_1 are the radius of the front and back spherical surfaces respectively. The 1560 nm light is focused further than the 1040 nm light. As shown in Fig. 4.19, the separation of the focal spots is around $41\mu m$.

The slow feedback loop is critical to the spatial stability of the beams at the sample. Here, we show how the slow drift of offset frequency can cause a drift of beam

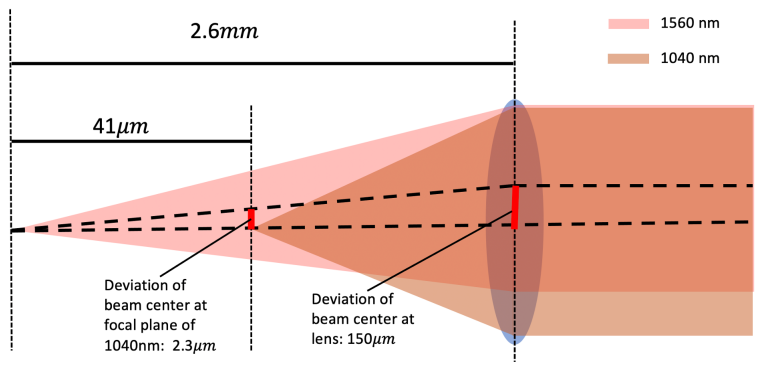

Figure 4.19: A schematic illustration of the beam geometry when the driving frequency of the 1560-nm beam has a slow drift.

focal spots on the sample. Inside AOM, the wavevector of light gets diffracted by bulk acoustic-optic interaction. Bragg angle θ_B is the particular angle of incidence (between the incident beam and the acoustic wave), which gives efficient diffraction into a single diffracted order. In the longitudinal-mode interaction, the acoustic wave travels longitudinally in the crystal, and the incident and diffracted laser beams see the same refractive index. The angle between the 0th order and the 1st order is denoted by seperation angle $\theta = 2\theta_B$, where $\theta_B = \frac{\lambda F}{2\nu}$. The refractive index of $PbMoO_4$ is $\sim$2.4. The modulaiton frequency of AOM is $\sim$80 MHz. Therefore, the separation angle between the 1560-nm fundamental and its 1st order is about 0.01°. Now we assume the offset frequency of the 1560-nm OFC "wanders" freely inside the bandpass window. The change of diffraction angle is $\sim$ 0.0005°. Therefore, the slow drift inside the bandpass window can cause a deviation of beam center of 150μm at 60$\times$ objective lens. Due to this deviation, some of the light will be clipped by the lens aperture. Moreover, the center of the beam after the objective lens will be affected as well. At the focal plane of 1040 nm light, the deviation of the beam center of 1560 nm light is approximately 2.3μm. The QuIC current is practically a planar current that peaks when the orientation of GaAs crystal is <001>. The two beams need to propagate

along the axis of the objective lens to ensure normal incidence. Given that the spacing between electrode pairs is only 7 μm, such a beam spot drift will be detrimental to the observation of QuIC current.

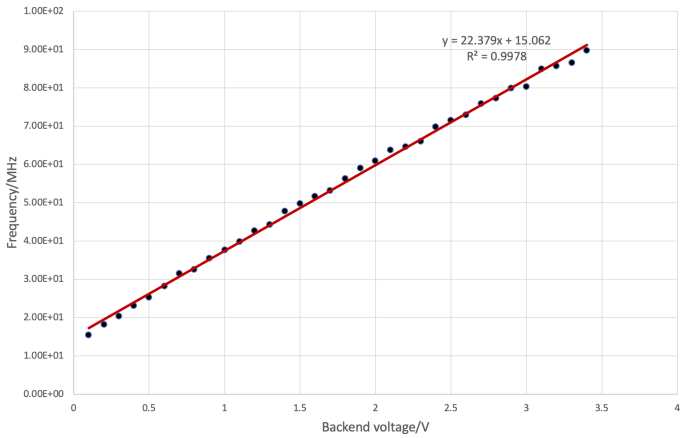

Figure 4.20: The oscillator offset frequency as a function of the backend voltage (black dots). A linear equation (red line) fits the measurement with a good number of 0.9978.

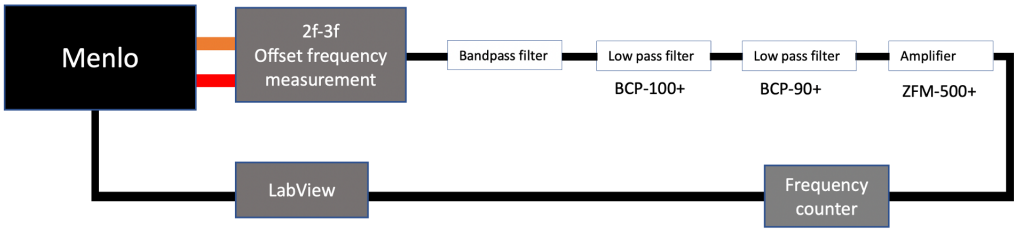

Figure 4.21: A schematic diagram of the feedback loop.

Fig. 4.21 is a schematic of the slow feedback loop. The beat note is picked out by one bandpass filter, one Mini-circuit BCP-100+ low pass filter, and one Mini-circuit BCP-90+ low pass filter. Both low-pass filters provide a > 20 dB loss for the frequency at the repetition rate. The signal then gets amplified by a ZFM-500+ that provides a gain of 20 dB. RF attenuators match the maximum input power of ZFM-500+, which is five dBm. A Hewlett Packard 53132A frequency counter measures the beat note with a sampling rate of 256/s. After adjusting the offset beat note to be at a "sweet spot,".

The LabVIEW program records the initial offset frequency. The average of every 64 data points from the frequency counter is compared with the initial offset frequency. If the beat note drifts out of the margins ($f_{initial} \pm 500KHz$), then the LabVIEW program calculates the voltage needed to compensate for the drift based on the linear dependence of offset frequency on the backend voltage (Fig. 4.20). Fig. 4.22 shows the robustness of the feedback loop. The offset oscillator was manually perturbated by changing the pumping current at times indicated by red arrows. The offset frequency of the oscillator stays stable within a much narrower window than the band-pass filter's bandwidth. As a result, the alignment of beam focal spots at the sample stays stable for hours.

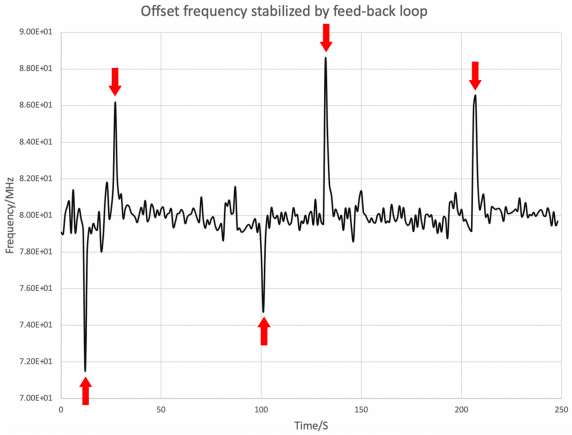

Figure 4.22: The oscillator offset frequency stabilized by the feedback loop. The red arrows denote the times when the offset frequency is manually perturbed.

4.4.5 Two-Color Temporal Overlap

To find the temporal overlap of 1040 nm and 1560 nm lights, we focused both lights to a $10\mu m$ thick BBO with a $40\times$ objective lens and monitored the spectrum of the outgoing light. A 3-axis rotation stage adjusts the orientation of BBO. It needs to be adjusted such that the second harmonic of both lights appears, as shown in Fig. 4.23.

By scanning the delay stage on the 1560 nm beam path, we can find the temporal overlap when the Sum Harmonic Generation (SFG) spectral peak appears at 620 nm.

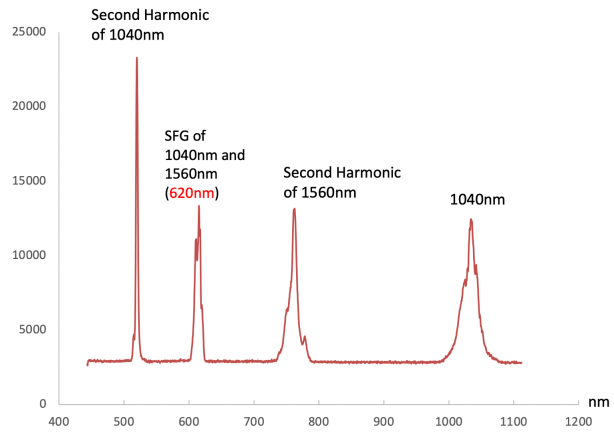

Figure 4.23: The spectrum of the light after the temporal-overlap-checking BBO. The second harmonics of 1040-nm light and 1560-nm light, the 1040-nm peaks are labeled. The SFG of 1040 nm and 1560 nm is highlighted as it indicates the temporal overlap.

4.5 Experimental Results

4.5.1 Detection-frequency Dependence of 2+3 QuIC

To find the QuIC current, we varied the relative phase delay with a piezo on the 1040-nm arm. Not sure about the transmission bandwidth of the MSM device, we also studied the SNR of QuIC by setting the detection frequency to 32 Hz, 64 KHz, and 128 KHz. 2+3 QuIC detected at 32 KHz is the first 10 seconds of the data in Fig. 4.24. The signal was taken from the X channel of the Lock-in amplifier. The AlGaAs sample was directly connected to the current input of the Lock-in amplifier (input impedance = 10 $k\Omega$). The delay stage on the 1040-nm arm is oscillated at 0.5 Hz by a piezo. The signal strength decreases significantly when offsetting the reference frequency, indicating a QuIC current bandwidth similar to the bandwidth of the stabilized beat

note. Note that the QuIC signal was still observable even when using the internal reference frequency of the Lock-in Amplifier or a separate external reference frequency. However, the signal-to-noise ratio of QuIC was significantly reduced because of the phase drift between the DDS clock and the Lock-in Amplifier clock.

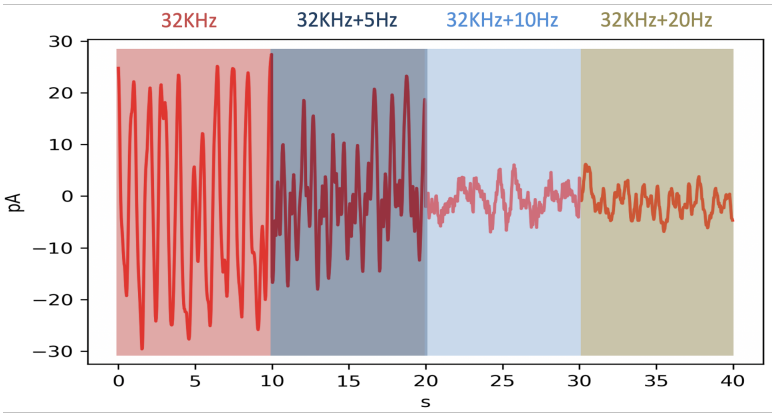

Figure 4.24: The 2+3 QuIC current from the horizontal electrode pair as a function of time. The four colored regions from left to right show the 2+3 QuIC current detected at 32 KHz, 32 KHz + 5 Hz, 32 KHz + 10 Hz, and 32 KHz + 20 Hz, respectively. The fields of 1040 nm and 1560 nm are co-linearly polarized across the horizontal electrode pair ($\langle 100 \rangle$ crystal axis).

4.5.2 Relative-phase Dependence of 2+3 QuIC

To further optimize the signal-to-noise ratio of this QuIC oscillation, we built an enclosure box for the setup to reduce the relative phase noise caused by air turbulence. The temporal delay was scanned to maximize the QuIC current. A black box isolated the sample to avoid noise caused by green stray light. The spatial overlap was optimized by checking the alignment after a few meters. The beam focal spots were placed in the center of the two pairs of electrodes. The longitudinal position of the MSM device was optimized so that the number of carriers induced by three-photon absorption was maximized. More importantly, changing the QuIC detection frequency from 32 KHz to 128 KHz significantly increased SNR. The optimized 2+3 QuIC was plotted as a

function of time in Fig. 4.25. The piezo oscillation amplitude and frequency are set to be $\sim \frac{3\times 2\pi\times 1040}{2\pi\times 2\times 2}\, nm = 780\, nm$ and 0.5 Hz, respectively. The turn-around points are at $t = 0s$, $1s$, $2s$. The 2+3 QuIC current oscillation aligns well with the sine function fit shown as the red curve in Fig. 4.25. This relative-phase dependence is consistent with the previous study done by our group[49] but with a significantly better SNR. The setup was completely rebuilt to reduce the relative-phase noise and the noise of the RF driving powers.

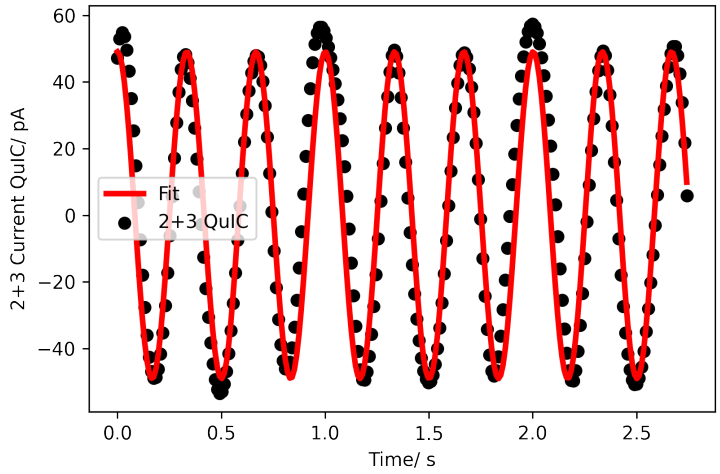

Figure 4.25: The 2+3 QuIC current (black dots) from the horizontal electrode pair as a function of time. The detection frequency is 128 KHz. A sine function (red curve) fits the 2+3 QuIC current. The fields of 1040 nm and 1560 nm are co-linearly polarized across the horizontal electrode pair ($\langle 100\rangle$ crystal axis). The piezo oscillation amplitude and frequency are ∼780 nm and 0.5 Hz, respectively.

4.5.3 Polarization Dependence of 1+2 QuIC and 2+3 QuIC (dual-polarization rotation)

With a better SNR, we now study the dependence of QuIC current on the polarization of two beams. The polarization of two beams was rotated together by two HWPs

moving at an angular frequency of $9°/s$. The 1+2 and 2+3 QuIC signals were taken while the polarization of beams rotated. The 1+2 and 2+3 QuIC signals are shown as a function of the angle of polarization in Fig. 4.26. Since the direction of QuIC currents is related to the direction of co-linear polarizations, the rotation of polarization imposes an amplitude modulation to the phase-induced QuIC oscillation. As shown in Fig. 4.26 (b), if turn-around points inside a burst occur mostly above zero (below zero), the turn-around points inside the next burst will mostly be below zero (above zero). This indicates a phase shift over a 90° rotation of HWPs. We denote the angle between the fast axis of HWP and the x-axis (horizontal direction) as θ. The polarization of beams when $\theta = 0°$ is identical to the polarization of beams when $\theta = 90°$, which means that the strength of the QuIC signal is unchanged. However, since the polarization of light is horizontal, the phase of the electric field is delayed by π when the fast axis of HWP moves from 0° to 90°. Therefore, the change of relative phase parameter is: $\Delta\phi_{relative} = 3\Delta\phi_{1560nm} - 2\Delta\phi_{1040nm} = 3\pi - 2\pi = \pi$. Therefore, the sign of QuIC flips as HWP rotates by 90°. The bursts in 2+3 QuIC are 'narrower' than the bursts in 1+2 QuIC on the time domain, which indicates a "narrower" current flux in real space in 2+3 QuIC. Later in the thesis, it will be shown that this is related to the localization of injected carriers in the $\boldsymbol{k}$-space in the 2+3 QuIC process. The drawbacks of this sampling method are: 1. Although the sampling rate of the QuIC signal is 128/s, the effective sampling rate of the polarization dependence is much smaller because only the peaks of phase-induced oscillation are "useful." 2. The slow drift of the relative phase caused by air flow accumulates and affects the signal strength, especially when the angular frequency of HWPs is small. The most effective way to increase the sampling rate of polarization dependence measurement is to get rid of the phase-induced QuIC oscillation. It can be achieved by stopping the slow ramp for 1+2 QuIC and the delay line oscillation for 2+3 QuIC. Fig. 4.27 and

Fig. 4.28 are schematics of 1+2 QuIC polarization dependence measurement and 2+3 QuIC polarization dependence measurement, respectively. The QuIC signals collected by horizontal and vertical electrode pairs are measured by Lock-in Amplifier A and B, respectively, while rotating the two HWPs at the same rate ($720°/s$). Thirty shots of QuIC signal over a 360° rotation of polarizations are averaged. The shaded areas represent the variance of data. The 1+2 QuIC and 2+3 QuIC collected by vertical electrode pairs are shown as dashed lines in Fig. 4.31 (a) and Fig. 4.31 (b), respectively. The 1+2 QuIC and 2+3 QuIC collected by horizontal electrode pairs were shown as dotted lines in Fig. 4.31 (a) and Fig. 4.31 (b), respectively. The amplitude of QuIC currents is plotted on polar coordinates, and the + and − signs of QuIC currents are indicated by the red and purple colors, respectively. The polarization dependence curves are consistent with the envelopes of the phase-induced QuIC oscillation in Fig. 4.26. For both 1+2 QuIC and 2+3 QuIC, the maximal vertical QuIC current occurs at the minimum of horizontal QuIC current. In other words, for both 1+2 QuIC and 2+3 QuIC, the vertical QuIC current is 90° out of phase relative to the horizontal current. This feature is consistent with Eq. 29 and Eq. 31. The maxima of the vertical 1+2 QuIC and vertical 2+3 QuIC are $3.49\,nA$ and $51.64\,pA$ respectively. The amplitudes of horizontal 1+2 QuIC and 2+3 QuIC were characterized according to the resistance between the horizontal electrode pair and the resistance between the vertical electrode pair.

4.5.4 Current Injection Model

In Fig. 4.29, the angle between a direction $\boldsymbol{k}$ in the $\boldsymbol{k}$-space and <100> crystal axis ($\boldsymbol{k}_x$) is denoted by θ. The direction of polarization of two-color electric field $\boldsymbol{k}_p$ and <100> crystal axis (k_x) is denoted by θ_p. Phenomenologically, the injection rate of carriers can be approximately treated as a stationary distribution relative to the direction

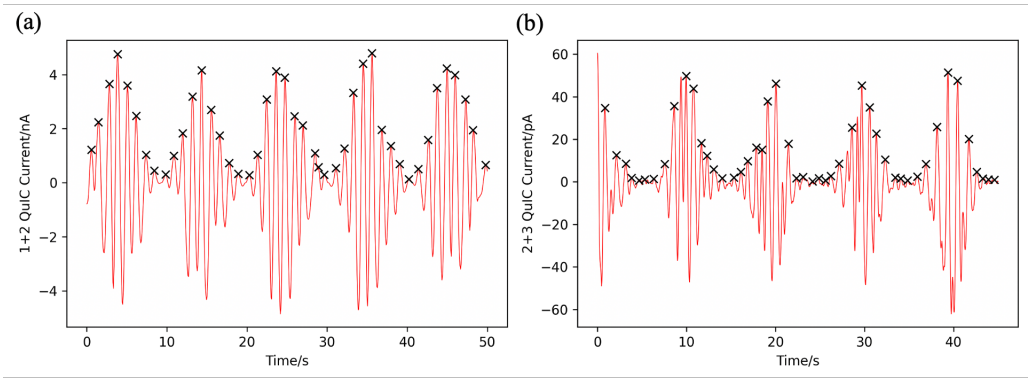

Figure 4.26: (a) the 1+2 QuIC current from the horizontal electrode pair (red curve) detected at 2 KHz as a function of time. (b) the 2+3 QuIC current from the hot=rizontal electrode pair (red curve) detected at 128 KHz as a function of time. In both figures, the polarization of two-color light fields is rotated with an angular frequency of $9 \circ /s$, which results in the amplitude modulation of the relative-phase-induced oscillations. The cross marks denote the peaks of current oscillations. The piezo oscillation and polarization rotation manipulate the current simultaneously.

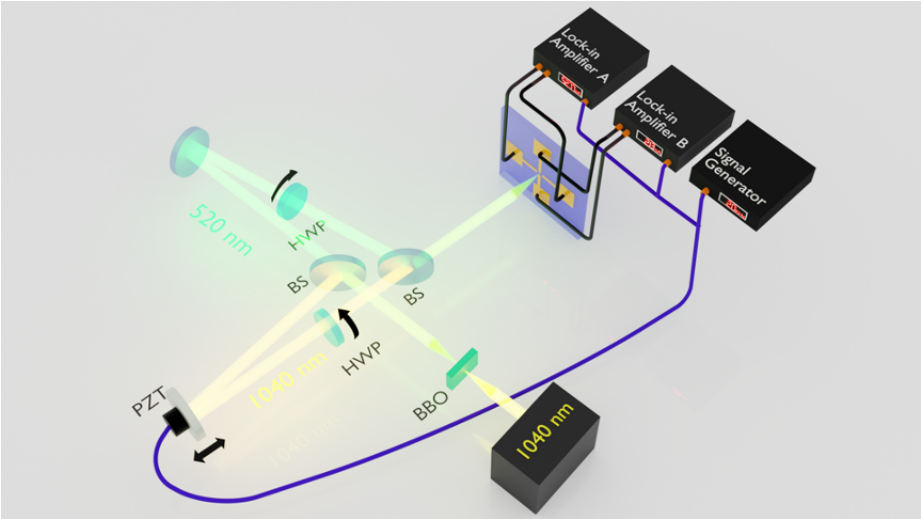

Figure 4.27: A schematic diagram of the 1+2 QuIC polarization dependence setup. A prism pair separates (denoted by a BS for simplicity) the 1040 nm light and its second harmonic. The two half-wave plates on the two arms of the two-color interferometer rotate at the same angular rate simultaneously. A PZT dithers the 1040-nm arm at 2 KHz. Two Lock-in Amplifiers measure 2+3 QuIC currents from the horizontal and vertical electrode pairs.

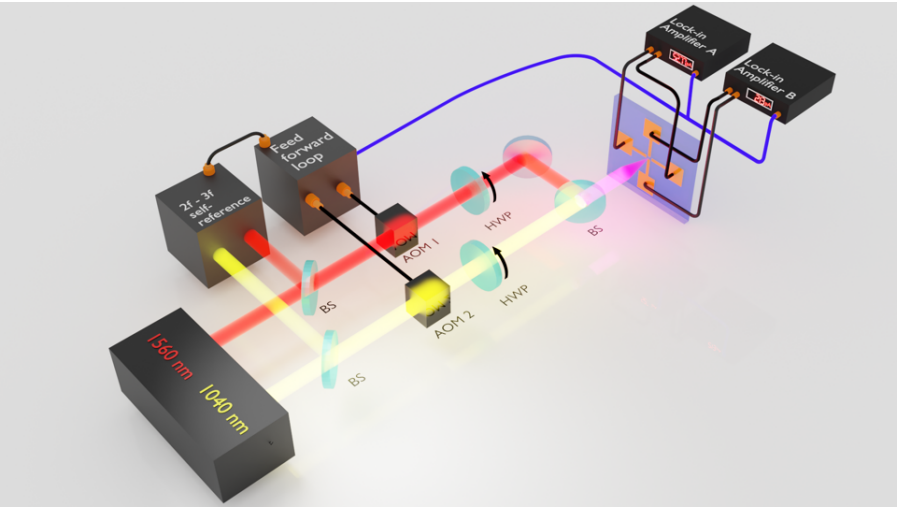

Figure 4.28: A schematic diagram of the 2+3 QuIC polarization dependence setup. The feed-forward and feedback loops stabilize and control the offset frequencies of 1040-nm OFC and 1560-nm oFC. The two half-wave plates on the two arms of the two-color interferometer rotate at the same angular rate simultaneously. Two Lock-in Amplifiers measure 2+3 QuIC currents from the horizontal and vertical electrode pairs.

of polarization. In other words, the injected current distribution rotates with the polarization of two-color light. The relative phase $\phi_{2+3}^{relative}$ changes the injection rate distribution. When $\phi_{2+3}^{relative} = \pi/2$ or $-\pi/2$, the imbalance between the injection rates at $\boldsymbol{k}$ and $-\boldsymbol{k}$ maximizes, resulting a large QuIC current. The injection rate distribution of 2+3 QuIC along $\vec{\boldsymbol{k}}$ can be expressed as a function of θ, θ_p, and $\Delta\phi_{2+3}^{relative}$:

$$\eta_{2+3}(\theta, \theta_p, \Delta\phi_{2+3}^{relative}) = A_1(C_1 cos(\theta - \theta_p) + sin(\Delta\phi_{2+3}^{relative}))^5 cos(\theta) + B_1(C_1 cos(\theta - \theta_p) + sin(\Delta\phi_{2+3}^{relative}))^3 sin^2(\theta - \theta_p) cos(\theta) \tag{4.39}$$

Since the direction of $\boldsymbol{k}$ vector is identical to the direction of carrier velocity in the real space, $\eta(\theta, \theta_p, \Delta\phi^{relative}) \left|E_{1040}\right|^2 \left|E_{1560}\right|^3$ is proportional to the current intensity distribution in the real space. The electrode pairs collect the integral of current intensity over $\theta_{electrode}$. From the contact geometry, $\theta_{electrode} \approx (-\frac{\pi}{9}, \frac{\pi}{9})$

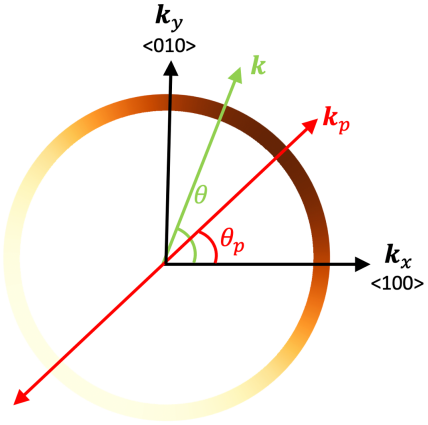

Figure 4.29: An example of the injection rate of carriers on the "ring" in the $\boldsymbol{k}$-space. The darkness of the color denotes the injection rate. The red double arrow denotes the polarization of the two-color light field $\boldsymbol{k}_p$

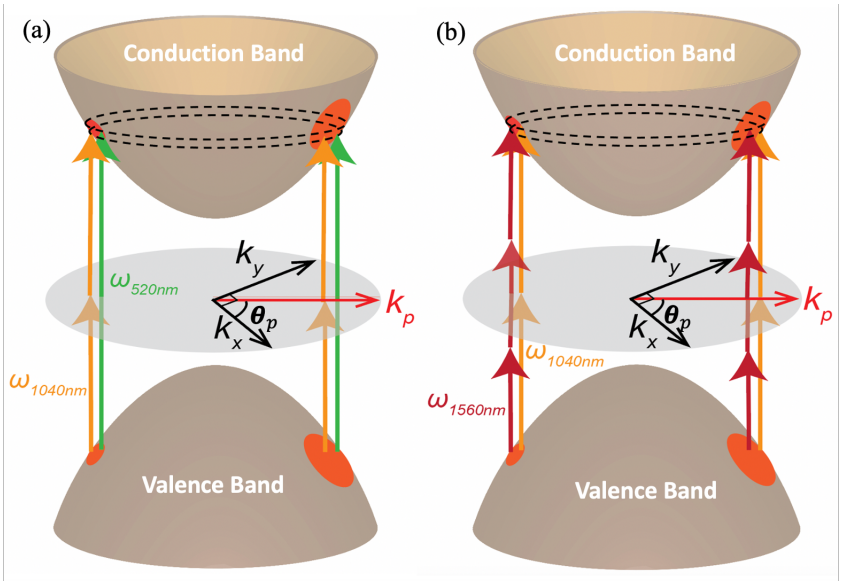

Figure 4.30: (a) A schematic illustration of 1+2 QuIC on the semiconductor band structure. (b) A schematic illustration of 2+3 QuIC on semiconductor band structure. In both graphs, the polarization of the two-color field is denoted by the red arrow.

For the horizontal electrode pair, 2+3 QuIC current can be written as:

$$I_{2+3}^{horizontal}(\theta_p) = \int_{-\frac{\pi}{9}}^{\frac{\pi}{9}} \eta_{2+3}(\theta, \theta_p, \frac{\pi}{2}) d\theta \left|E_{1040}\right|^2 \left|E_{1560}\right|^3 - \int_{-(\frac{\pi}{9}+\pi)}^{\frac{\pi}{9}+\pi} \eta_{2+3}(\theta, \theta_p, \frac{\pi}{2}) d\theta \left|E_{1040}\right|^2 \left|E_{1560}\right|^3 \tag{4.40}$$

For the vertical electrode pair, 2+3 QuIC current can be written as:

$$I_{2+3}^{vertical}(\theta_p) = \int_{-\frac{\pi}{9}+\frac{\pi}{2}}^{\frac{\pi}{9}+\frac{\pi}{2}} \eta_{2+3}(\theta, \theta_p, \frac{\pi}{2}) d\theta \left|E_{1040}\right|^2 \left|E_{1560}\right|^3 - \int_{-(\frac{\pi}{9}+\pi)+\frac{\pi}{2}}^{\frac{\pi}{9}+\pi+\frac{\pi}{2}} \eta_{2+3}(\theta, \theta_p, \frac{\pi}{2}) d\theta \left|E_{1040}\right|^2 \left|E_{1560}\right|^3 \tag{4.41}$$

Similarly, the injection rate distribution of 2+3 QuIC along $\vec{\boldsymbol{k}}$ can be expressed as a function of θ, θ_p, and $\Delta\phi_{1+2}^{relative}$:

$$\eta_{1+2}(\theta, \theta_p, \Delta\phi_{1+2}^{relative}) = (A_0(C_0 cos(\theta - \theta_p)) + sin(\Delta\phi_{1+2}^{relative}))^3 cos(\theta) + B_0(C_0 cos(\theta - \theta_p) + sin(\Delta\phi_{1+2}^{relative})) sin(\theta - \theta_p)^2 cos(\theta) \tag{4.42}$$

1+2 QuIC current collected by the horizontal electrode pair can be written as:

$$I_{1+2}^{horizontal}(\theta_p) = \int_{-\frac{\pi}{9}}^{\frac{\pi}{9}} \eta_{1+2}(\theta, \theta_p, \frac{\pi}{2}) d\theta \left|E_{520}\right| \left|E_{1040}\right|^2 - \int_{-(\frac{\pi}{9}+\pi)}^{\frac{\pi}{9}+\pi} \eta_{1+2}(\theta, \theta_p, \frac{\pi}{2}) d\theta \left|E_{520}\right| \left|E_{1040}\right|^2 \tag{4.43}$$

1+2 QuIC current collected by the vertical electrode pair can be written as:

$$I_{1+2}^{vertical}(\theta_p) = \int_{-\frac{\pi}{9}+\frac{\pi}{2}}^{\frac{\pi}{9}+\frac{\pi}{2}} \eta_{1+2}(\theta, \theta_p, \frac{\pi}{2}) d\theta \left|E_{520}\right| \left|E_{1040}\right|^2 - \int_{-(\frac{\pi}{9}+\pi)+\frac{\pi}{2}}^{\frac{\pi}{9}+\pi+\frac{\pi}{2}} \eta_{1+2}(\theta, \theta_p, \frac{\pi}{2}) d\theta \left|E_{520}\right| \left|E_{1040}\right|^2 \tag{4.44}$$

The integrals of injected current distribution are related to the injection rate tensor

elements. For example, η_{2+3}^{xxxxxx} can be written as:

$$\eta_{2+3}^{xxxxxx} = \int_{-\frac{\pi}{9}}^{\frac{\pi}{9}} \eta_{2+3}(\theta, 0, \frac{\pi}{2})d\theta - \int_{\frac{\pi}{9}}^{\frac{3\pi}{9}} \eta_{2+3}(\theta, 0, \frac{\pi}{2})d\theta \tag{4.45}$$

Note that the definition of η_{2+3}^{xxxxxx} is slightly different from the definition in Sipe paper in that the range of integrals is $\frac{2\pi}{9}$ instead of π due to the geometry of electrode pairs. We denote $\eta_{1+2}^{xxxx} |E_{520}| |E_{1040}|^2$ and $\eta_{2+3}^{xxxxxx} |E_{1040}|^2 |E_{1560}|^3$ with $\langle xxxx \rangle_{1+2}$ and $\langle xxxxxx \rangle_{2+3}$ respectively.

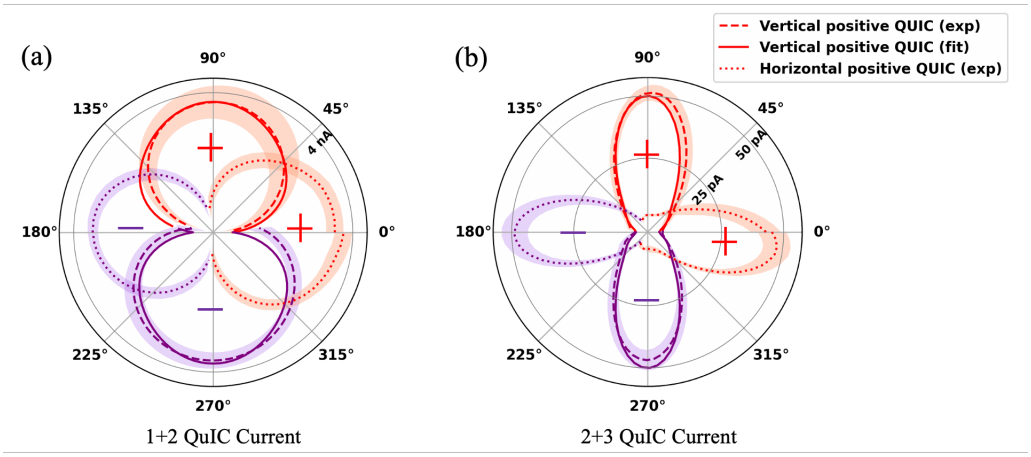

Figure 4.31: (a) The polar plots of 1+2 QuIC currents from the vertical electrode pair and horizontal electrode pair. (b) The polar plots of 2+3 QuIC currents from the vertical electrode pair and horizontal electrode pair. In both graphs, the vertical QuIC currents are fitted by the theory (solid curves). The + (red) and − (purple) signs indicate the sign of QuIC current.

From the maxima in Fig. 4.31, we get:

$$\langle xxxx \rangle \approx 3.49nA, \quad \langle xxxxxx \rangle \approx 51.64pA \tag{4.46}$$

The free parameters in the integrals of injected current distribution are fitted to the

data in Fig. 4.31. The ratio of the free parameters in Eq. 3.41 is:

$$A_0 : B_0 : C_0 \equiv 1.72 : 3.71 : 1 \tag{4.47}$$

The ratio of the free parameters in Eq. 38 is:

$$A_1 : B_1 : C_1 \equiv 0.6 : 1.11 : 1 \tag{4.48}$$

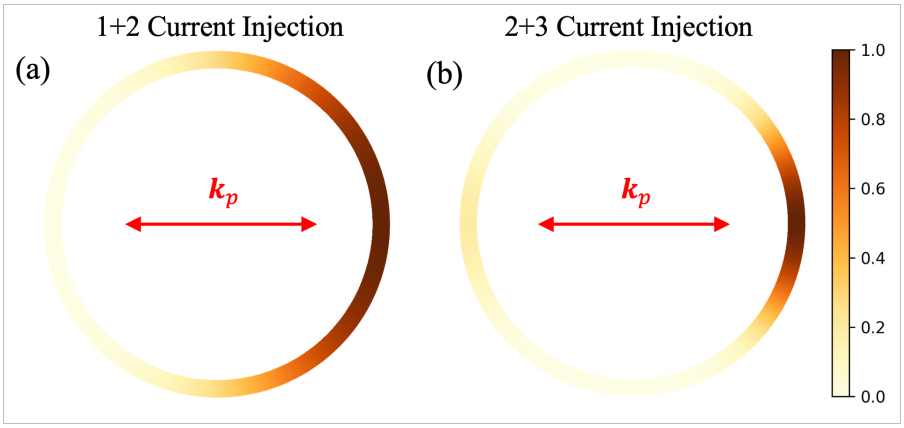

Figure 4.32: (a) polar plot of the fitted injection rate of carriers in the $\boldsymbol{k}$-space. (b) polar plot of the fitted injection rate of carriers in the $\boldsymbol{k}$-space. In both graphs, the two-color light field (red double arrow) is linearly polarized across the horizontal electrode pair.

The normalized 1+2 QuIC and 2+3 QuIC current injection distributions maximize along $\boldsymbol{k}_x$ when the polarization of two-color excitation is horizontal, as shown in Fig. 4.32. The FWHM of the 1+2 QuIC injection peak is $\sim 103.2°$ while the FWHM of the 2=3 QuIC injection peak is $\sim 57.3°$. This indicates that the localization ratio of 1+2 QuIC and 2+3 QuIC is ~ 0.56. This result is consistent with the localization of 2+3 QuIC predicted in Sipe paper.

The imbalance of the current injection rates at $\boldsymbol{k}$ and $\boldsymbol{k}^{'}$ changes with relative phase parameter $\phi^{relative}$. Fig. 4.33 shows the relative-phase dependence of the fitted current

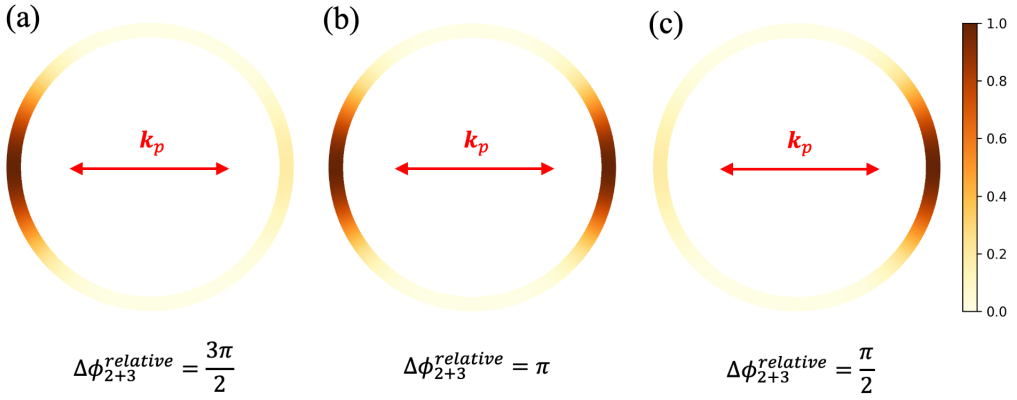

Figure 4.33: Polar plots of the fitted injection rate of carriers in the $\boldsymbol{k}$-space when the relative phase of the fields of 1040 nm and 1560 nm is: (a) $\frac{3\pi}{2}$, (b) π, (c) $\frac{\pi}{2}$. The two-color light field (red double arrow) is linearly polarized across the horizontal electrode pair.

injection distribution when $\boldsymbol{k}_p$ is horizontal. The current injection rate has inversion symmetry when $\phi_{2+3}^{relative} = \pi$, resulting in zero net current. The imbalance changes direction when $\phi_{2+3}^{relative}$ changes from $\frac{3\pi}{2}$ to $\frac{\pi}{2}$. This relative phase dependence also exists for 1+2 QuIC.

4.5.5 Polarization Dependence of 1+2 QuIC and 2+3 QuIC (single-polarization rotation)

The QuIC signals were taken when the polarization of only one color was rotated. The vertical QuIC currents are plotted as dashed lines, and the horizontal QuIC currents are plotted as dotted lines. Colored areas represent the variance of data. As shown in Fig. 4.34 (a) and Fig. 4.35 (b), the 1+2 QuIC when rotating 520-nm and the 2+3 QuIC when rotating 1560-nm go across 0. This indicates that the direction of 1+2 QuIC current and 2+3 QuIC follow the polarization of 520 nm light and the polarization of 1560 nm light, respectively. This feature is consistent with the prediction in Ref. [10]. The behavior of 2+3 QuIC when rotating 1560-nm light polarization is similar to the

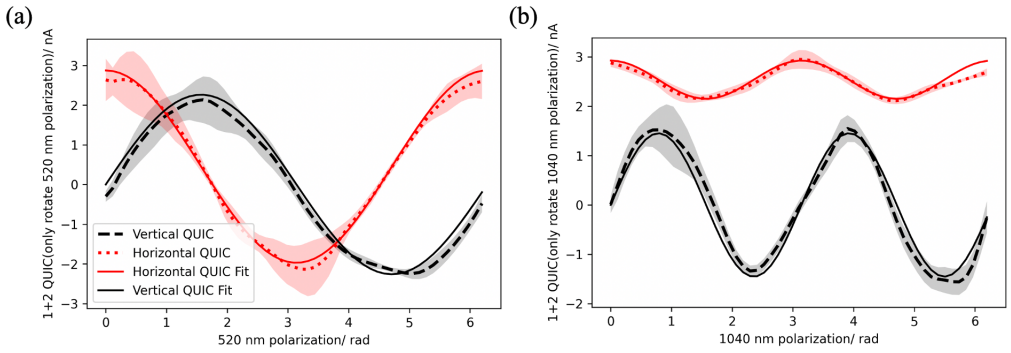

Figure 4.34: (a) 1+2 QuIC currents from the horizontal electrode pair (red dotted line) and vertical electrode pair (black dashed line) are plotted as functions of the polarization of 520-nm light field. The 1040-nm light field is linearly polarized across the horizontal electrode pair. (b) 1+2 QuIC currents from the horizontal electrode pair (red dotted line) and vertical electrode pair (black dashed line) are plotted as functions of the polarization of 1040-nm light field. The 520-nm light field is linearly polarized across the horizontal electrode pair. In both graphs, the colored regions denote the variances.

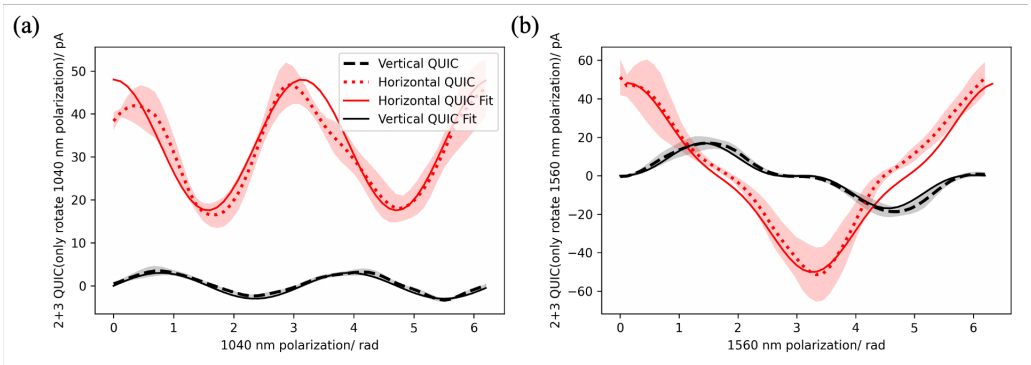

Figure 4.35: (a) 2+3 QuIC currents from the horizontal electrode pair (red dotted line) and vertical electrode pair (black dashed line) are plotted as functions of the polarization of 1040-nm light field. The 1560-nm light field is linearly polarized across the horizontal electrode pair. (b) 2+3 QuIC currents from the horizontal electrode pair (red dotted line) and vertical electrode pair (black dashed line) are plotted as functions of the polarization of 1560-nm light field. The 1040-nm light field is linearly polarized across the horizontal electrode pair. In both graphs, the colored regions denote the variances.

previous study [49].

The horizontal 1+2 QuIC when rotating the polarization of 520-nm light can be written as a function of θ_p:

$$I_{1+2}^{horizontal}(\theta_p^{520}) = \eta_{1+2}^{xxxx} \left|E_{520}\right| \left|E_{1040}\right|^2 cos(\theta_p^{520}) = \langle xxxx \rangle \, cos(\theta_p^{520}) \tag{4.49}$$

The vertical 1+2 QuIC, when rotating the polarization of 520-nm light can be written as a function of θ_p:

$$I_{1+2}^{vertical}(\theta_p^{520}) = \langle yyyy \rangle \, sin(\theta_p^{520}) \tag{4.50}$$

The horizontal 1+2 QuIC when rotating the polarization of 1040-nm light can be written as a function of θ_p:

$$I_{1+2}^{horizontal}(\theta_p^{1040}) = \langle xxxx \rangle \, cos^2(\theta_p^{1040}) + \langle xyyx \rangle \, sin^2(\theta_p^{1040}) \tag{4.51}$$

The vertical 1+2 QuIC, when rotating the polarization of 1040-nm light, can be written as a function of θ_p:

$$I_{1+2}^{vertical}(\theta_p^{1040}) = 2 \langle yyxx \rangle \, cos(\theta_p^{1040}) sin(\theta_p^{1040}) \tag{4.52}$$

We used the same three independent injection coefficients to fit the four curves in Fig. 4.34:

$$\langle xxxx \rangle \approx 2.9nA, \;\; \langle yyxx \rangle \approx 1.1nA, \;\; \langle yxxy \rangle \approx 2.3nA \tag{4.53}$$

The horizontal 2+3 QuIC when rotating the polarization of 1040-nm light can be

written as a function of θ_p:

$$I_{2+3}^{horizontal}(\theta_p^{1040}) = \langle xxxxxx \rangle \, cos^2(\theta_p^{1040}) + \langle xxxxyy \rangle \, sin^2(\theta_p^{1040}) \tag{4.54}$$

The vertical 2+3 QuIC, when rotating the polarization of 1040-nm light, can be written as a function of θ_p:

$$I_{2+3}^{vertical}(\theta_p^{1040}) = 2 \, \langle yxxxyx \rangle \, cos(\theta_p^{1040}) sin(\theta_p^{1040}) \tag{4.55}$$

The horizontal 2+3 QuIC when rotating the polarization of 1560-nm light can be written as a function of θ_p:

$$I_{2+3}^{horizontal}(\theta_p^{1560}) = \langle xxxxxx \rangle \, cos^3(\theta_p^{1560}) + \langle xxyyxx \rangle \, cos(\theta_p^{1560}) sin^2(\theta_p^{1560}) \tag{4.56}$$

The vertical 2+3 QuIC, when rotating the polarization of 1560-nm light, can be written as a function of θ_p:

$$I_{2+3}^{vertical}(\theta_p^{520}) = \langle yyyyyy \rangle \, sin^3(\theta_p^{1560}) + 3 \, \langle yxxyxx \rangle \, sin(\theta_p^{1560}) cos^2(\theta_p^{1560}) \tag{4.57}$$

We used the same five independent injection coefficients to fit the four curves in Fig. 4.35:

$$\langle xxxxxx \rangle \approx 48.2pA, \;\; \langle xxxxyy \rangle \approx 16.5pA, \;\; \langle xxyyxx \rangle \approx 7.2pA \tag{4.58}$$

$$\langle yxxyxx \rangle \approx 2.8pA, \;\; \langle yxxxyx \rangle \approx 1.4pA \tag{4.59}$$

4.5.6 Discussion

Both in 1+2 QuIC and 2+3 QuIC, the optimal longitudinal position of the sample is closer to the focal plane of the light with lower photon energy. This indicates that the QuIC current is limited by the number of carriers generated from the higher-order optical absorption. The QuIC current generation area is the "effective beam spot," where the two beam focal spots overlap. The beam diameters of the 1040-nm beam and the 1560-nm beam before the 60X objective are 1.6 mm and 2.17 mm, respectively. Therefore, the current generation area of 1+2 QuIC is the focal spot of the 1040-nm beam (diameter of 2.13 μm). The current generation area of 2+3 QuIC is the focal spot of the 1560-nm beam (diameter of 2.38 μm). This shows that the generation area is not a contributing factor to the difference in polarization dependencies of 1+2 QuIC and 2+3 QuIC.

The refractive indices of AlGaAs for 520 nm, 1040 nm, and 1560 nm are 3.92, 3.34, and 3.28, respectively. As two of these lights propagate inside the crystal, the change of relative phase can be written as:

$$\Delta\phi_{1+2}^{relative} = [2 \times \frac{2\pi n_{1040nm}}{\lambda_{1040nm}} - \frac{2\pi n_{520nm}}{\lambda_{520nm}}]z \tag{4.60}$$

$$\Delta\phi_{2+3}^{relative} = [3 \times \frac{2\pi n_{1560nm}}{\lambda_{1560nm}} - 2 \times \frac{2\pi n_{1040nm}}{\lambda_{1040nm}}]z \tag{4.61}$$

For 2+3 QuIC, a relative phase shift of π can be achieved with a propagation of $4.34\mu m$. Given that the thickness of the AlGaAs layer is $4\mu m$, we know: 1. the Rayleigh lengths are longer than the layer thickness. In other words, the wavefronts remain flat inside the crystal. 2. the QuIC currents generated at different depths won't cancel out because the light intensity exponentially decays. For 1+2 QuIC, a relative phase shift of π can

be achieved with a propagation of 224 nm. Although it is much shorter than the layer thickness, we also know 90% of the 520-nm light is absorbed after it propagates for 230 nm in the crystal. The current with a flipped direction flows transversely deeper inside the crystal and is much weaker than the current closer to the surface, which has a negligible contribution to the current extracted out of the electrodes.

4.5.7 Summary

In conclusion, we have directly measured the current injected in 1+2 QuIC and 2+3 QuIC, which both have relative-phase dependence, with two perpendicular electrode pairs. We have revealed that the direction of current is directly related to the polarization of the light field. For example, the current from the vertical (Horizontal) electrode pair is minimized when the light fields are horizontally (vertically) polarized. When the two light fields are co-linearly polarized and rotated together, we find that the 2+3 QuIC current has a narrower angular span than the 1+2 current. Our results reveal the localization of carrier injection distribution in the $\boldsymbol{k}$-space in 2+3 QuIC. We extracted a localization ratio of 0.56 based on our proposed current injection model. When only one of the linear polarizations is rotated, we discover that the direction of QuIC currents is mainly determined by the polarization of 520-nm light (in 1+2 QuIC) and the polarization of 1560-nm light (in 2+3 QuIC), which is consistent with the optical injection theory.

CHAPTER 5

Outlook

Our measurements showed that the photocurrents from Ohmic-contact AlGaAs bulk unbiased crystal in QuIC processes are a powerful tool for studying $\boldsymbol{k}$-space distribution of carriers. This localization of carriers in the $\boldsymbol{k}$-space should be transferable to other systems. The localization of carriers has been predicted to exist in Transition metal dichalcogenides (TMD) materials such as $MoSe_2$, WSe_2 [10]. Combined with recent advancements in Ohmic contact engineering in 2D materials [50], QuIC has the potential to open up new opportunities in studying the band structure of novel 2D materials.

As mentioned in Chapter 4, the wavefronts of the two lights of different colors are slightly offset because of the inevitable chromatic aberration. This limits the sample's longitudinal range where the QuIC signal has a low SNR. The QuIC currents obtained from mismatched wavefronts are shown in Appendix B. Using parabolic mirrors to focus the two lights can eliminate the chromatic aberration, but the focal spots need to be small enough to achieve similar excitation densities. Another way that can potentially help is slightly changing the divergence of the beams before the objective lens to image them on the same plane.

We demonstrated the angular distribution of QuIC currents by collecting them with two perpendicular pairs of electrodes. The engineering of such Ohmic electrodes can be

further improved in the future. More pairs of electrodes can be used to study the current distribution with a better angular resolution. As mentioned in Appendix A, Heidelberg μPG 501 Mask Maker was used to write electrode patterns on the photoresist. The dimensions of our electrodes are close to the feature resolution of Heidelberg μPG 501 Mask Maker. Therefore, it is tricky to write more complicated patterns. However, GCA AS200 AutoStep, which is more compatible with wafers instead of pieces, can offer better feature resolution and alignment control. The spacing between electrodes can also be further explored to study the free mean path of the injected carriers.

The scattering of carriers in the conduction band is a remaining interesting question. Namely, after the carriers are optically injected into the conduction band, how do they scatter on the same energy level? In future work, we can apply different polarization schemes to generate various $\boldsymbol{k}$-space distributions. Pump-probe scheme can be integrated into the QuIC experiment to study carrier dynamics. The time delay between the two pulses of different photon energies can also be varied to study the interference dynamics of the two optical transition pathways.

APPENDIX A

Ohmic Contact Fabrication

There have been a few early reviews on different stages of Ohmic contact formation[51, 52, 53, 54, 55]. The negative contributing factors to good ohmic contact include Au spiking, poor morphology, temperature stability, and edge definition. One good solution is to use a low band gap alloy buffer layer. The GeAu contact has been studied extensively for III-V compounds such as GaAs, InP, and GaN [55]. Ni can be used as a layer between the semiconductor and GeAu to improve the wettability [56] and avoid the "balling up" process. Ni is also important for other reasons: reducing the surface oxides, and reacting with GaAs at low temperatures possibly forming electrically important NiAs phases [57]; reducing the loss of As during contact formation [58]. Annealing time is also a determining factor of the ohmic contact formation. GeAuNi contact has shown a strong propensity to form AuGa, which has been observed in TEM at temperatures of 420°C and above [57]. Rapid thermal annealing has been proven to be effective for stopping complex alloy reactions, which limits the tendency for total consumption of the Au. It has been shown that the annealing temperature affects the ohmic contact formation of PtTiGePd on highly C-dope AlGaAs [59]. The out-diffusion of As is critical to good p-type ohmic contact. And it only starts to occur when the annealing temperature is above $530°C$.

The fabrication of ohmic contacts on AlGaAs was done in The University of Michi-

gan Lurie Nanofabrication Facility (LNF). The following are the steps of our ohmic contact fabrication:

1: Clean the wafer at the solvent bench with water, IPA and Acetone.

2: Use a spinner to create a layer of photoresist (SPR 220 (3.0)). The thickness of the photoresist layer is $3\mu m$.

3. Softbake: bake the wafer at 110° for 90 seconds.

4. Exposure: use Heidelberg μPG 501 Mask Maker to write the electrode pattern onto the photoresist. The exposure time should be 110 ms.

5. Development: use CEE Developer 1 with AZ 726 to develop the sample for 30 seconds.

6. Plasma Etching: use BCl_3 and HBr gases to etch the sample for 1 minute on LAM 9400. The etching depth is $\sim 0.8\mu m$. If the etching depth is too low, Ohmic contact will either not form or will form with a much longer annealing time.

7. Metal deposition: the order of the five layers is Au Ni Ge Au Ni (110nm, 30nm, 20nm, 10nm, 5nm) from top to bottom [60]. The deposition rates need to be small to achieve uniform densities of metal layers.

8. Annealing: different annealing times and temperatures were experimented with. Annealing at $500°C$ for 5 mins gives reproducible and good-quality ohmic contact. Note that if the annealing temperature is too high, the surface of metal contact will start melting and form "bumps". The quality of the ohmic contact highly depends on the cleanness of the metal-semiconductor interface. If there is residue of photoresist on the sample or the photoresist is initially non-uniform across the sample, Ohmic contact will have higher resistance.

APPENDIX B

Wavefront Mismatch

When the wavefront of the two lights of different colors mismatch, the relative phase can change inside the beam spots, generating QuIC current in different directions on the same plane, as shown in Fig. B.1. Fig. B.2 shows the 2+3 QuIC when the sample is 20 μm inside (optimal - 20 μm) and 20 μm outside (optimal + 20 μm) the optimal longitudinal position. The QuIC currents seem to be much noisier than Fig. 4.25. It is potentially because: 1. currents flowing in different directions interfere on the same plane. 2: the systematic noise is more significant as the absolute amplitude of QuIC is reduced with the excitation density.

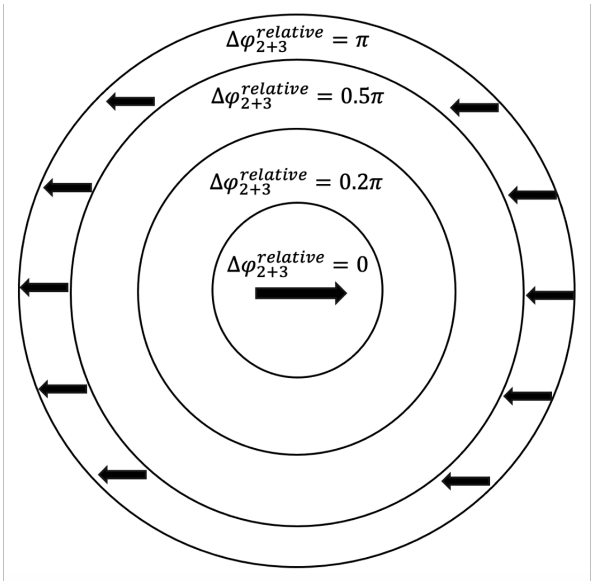

Figure B.1: A schematic illustration of QuIC current inside beam focal spots when the wavefronts are mismatched. The relative phases at different locations are labeled. The black arrows denote the direction of QuIC currents.

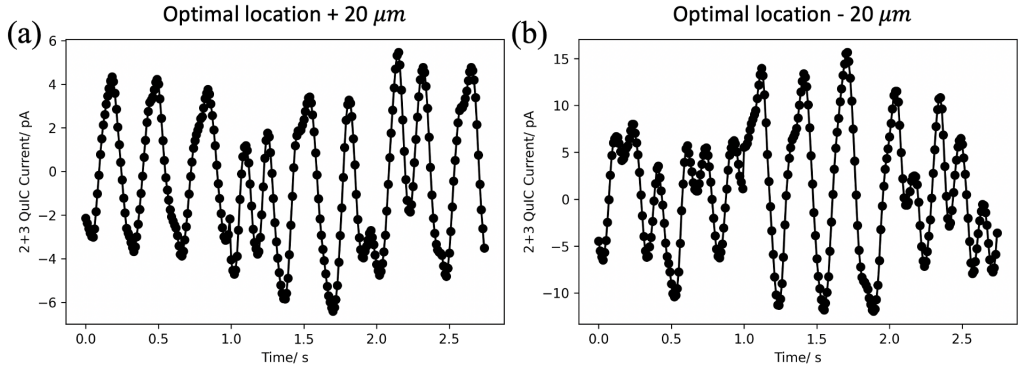

Figure B.2: (a) The 2+3 QuIC current from the horizontal electrode pair when the sample is 20 μm inside (optimal - 20 μm). (b) The 2+3 QuIC current from the horizontal electrode pair when the sample is 20 μm outside (optimal + 20 μm).

BIBLIOGRAPHY

[1] J Gudde, M Rohleder, Torsten Meier, SW Koch, and U Hofer. Time-resolved investigation of coherently controlled electric currents at a metal surface. *Science*, 318(5854):1287–1291, 2007.

[2] Hamsa Naser, Hayder Abduljalil, and Mudar Abdulsattar. Study the effect of sulfur atoms on the electronic structure for the gallium arsenide nanocrystals of eight atoms. *Journal of Babylon University/Pure and Applied Sciences*, 21:1794–1802, 01 2013.

[3] T.E. Schlesinger. *Gallium Arsenide*, pages 3431–3435. 12 2001.

[4] A. Hache, J.E. Sipe, and H.M. van Driel. Quantum interference control of electrical currents in gaas. *IEEE Journal of Quantum Electronics*, 34(7):1144–1154, 1998.

[5] SA Lyon. Spectroscopy of hot carriers in semiconductors. *Journal of luminescence*, 35(3):121–154, 1986.

[6] J. Rioux and J.E. Sipe. Optical injection processes in semiconductors. *Physica E Low-Dimensional Systems and Nanostructures*, 45:1–15, 08 2012.

[7] Alain Haché. *Coherent control of photocurrent in bulk semiconductors*. PhD thesis, 1998.

[8] https://www.fiberlabs.com/glossary/erbium-doped-fiber-amplifier/.

[9] Ali Albalawi, Hongna Zhu, Stefano Taccheo, Alessandro Chiasera, Maurizio Ferrari, Jafar Alzubi, and Omar Alzubi. Numerical modeling of the impact of pump wavelength on yb-doped fiber amplifier performance. *Optical and Quantum Electronics*, 48, 10 2016.

[10] Perry T. Mahon, Rodrigo A. Muniz, and J. E. Sipe. Quantum interference control of localized carrier distributions in the brillouin zone. *Phys. Rev. B*, 100:075203, Aug 2019.

[11] Sebastian Koke, Christian Grebing, Harald Frei, Alexandria Anderson, Andreas Assion, and Günter Steinmeyer. Direct frequency comb synthesis with arbitrary offset and shot-noise-limited phase noise. *Nature Photonics*, 4(7):462–465, 2010.

[12] EA Manykin. Quantum interference and coherent control. *Laser physics*, 11(1):60–67, 2001.

[13] Moshe Shapiro and Paul Brumer. *Principles of the quantum control of molecular processes*. 2003.

[14] Gershon Kurizki, Moshe Shapiro, and Paul Brumer. Phase-coherent control of photocurrent directionality in semiconductors. *Physical Review B*, 39(5):3435, 1989.

[15] Moshe Shapiro, John W Hepburn, and Paul Brumer. Simplified laser control of unimolecular reactions: Simultaneous ($\omega 1$, $\omega 3$) excitation. *Chemical physics letters*, 149(5-6):451–454, 1988.

[16] Ce Chen, Yi-Yian Yin, and DS Elliott. Interference between optical transitions. *Physical review letters*, 64(5):507, 1990.

[17] NB Baranova, AN Chudinov, and B Ya Zel'dovich. Polar asymmetry of photoionization by a field with$<$ e3$>\neq$ 0. theory and experiment. *Optics communications*, 79(1-2):116–120, 1990.

[18] NM Lawandy, NB BARANOVA, AN CHUDINOV, and BY ZEL'DOVICH. Comments on polar asymmetry of photoionization by a field with$<$ e3$>\neg=$; o. theory and experiment [nb baranova, an chudinov and b. ya. zel'dovich, optics comm. 79 (1990) 116]. reply. *Optics communications*, 85(4):369–371, 1991.

[19] NB Baranova, AN Chudinov, and B Ya Zel'dovich. Reply to comments on"polar asymmetry of photoionization by a field with$<$ e 3$>\neq$ 0. theory and experiment". *Optics Communications*, 85(4):371–371, 1991.

[20] Ce Chen and DS Elliott. Measurements of optical phase variations using interfering multiphoton ionization processes. *Physical review letters*, 65(14):1737, 1990.

[21] DJ Jackson, JJ Wynne, and PH Kes. Resonance-enhanced multiphoton ionization: Interference effects due to harmonic generation. *Physical Review A*, 28(2):781, 1983.

[22] Yi-Yian Yin, Ce Chen, DS Elliott, and AV Smith. Asymmetric photoelectron angular distributions from interfering photoionization processes. *Physical review letters*, 69(16):2353, 1992.

[23] A Haché, Y Kostoulas, R Atanasov, JLP Hughes, JE Sipe, and HM Van Driel. Observation of coherently controlled photocurrent in unbiased, bulk gaas. *Physical Review Letters*, 78(2):306, 1997.

[24] E Dupont, Paul B Corkum, HC Liu, M Buchanan, and ZR Wasilewski. Phase-controlled currents in semiconductors. *Physical review letters*, 74(18):3596, 1995.

[25] Louis Costa, Markus Betz, Marko Spasenović, Alan D Bristow, and Henry M Van Driel. All-optical injection of ballistic electrical currents in unbiased silicon. *Nature Physics*, 3(9):632–635, 2007.

[26] Ryan W Newson, Jean-Michel Ménard, Christian Sames, Markus Betz, and Henry M van Driel. Coherently controlled ballistic charge currents injected in single-walled carbon nanotubes and graphite. *Nano letters*, 8(6):1586–1589, 2008.

[27] Dong Sun, Charles Divin, Julien Rioux, John E Sipe, Claire Berger, Walt A De Heer, Phillip N First, and Theodore B Norris. Coherent control of ballistic photocurrents in multilayer epitaxial graphene using quantum interference. *Nano letters*, 10(4):1293–1296, 2010.

[28] Shawn Sederberg, Fanqi Kong, Felix Hufnagel, Chunmei Zhang, Ebrahim Karimi, and Paul B Corkum. Vectorized optoelectronic control and metrology in a semiconductor. *Nature Photonics*, 14(11):680–685, 2020.

[29] TM Fortier, PA Roos, DJ Jones, Steven T Cundiff, RDR Bhat, and John E Sipe. Carrier-envelope phase-controlled quantum interference of injected photocurrents in semiconductors. *Physical review letters*, 92(14):147403, 2004.

[30] PA Roos, Xiaoqin Li, RP Smith, Jessica A Pipis, TM Fortier, and Steven T Cundiff. Solid-state carrier-envelope phase stabilization via quantum interference control of injected photocurrents. *Optics letters*, 30(7):735–737, 2005.

[31] R Atanasov, A Haché, JLP Hughes, HM Van Driel, and JE Sipe. Coherent control of photocurrent generation in bulk semiconductors. *Physical review letters*, 76(10):1703, 1996.

[32] MV Entin. Theory of the coherent photogalvanic effect. *SOVIET PHYSICS SEMICONDUCTORS-USSR*, 23(6):664–666, 1989.

[33] A Haché, JE Sipe, and HM Van Driel. Quantum interference control of electrical currents in gaas. *IEEE Journal of Quantum Electronics*, 34(7):1144–1154, 1998.

[34] RDR Bhat and JE Sipe. Optically injected spin currents in semiconductors. *Physical Review Letters*, 85(25):5432, 2000.

[35] Martin J Stevens, Arthur L Smirl, RDR Bhat, Ali Najmaie, JE Sipe, and HM Van Driel. Quantum interference control of ballistic pure spin currents in semiconductors. *Physical review letters*, 90(13):136603, 2003.

[36] Jens Hübner, WW Rühle, M Klude, D Hommel, RDR Bhat, JE Sipe, and HM Van Driel. Direct observation of optically injected spin-polarized currents in semiconductors. *Physical review letters*, 90(21):216601, 2003.

[37] JM Fraser, AI Shkrebtii, JE Sipe, and HM Van Driel. Quantum interference in electron-hole generation in noncentrosymmetric semiconductors. *Physical review letters*, 83(20):4192, 1999.

[38] E Papastathopoulos, D Xenakis, and D Charalambidis. Phase-sensitive ionization through multiphoton-excitation schemes involving even numbers of photons. *Physical Review A*, 59(6):4840, 1999.

[39] Rodrigo A Muniz, Kai Wang, JE Sipe, and ST Cundiff. Quantum interference control of two-and three-photon processes. In *2016 Conference on Lasers and Electro-Optics (CLEO)*, pages 1–2. IEEE, 2016.

[40] Kai Wang, Rodrigo A Muniz, JE Sipe, and ST Cundiff. Quantum interference control of injected photocurrent in an algaas waveguide. In *CLEO: Applications and Technology*, pages JW2A–158. Optica Publishing Group, 2018.

[41] Rodrigo A Muniz, Cuauhtémoc Salazar, Kai Wang, ST Cundiff, and JE Sipe. Quantum interference control of carriers and currents in zinc blende semiconductors based on nonlinear absorption processes. *Physical Review B*, 100(7):075202, 2019.

[42] Kai Wang, Rodrigo A Muniz, JE Sipe, and ST Cundiff. Comb offset frequency measurement using two-photon—three-photon quantum interference control. In *CLEO: Applications and Technology*, pages JTh2A–68. Optica Publishing Group, 2017.

[43] Mark Lundstrom. Fundamentals of carrier transport, 2nd edn. *Measurement Science and Technology*, 13(2):230–230, 2002.

[44] David H Auston, KB Eisenthal, RM Hochstrasser, CK Johnson, W Kaiser, A Laubereau, D von der Linde, A Seilmeier, CV Shank, and W Zinth. Ultrashort laser pulses and applications. 2013.

[45] SS Prabhu, SE Ralph, MR Melloch, and ES Harmon. Carrier dynamics of low-temperature-grown gaas observed via thz spectroscopy. *Applied Physics Letters*, 70(18):2419–2421, 1997.

[46] Alfred Leitenstorfer, Cornelius Fürst, Alfred Laubereau, Wolfgang Kaiser, Günther Tränkle, and Günter Weimann. Femtosecond carrier dynamics in gaas far from equilibrium. *Physical review letters*, 76(9):1545, 1996.

[47] W Fawcett, AD Boardman, and S Swain. Monte carlo determination of electron transport properties in gallium arsenide. *Journal of Physics and Chemistry of solids*, 31(9):1963–1990, 1970.

[48] Michael Shur. Physics of semiconductor devices, prentice hall. *Inc., Englewood Cliffs, New Jersey*, page 680, 1990.

[49] Kai Wang, Rodrigo A. Muniz, J. E. Sipe, and S. T. Cundiff. Quantum interference control of photocurrents in semiconductors by nonlinear optical absorption processes. *Phys. Rev. Lett.*, 123:067402, Aug 2019.

[50] Yue Zheng, Jing Gao, Cheng Han, and Wei Chen. Ohmic contact engineering for two-dimensional materials. *Cell Reports Physical Science*, 2(1), 2021.

[51] VL Rideout and CR Crowell. Solid-state electron. *Solid-State Electron*, 18:541, 1975.

[52] TC Shen, GB Gao, and H Morkoc. Recent developments in ohmic contacts for iii–v compound semiconductors. *Journal of Vacuum Science & Technology B: Microelectronics and Nanometer Structures Processing, Measurement, and Phenomena*, 10(5):2113–2132, 1992.

[53] Carl Wilmsen. *Physics and chemistry of III-V compound semiconductor interfaces*. Springer Science & Business Media, 2013.

[54] EH Rhoderick and RH Williams. Metal-semiconductor contacts (clarendon, oxford). 1978.

[55] AG Baca, F Ren, JC Zolper, RD Briggs, and SJ Pearton. A survey of ohmic contacts to iii-v compound semiconductors. *Thin solid films*, 308:599–606, 1997.

[56] Ralph E Williams. Gallium arsenide processing techniques. *(No Title)*, 1984.

[57] Masanori Murakami, KD Childs, John M Baker, and A Callegari. Microstructure studies of aunige ohmic contacts to n-type gaas. *Journal of Vacuum Science & Technology B: Microelectronics Processing and Phenomena*, 4(4):903–911, 1986.

[58] Piotr Karbownik, Anna Baranska, Anna Szerling, Wojciech Macherzynski, Ewa Papis, Kamil Kosiel, Maciej Bugajski, Marek Tlaczala, and Rafal Jakiela. Low resistance ohmic contacts to n-gaas for application in gaas/algaas quantum cascade lasers. *Optica Applicata*, 39(4):655, 2009.

[59] MW Cole, WY Han, LM Casas, DW Eckart, T Monahan, and KA Jones. The mechanisms of formation of ohmic contacts to algaas: A microstructural, elemental diffusion and electrical investigation. *Scanning: The Journal of Scanning Microscopies*, 18(5):379–384, 1996.

[60] https://materion.com/-/media/files/advanced-materials-group/me/challenge-of-applying-ohmic-contacts.pdf.